FREEZING AND OPTICAL PROPERTIES OF MODEL ATMOSPHERIC AEROSOLS

by

Michael Elliot Earle

A thesis
presented to the University of Waterloo
in fulfilment of the
thesis requirement for the degree of
Doctor of Philosophy
in
Chemistry

Waterloo, Ontario, Canada, 2007

I hereby declare that I am the sole author of this thesis. This is a true copy of the thesis, including any required final revisions, as accepted by my examiners.

I understand that my thesis may be made electronically available to the public.

ABSTRACT

The freezing of model atmospheric aerosols – specifically, model cirrus cloud particles – was investigated through laboratory studies of supercooled water aerosols. Water droplets with radii of 1 – 2.7 μm were exposed to well-defined temperature profiles ranging from 240 – 230 K in a cryogenic flow tube apparatus, and observed using infrared extinction spectroscopy. A computational characterization procedure, based on theories of light scattering, was used to determine the size and phase composition of aerosols from extinction spectra. The procedure showed large ice fractions at uncharacteristically warm temperatures, which was attributed to the formation of ordered, "ice-like" clusters of molecules in supercooled water. Temperature-dependent complex indices of refraction were determined from the supercooled water extinction spectra, and showed changes reflecting this ordered formation. Taking the "ice-like" character of clusters into account, the homogeneous nucleation point for micrometre-sized water aerosols was determined to be 236.2 K. A microphysical model was developed to determine temperature-dependent, volume- and surface-based homogeneous nucleation rates from experimental freezing data. The model results indicated that surface nucleation was the dominant process for our range of experimental conditions. This was supported by separate studies of smaller, 0.63 and 0.75 μm radius aerosols, with larger surface-to-volume ratios.

An optical microscopy apparatus was placed in the cryogenic flow tube to allow real-time imaging of particles in freezing experiments. The imaging studies demonstrated the utility of the microscopy apparatus for the observation and classification of ice crystal

habits. Ray tracing and image processing algorithms were used to analyze particle geometry and size. The latter was used to validate the size retrievals from the aerosol characterization procedure.

Additional studies probed the changes in the optical properties of crystalline ammonium sulfate, $(NH_4)_2SO_4$, due to the paraelectric-to-ferroelectric transition at 223 K. Temperature-dependent refractive indices were determined from crystalline $(NH_4)_2SO_4$ extinction spectra. Only small changes in these values were observed down to 223 K, below which significant changes were observed, due to the changes in lattice structure accompanying the ferroelectric transition.

ACKNOWLEDGEMENTS

This thesis marks the culmination of an extremely positive and memorable four years at the University of Waterloo, and bears the fingerprints of all of those who have helped along the way. For these contributions, I offer my sincerest thanks. I would first like to thank Dr. Sloan for providing me with the opportunity to work on this project, and for his continued support, insight, and advice. His patience and encouragement provided the backdrop for my progress and development, and for this I am forever appreciative. I would also like to thank the members of my Ph.D. committee – Dr. Bernath, Dr. Edwards, and Dr. Thomas – for all of their questions and comments, and for making committee meetings and seminars relaxed and surprisingly bearable. In addition, I would like to acknowledge both NSERC and the University of Waterloo for their respective roles in the funding of this project.

I would like to extend special thanks to Alexei Khalizov, who was my mentor and co-worker for my first two years in the Sloan lab. Alexei taught me about experimental chemistry, aerosol science, and equally as important, the intrinsic qualities that make a good scientist. What will forever stand out, though, are our various discussions while running experiments, covering such topics as nucleation theory, Russian history, Paris Hilton, and the weird smell ladybugs make when sucked into a vacuum cleaner.

I am also grateful for the friendship and support of the members of the Sloan lab group, past and present. In particular, I would like to thank Thomas Kuhn, for all of his help in the laboratory, and for numerous invaluable discussions. Special mention must also be given to Alex Zasetsky, Rodion Remorov, Robert Schiwon, Igor Grishin, our lab

technicians Chris DaMaren, Mike Hintermeister, and Alex Chornyy, and the staff of the Science and Electronics Shops

My friends and family also deserve a huge amount of credit, for keeping me positive in the face of adversity and ridiculous amounts of work (I'm looking at you, comprehensive exam), and for making my time outside of the lab both fulfilling and entertaining. I would especially like to thank Wayde Johnson, Monica Harvey, and my roommate of the past two years, the now-Doctor Mike Dick, a fellow Maritimer in a smoggy, foreign land. And of course, this section would not be complete without special recognition of the key members of my motivational and emotional support system, and co-chairs of the Mike Earle fan club, my mother, Nancy Earle, and fiancée, Nikki Parliament.

DEDICATION

To my family and Nikki, for all of their encouragement, support, and putting up with mature complaints such as “I’m bored of studying,” and “I wish this thesis would just write itself.”*

---

* Author’s note: Theses don’t, in fact, write themselves, despite wishes to the contrary.

TABLE OF CONTENTS

LIST OF FIGURES

Chapter 5

Chapter 6

Chapter 7

Chapter 8

Chapter 9

Appendix A

CHAPTER ONE

INTRODUCTION

1.1. Introduction

Aerosols have been the subject of extensive scientific investigation in recent years, owing largely to the role these suspended, condensed-phase particles[1] play in the redistribution of energy in Earth's atmosphere. This alteration of Earth's radiative balance, termed radiative forcing, can have a significant impact on climate.[2] Radiative forcing can be positive or negative, denoting increases or decreases, respectively, in the radiant power reaching Earth's surface per unit area (typically expressed in units of W/m^2). Increases in the mean global surface temperature of ~ 0.3 to 0.6 °C over the past century have been largely attributed to positive forcing by greenhouse gases (CO_2, CH_4, etc.), generally estimated to be ~ +2.4 W/m^2.[3,4] In order to assess long-term and future heating and climate trends, it is important to understand the potentially mitigating radiative effects of atmospheric aerosols.

The magnitude and direction of radiative forcing by aerosols depend strongly upon composition and size. The chemical components comprising the most significant fractions of the total aerosol mass are sulfate, ammonium, nitrate, sea salt, mineral dust, black (elemental) carbon, and various organics.[4] These components can be formed directly from natural or anthropogenic sources (primary aerosols), or by gas-to-particle conversion in the atmosphere (secondary aerosols).[4,5] Particle diameters are typically between 0.01 and 100 μm, with fine particles less than 2.5 μm in diameter predominating the total number and mass of aerosols.[3,5] The influence of these small, chemically diverse particles on Earth's radiative balance is divided into direct and indirect effects based on the way in which the particles interact with light.

In the direct effect, atmospheric aerosols scatter and absorb incident solar (short-wave) radiation, which has maximum intensity in the wavelength range between ~ 0.3 to 0.7 μm, and absorb surface-emitted thermal (infrared) radiation, with maximum intensity between ~ 4 to 20 μm.[2-4,6] Light scattering by aerosols depends on particle diameter, d, and the wavelength of light, λ, and is typically considered in terms of the scattering parameter, α:[5]

$$\alpha = \frac{\pi d}{\lambda} \tag{1.1}$$

Scattering is strongest when d and λ are of similar magnitude. Indeed, since the majority of aerosols are of similar diameter to the wavelengths of greatest intensity in the solar spectrum, this radiation is strongly scattered in the atmosphere, reducing the flux to Earth's surface (negative forcing).[2] The absorption of solar radiation by atmospheric aerosols also results in negative forcing,[6] while the absorption of terrestrial thermal radiation by aerosols results in positive radiative forcing. The magnitude of this positive forcing is comparatively small, and thus, the overall forcing due to aerosol direct effects is negative.[3,7]

This net negative forcing is compounded by indirect aerosol effects, in which aerosols perturb Earth's radiative balance through their role in cloud formation.[2-4,6] Atmospheric aerosols act as nuclei for the formation of aqueous droplets and ice particles; these aerosols are referred to as cloud condensation nuclei (CCN) and ice nuclei (IN), respectively. The concentrations of CCN and/or IN influence the number and size of cloud particles, which in turn, determine their scattering properties, the frequency of precipitation, and cloud lifetime.[6,8] The overall forcing due to aerosols, combining both direct and indirect effects, is generally estimated to be negative, with values between ~ -1 to -2 W/m^2.[4,7]

The radiative effects of the pure liquid water and ice aerosols in clouds must also be considered. Cirrus clouds, in particular, cover approximately one-third of the Earth's surface, and hence, their contribution to the overall radiative balance is significant.[9,10] Cirrus clouds are thin, wispy clouds found in the upper troposphere and lower stratosphere between approximately 4 and 20 km.[10,11] With characteristic temperatures of ~ 248 to 213 K, these clouds are composed primarily of ice particles ranging in diameter from 0.1 μm to 8 mm.[12] Cirrus cloud particles scatter incident solar radiation and absorb surface-emitted infrared radiation, as per the direct aerosol effect described above; however, the larger particles in cirrus clouds have a greater tendency to scatter solar radiation in the forward direction (same direction as incident light), increasing the flux toward Earth's surface.[10,13] The radiative influence of cirrus clouds is further complicated by particle shape. The thermodynamically stable phase of ice at atmospheric pressure and temperatures down to ~ 190 K is hexagonal in shape and structure (ice-I$_h$), but a variety of crystalline shapes, or "habits," can form, as evidenced by the myriad different types of snowflakes.[12] The scattering properties of aerosols vary with shape; for example, as particles become less symmetrical, the extent of forward scattering increases.[10] Given this propensity for forward scattering, and to a larger extent, the strong absorption of infrared radiation by water and ice, the net radiative influence of cirrus cloud aerosols is generally estimated to be positive.[10,13]

Estimates of aerosol forcing come from computational radiative transfer models (henceforth referred to as climate models), which are constrained, or parameterized, by the results of field observations, satellite measurements, and laboratory studies.[7] An ever-expanding knowledge base of particle sizes, shapes, compositions (including phase), and concentrations in the atmosphere has been obtained, yet estimates of aerosol forcing are still highly uncertain, as the fundamental microphysical behaviour that determines these properties is poorly understood. This behaviour extends beyond the role of aerosols as CCN and IN noted above; aerosols can also undergo a variety of phase transitions in the atmosphere. These changes in phase are particularly important, as phase influences the physical, chemical, and optical properties of aerosols,[14-16] which in turn, influence Earth's radiative balance and climate.

1.2. Phase Transitions of Aerosols

Phase transitions of aerosols can occur with changes in temperature and relative humidity (RH), the latter of which is typically expressed in percent, as follows:[11]

$$RH = \frac{p_{H_2O}}{p^0_{H_2O}} \times 100\% \tag{1.2}$$

where p_{H_2O} is the partial pressure of water vapour and $p^0_{H_2O}$ is the saturation vapour pressure of water at a given ambient temperature. As temperature is decreased, aqueous aerosols can undergo liquid-to-solid transitions, or freezing, resulting in the formation of ice and various crystalline hydrates (*e.g.* nitric acid trihydrate, NAT).[14] The opposing solid-to-liquid transition (melting) can occur as temperature is increased. Solid-to-solid phase transitions can also occur with changes in temperature. For example, crystalline ammonium sulfate, $(NH_4)_2SO_4$, can undergo a transition from the paraelectric phase to the ferroelectric phase upon cooling below 223 K.[14,17-19] This transition involves changes in lattice structure, which give rise to spontaneous polarization of the crystal. Additional temperature-dependent phase transitions include precipitation, in which salts crystallize from aqueous solutions as the temperature is reduced, and dissolution, in which crystalline salt species dissolve into solution upon warming.[14]

Precipitation and dissolution should be distinguished from efflorescence and deliquescence, respectively, in which aqueous solutions undergo similar transitions, but with changes in RH rather than temperature.[11,14] In efflorescence, water from an aqueous solution aerosol exposed to decreasing RH will evaporate, causing the aerosol to become smaller and increasingly saturated before crystallizing, or efflorescing, at a threshold humidity characteristic of the aqueous species (efflorescence RH). In deliquescence, on the other hand, a crystalline salt particle exposed to successively higher RH will not grow steadily larger and more dilute, but rather, will spontaneously uptake water to form a saturated aqueous solution only once the RH has increased to a second characteristic threshold value (deliquescence RH). The sequential versus spontaneous nature of these transitions results in the deliquescence RH generally being much higher than the efflorescence RH. These transitions are said to exhibit hysteresis; that is, they depend on the phase and humidity history of particles, and do not follow changes in conditions as might otherwise be expected.

Considering the effects of phase transitions on the physical properties of aerosols, deliquescence will result in increased particle sizes compared to the initial crystalline species, while reductions in RH above the efflorescence point will lead to corresponding decreases in size for aqueous solution aerosols. Recalling Equation 1.1, these changes in size will affect the aerosol scattering properties. As discussed in the previous section, scattering is also influenced by particle shape. Aqueous aerosols are spherical, as their surface tension minimizes their surface-to-volume ratios. Transitions between the aqueous and crystalline phases (*e.g.* hexagonal ice crystals) can therefore result in changes in particle shape, and hence, the aerosol scattering properties.

In addition, phase transitions can influence both the scattering and absorption of radiation by aerosols by changing their optical properties. The properties of interest in this case are the complex indices of refraction, n^*, also referred to as optical constants. Expressed in terms of ν, the frequency of light (typically expressed in s^{-1}):

$$n^*(\nu) = n(\nu) + ik(\nu) \tag{1.3}$$

The real component, $n(\nu)$, is related to scattering, while the imaginary component, $k(\nu)$, is related to absorption. Optical constants are phase-dependent, reflecting the structural changes which accompany changes in phase. For example, liquid water and ice have distinctly different refractive indices, as do crystalline and aqueous $(NH_4)_2SO_4$ (among other inorganic salts). It should be noted that Equation 1.3 can also be expressed in terms of wavelength, λ (units of μm or nm), or wavenumber, $\tilde{\nu}$ (units of cm^{-1}), which are related to ν as follows:

$$\nu = \frac{c}{\lambda} = c\tilde{\nu} \tag{1.4}$$

where c is the speed of light. Frequency, wavelength, and wavenumber will be used interchangeably throughout this thesis, depending upon the specific context.

1.3. Thesis Overview

Given the impact of phase on aerosol properties, and by extension, Earth's radiative balance and climate, it is evident that further understanding of aerosol phase transitions under atmospherically-relevant conditions is required to better parameterize climate models. Accordingly, this work focuses largely on the freezing transition for model atmospheric aerosols. This transition is approached from the most fundamental perspective: the homogeneous nucleation of ice in pure, supercooled water aerosols. Outstanding questions remain regarding the dependence of homogeneous nucleation on particle volume and/or surface area, as well as the temperature dependence of the associated nucleation rates. In addition, the frequency of occurrence of different ice crystal habits as a function of the formation conditions has not been well-characterized. These questions and shortcomings are addressed in the present work through laboratory studies of supercooled water aerosols. These studies are performed in a cryogenic, laminar aerosol flow tube apparatus capable of reproducing temperature conditions characteristic of the upper troposphere and lower stratosphere. Hence, the results from these studies are directly applicable to the formation and properties of cirrus clouds.

The changes in aerosol optical properties that accompany phase transitions are also a focal point of this thesis. The changes accompanying the freezing transition for pure water aerosols are considered in conjunction with the above studies. Separate studies investigate the changes in optical properties due to the ferroelectric transition of crystalline $(NH_4)_2SO_4$. Temperature- and phase-dependent complex indices of refraction for common atmospheric aerosol species are important for improving the accuracy of data retrievals in remote sensing and laboratory studies, which often employ values obtained at ambient temperature.

The theoretical basis and background for this work is given in Chapter 2, including homogeneous nucleation theory, the processes by which ice particles can grow following nucleation, and the resulting crystal habits. Chapter 3 describes the general experimental setup and methodology used in this work, with Chapter 4 expanding the description to include the development and optimization of the laminar aerosol flow tube apparatus. Chapter 5 details the investigation of the freezing of supercooled water aerosols, and how this investigation led to the determination of temperature-dependent optical constants for supercooled water, which is the subject of Chapter 6. The microphysical model used to determine homogeneous nucleation rates from experimental freezing data is described in Chapter 7, along with the resulting temperature-dependent rates for volume and surface nucleation. Chapter 8 outlines a new flow tube apparatus constructed to expand the range of experimental conditions. The resulting freezing data and nucleation rates are presented, and compared with the results from the preceding chapters. An experimental approach for ice crystal habit observations, and preliminary results, are given in Chapter 9. Conclusions and directions for future study are provided in Chapter 10. Appendix A details the investigation of the temperature-dependent complex indices of refraction for crystalline $(NH_4)_2SO_4$ aerosols, and Appendix B provides the code for the microphysics model noted above.

CHAPTER TWO

BACKGROUND AND THEORY

2.1. Introduction

The kinetics of homogeneous nucleation largely determine the extent of ice formation in the upper troposphere and stratosphere. The inherent dependence of classical nucleation theory upon droplet volume has been called into question by recent studies which have proposed a thermodynamic basis for a process dependent upon droplet surface area. Irrespective of the underlying nucleation process, the nascent ice particles are subject to growth by secondary processes in the atmosphere, which can alter their sizes and habits, and in turn, their radiative properties. The central concepts of supercooling, nucleation theory, secondary growth, and crystal habit are discussed in the following chapter, along with their relevance to the formation and properties of cirrus clouds.

2.2. Homogeneous Nucleation of Ice in Supercooled Water

Aerosol droplets can exist in a metastable liquid or aqueous phase at temperatures below their thermodynamic freezing points, a phenomenon referred to as "supercooling".[20] Water droplets, for instance, can be supercooled below 273 K, despite the fact that crystalline ice is the thermodynamically stable phase at these temperatures. In fact, liquid water droplets have been observed in clouds at temperatures as low as 233 K.[21] Supercooling occurs when there are no nucleation centres present within the bulk liquid.[20] Nucleation centres serve as starting points for crystal lattice growth, and as such, initiate the liquid-to-solid phase transition.[20,22] The kinetics of nucleus formation are therefore of primary concern when considering the freezing process, since it is the presence or absence of these nuclei that determines whether the liquid will undergo a phase transition, or remain in a supercooled state.

In certain cases, material other than the bulk liquid can initiate the liquid-to-solid phase transition.[1] This is referred to as heterogeneous nucleation. In these cases, the foreign material provides nucleation centres, and so the formation of nuclei need not be considered. In the absence of solutes and/or impurities (pure liquids), however, nucleation centres can be formed from molecules of the bulk liquid.[1] This is known as homogeneous nucleation. These nuclei are formed as the result of continuous, random structural fluctuations in the liquid.[23,24] These fluctuations lead to chance agglomerations of the liquid molecules, forming organized clusters called embryos.[12] Nuclei will form when embryos reach a critical (germ) size, as determined by the free energy of the system.[12,24] This can be conceptualized using classical nucleation theory, in which the net change in free energy upon nucleation, W, is given by the following:[24]

$$W = \frac{4\pi r^3 \Delta G}{3V_m} + 4\pi r^2 \sigma \tag{2.1}$$

The first term in Equation 2.1 represents the change in free energy, ΔG, per mole of the bulk liquid upon forming a spherical crystalline region of radius r within a molar volume V_m. The second term in Equation 2.1 represents the surface energy of the crystal-liquid interface, where σ is the surface tension. The contribution of the bulk term to W is negative, while that of the surface term is positive.[25]

Figure 2.1 shows the change of *W* as a function of *r*. Below the critical radius, *r**, *W* increases with *r*. In such cases, re-melting of the embryo will lead to a decrease in free energy, and is thus the favoured process, superseding nucleation. However, in the event that a chance agglomeration of liquid molecules reaches the critical size, corresponding to the point of maximum free energy, *W**, a stable crystalline nucleus results. As discussed further in the following section, subsequent crystal growth beyond *r** will lead to corresponding decreases in free energy.

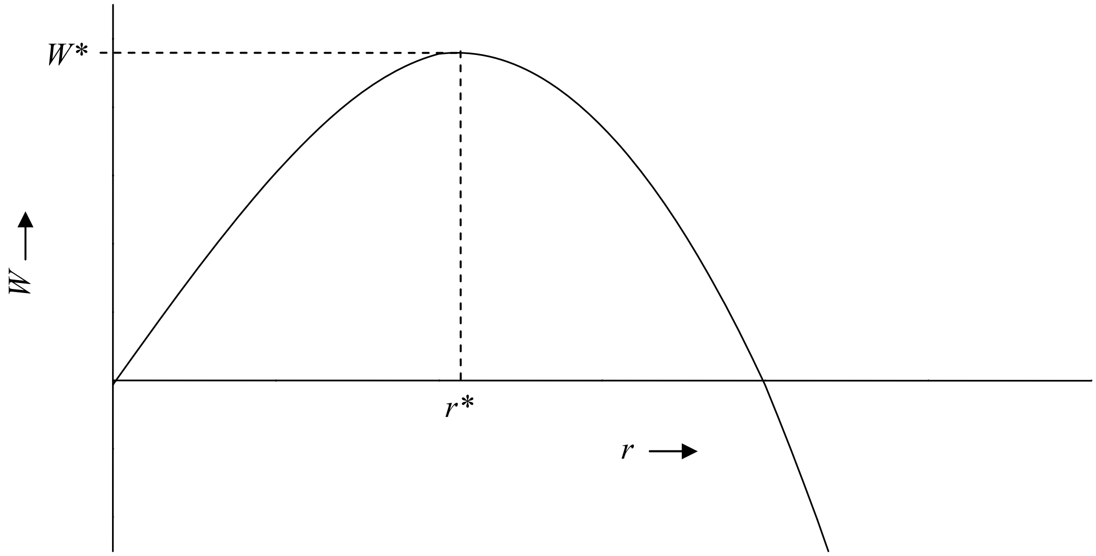

Figure 2.1: Change in net free energy of nucleation as a function of embryo radius.

The occurrence of a homogeneous nucleation event can be considered further using statistical thermodynamics.[24] The probability that structural fluctuations in the bulk liquid will overcome the free energy barrier *W** is given by the Boltzmann term:

$$p(W^*) = \exp\left(\frac{-W^*}{RT}\right) \tag{2.2}$$

where R is the ideal gas constant and T is temperature. Structural rearrangements are also an integral part of the nucleation process, as liquid molecules must reorient themselves when forming the crystal structure.[22,24] The rate at which these rearrangements occur is proportional to an Arrhenius rate factor:

$$\exp\left(\frac{-\Delta G_D}{RT}\right) \tag{2.3}$$

in which ΔG_D is the activation energy corresponding to the rearrangement.[24] It follows that the overall rate of homogeneous nucleation, J, depends upon both a thermodynamic factor associated with overcoming the free energy barrier to critical nucleus growth, and a kinetic factor related to the structural reorganization implied therein. Combining these factors gives the rate of homogeneous nucleation as follows:[24]

$$J = A\exp\left(\frac{-W^*}{RT}\right)\exp\left(\frac{-\Delta G_D}{RT}\right) \tag{2.4}$$

where A is a proportionality constant, and J is typically expressed in units of cm^{-3} s^{-1}. Note that both factors in Equation 2.4 are exponentially dependent upon temperature.

2.3. Crystal Growth and Implications for Freezing

The nucleus serves as a template for crystal growth, in which the crystalline structure is extended throughout the entire droplet; thus, crystal growth completes the freezing transition. For a crystal to grow, liquid molecules must detach themselves from the liquid structure and attach to the nucleation centre.[24] In doing so, the molecules must pass from their average equilibrium positions in the liquid to new equilibrium positions in the crystal form, the two positions being separated by an energy barrier, $\Delta G'$.[12] In other terms, $\Delta G'$ is the free energy of activation for the diffusion of liquid molecules across the liquid-crystal interface. Thus, crystal growth is a diffusion-limited process. Similar to the preceding treatment of nucleation rates, the rate of crystal growth, u, is proportional to both Arrhenius and Boltzmann terms:[24]

$$u = a_0 \nu \exp\left(\frac{-\Delta G'}{RT}\right)\left(1 - \exp\left(\frac{\Delta G}{RT}\right)\right) \tag{2.5}$$

In Equation 2.5, a_0 is the intermolecular distance in the crystal, and ν is the frequency of thermal vibrations in the material. Recall that ΔG represents the decrease in free energy per mole upon nucleation within the bulk droplet volume. Values of u are generally expressed in cm s^{-1}.

From Equation 2.5 it is apparent that crystal growth, like homogeneous nucleation, is a temperature-dependent process; however, the dependence differs in each case. It therefore follows that freezing will only occur at temperatures where both processes are thermodynamically favoured. Nucleation and crystal growth can be readily visualized in terms of two temperature-dependent rate curves, whose overlap determines whether freezing will occur.[24] Figure 2.2 illustrates favourable overlap, resulting in a liquid-to-solid phase transition at temperatures in the overlap region, centred at temperature T_f.

2.4. Surface vs. Volume Nucleation

The treatment of freezing presented thus far has followed the conventional approach of classical nucleation theory. This approach assumes that nucleation only occurs within the bulk volume of a supercooled liquid droplet.[26] A collection of experimental work has investigated the freezing of liquid water droplets suspended in air,[27-30] oil,[31] and in emulsions,[32] reporting homogeneous nucleation rates as a function of

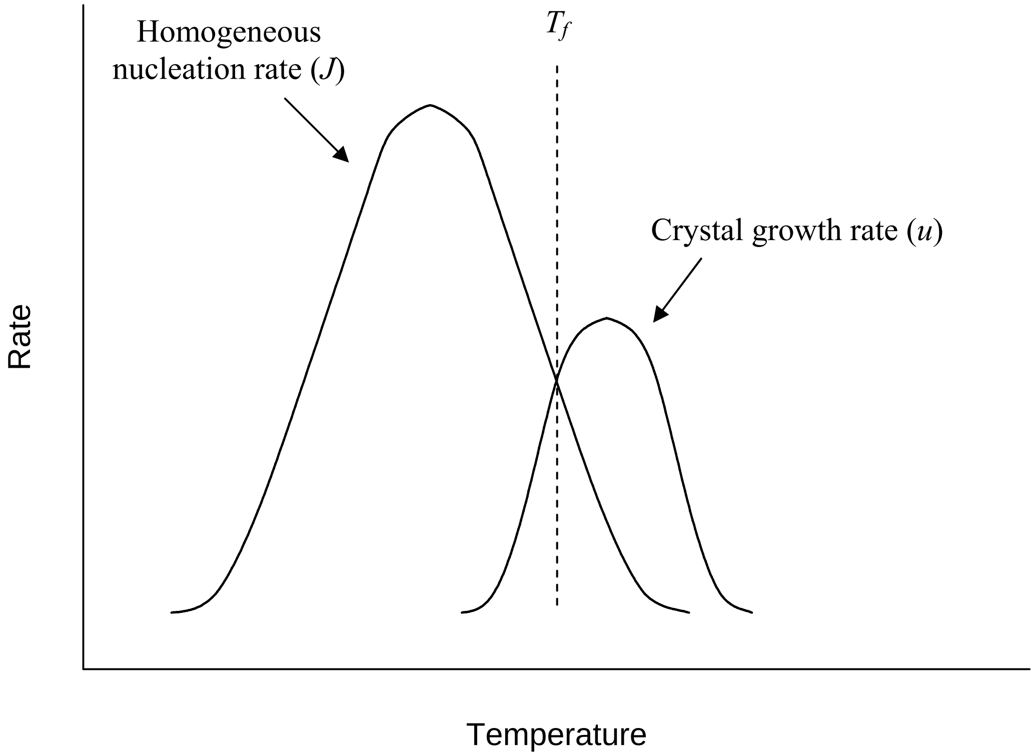

Figure 2.2: Favourable overlap of rate curves for homogeneous nucleation and crystal growth. Freezing will occur over the range of temperatures at which the curves overlap, centred at T_f.

droplet volume (see Section 7.1 for further discussion of these studies and the general approach to nucleation rate determination). Despite good general agreement with theoretical values (from Ref 33), there was some discrepancy between the results obtained by different methods, notably a spread in values of over five orders of magnitude at 240 K.[34] This discrepancy suggested that the classical, volume-based approach was insufficient to describe the freezing of pure water droplets.

Recent work has addressed this deficiency, proposing that in some cases, crystal nucleation at the droplet surface is thermodynamically favoured over nucleation inside the droplet volume.[26,34,35] This is referred to as pseudoheterogeneous nucleation, or more simply, surface nucleation. Prompted by the results of computer simulations which showed preferential nucleus formation at or near the surface,[36-38] Djikaev *et al.* conducted a thermodynamic assessment of the work of crystalline nucleus formation in both the volume- and surface-based cases.[26] The principal difference between the two cases was found to be the energetic contribution of interfaces formed with the crystalline nucleus. The interfaces formed in each case are illustrated in Figure 2.3.

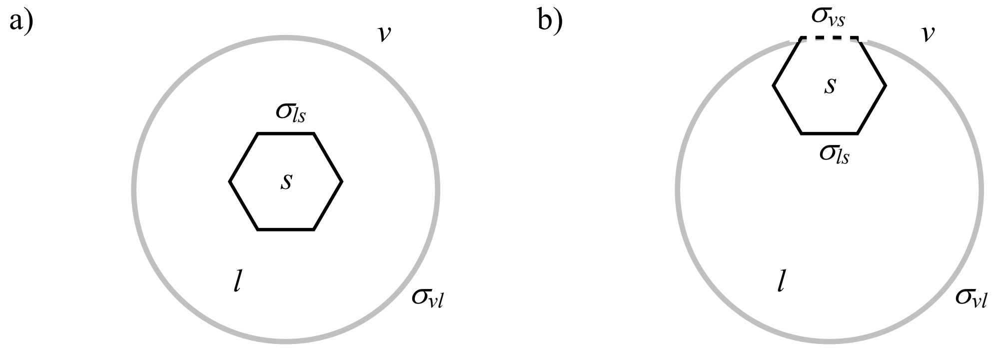

Figure 2.3: Schematic representations of (a) volume-based nucleation and (b) surface-based nucleation, showing interfaces formed between the vapour (*v*), liquid (*l*), and solid (*s*) phases. The interfaces are vapour-liquid (grey line), liquid-solid (black line), and vapour-solid (dashed black line), with surface tensions σ_{vl}, σ_{ls}, and σ_{vs}, respectively.

Classical, volume-based nucleation results in the formation of a liquid-solid interface with surface tension σ_{ls}. The overall energy of the interface is given as $\sigma_{ls}A_c$, the product of the surface tension (expressed in units of energy per cm^2) and the surface area of the crystalline nucleus, A_c. Surface nucleation, on the other hand, results in the formation of a vapour-solid interface, where one face of the crystal nucleus is in contact with the surrounding vapour. Denoting the area of this crystal face as A_f, the interfacial energy is given by $\sigma_{vs}A_f$. The remaining faces of the crystal are all in contact with the liquid phase, and thus, the overall surface energy is:

$$\sigma_{ls}(A_c - A_f) + \sigma_{vs}A_f \tag{2.6}$$

The question of the thermodynamic favourability of the surface-based process can be considered in terms of the one crystal face in contact with the vapour, which distinguishes this process from classical nucleation. Were this face formed within the bulk volume, the vapour-solid interface would be replaced by liquid-solid and vapour-liquid interfaces, both of area A_f. The energy $\sigma_{vs}A_f$ would therefore be replaced by the sum of contributions from these interfaces:

$$\sigma_{ls}A_f + \sigma_{vl}A_f \tag{2.7}$$

Thus, surface nucleation will be thermodynamically favoured for the condition:

$$\sigma_{ls}A_f + \sigma_{vl}A_f > \sigma_{vs}A_f \tag{2.8}$$

which, since A_f is constant, reduces to:

$$\sigma_{ls} + \sigma_{vl} > \sigma_{vs} \tag{2.9}$$

In other words, if the sum of the surface tensions of the liquid-solid and vapour-liquid interfaces exceeds that of the vapour-solid interface, homogeneous nucleation will occur at the droplet surface.

The inequality postulated in Equation 2.9 corresponds with the condition for the partial wettability of a solid by its own melt.[25,26,34,35] Figure 2.4 shows a drop of liquid, or melt, partially wetting the surface of a solid at a contact angle, θ (for complete wetting of the surface, $\theta = 0$). Further wetting of the surface will increase the areas of the liquid-solid and vapour-liquid interfaces, and decrease the area of the vapour-solid interface. Partial wetting thus requires that any increases in the extent of wetting are discouraged by

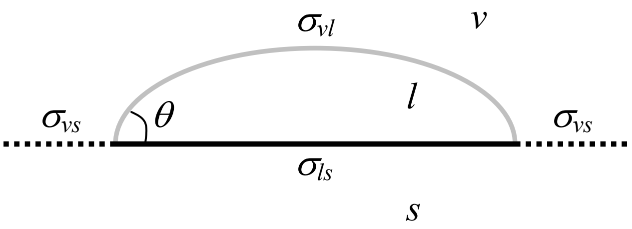

Figure 2.4: Partial wetting of a solid by a liquid drop with contact angle θ. Phase, interface, and surface tension designations follow from Figure 2.3.

overall increases in surface energy, as per the condition in Equation 2.9.[35] Partial wetting of ice surfaces by liquid water has been observed experimentally,[39] supporting the thermodynamic basis for surface-based nucleation detailed above.

Tabazadeh *et al.*[34] attempted to reconcile the discrepancies in volume-based nucleation rates noted above by treating the reported values from a surface-based perspective. The volume nucleation rates in cm^{-3} s^{-1} were denoted as J_V, and converted to surface nucleation rates, J_S, in cm^{-2} s^{-1} using the following relation:

$$J_S = \frac{J_V r}{3} \tag{2.10}$$

where r is the particle radius reported in each study (assuming monodisperse particle size distributions). The overall spread in values was not significantly improved by this approach. It was found, however, that in some cases, the correspondence between values obtained in different studies was improved, while in other cases, it was not. This led the authors to suggest that the total nucleation rate, J_T, is the sum of contributions from both volume and surface nucleation, and that the relative contributions of each process depend on the nature of the interface with the droplet (air or oil) and droplet size.[29,34]

$$J_T = J_V V + J_S S \tag{2.11}$$

In Equation 2.11, V and S are the volume and surface area of droplets, respectively. The contribution of surface nucleation will increase with decreasing particle size, which increases the surface-to-volume ratio. This is in accordance with the results of Duft and Leisner,[28] who found that nucleation rates for droplets with radii of 19 μm and 49 μm scaled with droplet volume, and suggested that surface nucleation will only be important for particles less than ~ 1 μm in radius.[25]

Further support for surface nucleation comes from recent studies of heterogeneous freezing in supercooled water droplets. Shaw *et al.*[40] and Durant and Shaw[41] showed that the presence of heterogeneous nuclei at the surface of 3 – 4 mm diameter water droplets resulted in freezing temperatures 4 – 5 K warmer than when the nuclei were present within the bulk volume. This was believed to be a manifestation of surface nucleation, as the nature of the studies eliminated the potential for transient effects caused by a nucleus contacting the droplet surface,[42] which had been considered to give rise to similar phenomena in previous studies.[12] In addition, video imaging studies by Hindmarsh *et al.*[43] demonstrated the role of surface nucleation in suspended sucrose solution droplets, particularly at lower sucrose concentrations. Recent molecular dynamics simulations of supercooled water[44,45] and gold nanoparticles[46] have also provided evidence in favour of nucleation at or near the liquid-vapour interface.

The question of whether the freezing of a supercooled water droplet is initiated in the bulk volume and propagated to the surface, or initiated at or near the surface and propagated into the bulk, is of more than just fundamental interest. The preponderance of surface nucleation for small cloud and aerosol particles could have significant ramifications, as the surfaces of these particles are more prone to modification by anthropogenic emissions (*e.g.* adsorption of organic surfactant species that lower the surface tension of the air-water interface[47-49]) than the bulk material.[28,34] Furthermore, the dependence of homogeneous nucleation rates on particle volume or surface area (and the temperature-dependence of these rates) is important for climate models to more accurately predict the freezing of cloud particles given initial size and temperature information. The fraction of particles of each phase, their respective sizes, and the ambient conditions will dictate ice crystal growth by secondary processes, as discussed in the following section.

2.5. Secondary Growth Processes

For mixed-phase clouds (liquid water and ice), the saturation vapour pressure over ice particles is lower than that over liquid droplets at a given temperature. The resulting gradients between the vapour pressures above particles and the partial pressure of water in the surrounding gas drive the exchange of vapour-phase mass from liquid to ice, causing the ice particles to grow at the expense of the liquid droplets. This process is termed the Bergeron-Findeisen mechanism,[50,51] but is generally referred to as deposition growth[12] or mass transfer.[17] The microphysics of mass transfer and the corresponding evaporation/growth of aerosols are detailed in Section 7.2.1. Mass transfer is most important near the homogeneous nucleation point, where only small fractions of the total aerosol have frozen, and the saturation vapour pressure of water is significant. As the temperature is reduced below the nucleation point, mass transfer is suppressed, as the fraction of ice particles is larger, and the saturation vapour pressure over water droplets is less significant.

Ice particles can also grow through collisions with other ice particles, or with supercooled liquid droplets.[12] In the former case, the process is known as clumping or aggregation, while in the latter case, the process is known as riming. Herein we will refer to riming as contact freezing, which is more reflective of the underlying process, in which a supercooled liquid droplet freezes immediately upon contact with an ice particle. Both collisional and mass transfer growth can occur within clouds. The combination of ice nucleation, which produces crystals of distinct structure and geometry, with the secondary growth processes detailed above, gives rise to an interesting variety of ice crystal shapes, or habits.

2.6. Ice Crystal Structure and Habit

As noted in Section 1.1, the thermodynamically stable phase of ice in the atmosphere is hexagonal ice-I_h. In this structure, each water molecule is hydrogen-bonded to its four nearest neighbours, with the four oxygen atoms forming an almost tetrahedral structure.[12] These oxygen atoms form a hexagonal crystal lattice, characterized by a four-sided prismatic unit cell on a rhombic base [Figure 2.5(a)]. In general, such hexagonal structures are formed by hexagonal-close packing (hcp) of molecular layers in an ABAB… sequence.[52] Nucleation of ice-I_h in supercooled droplets results in hexagonal nuclei with six-fold symmetry.[12,53]

Ice can also exist in a metastable crystalline phase known as cubic ice (ice-I_c). Cubic ice has the same tetrahedral, hydrogen-bonded structure as hexagonal ice; however, the molecular layers are cubic close-packed (ccp) in an ABCABC… sequence, giving rise to a face-centred cubic (fcc) lattice of oxygen atoms [Figure 2.5(b)].[52,54] It has

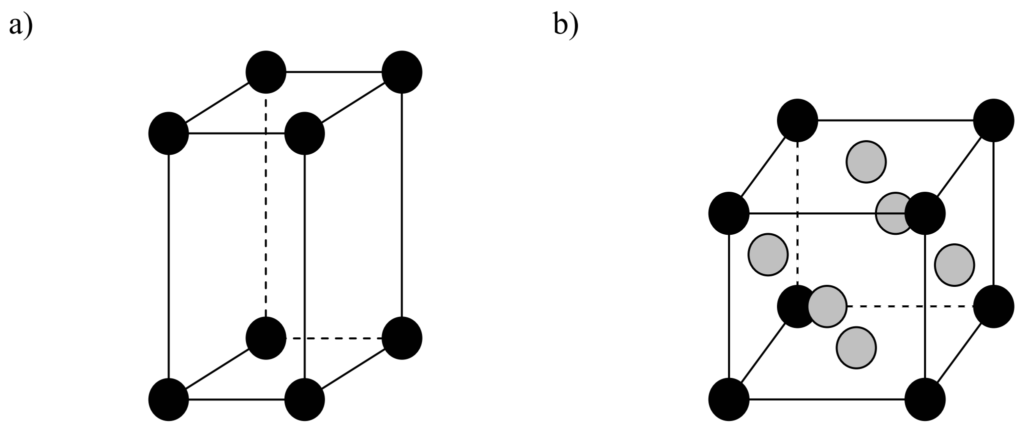

Figure 2.5: Crystal lattice structures for oxygen atoms in (a) hexagonal unit cells of ice-$\mathrm{I_h}$ and (b) face-centred cubic unit cells of ice-$\mathrm{I_c}$. Black spheres represent atoms at vertices. Grey spheres represent atoms in the centre of cell faces.

been suggested that, due to a lower free energy of formation, ice will nucleate preferentially as ice-$\mathrm{I_c}$, with crystalline nuclei of octahedral geometry.[53,54] This is known to be the case for temperatures less than ~ 180 to 190 K,[53-55] but there is mounting evidence to suggest that the nucleation of cubic ice occurs to some extent at warmer temperatures in the atmosphere.

Observations of atmospheric halos – rings and arcs of light produced by the reflection and refraction of light by ice crystals in clouds[56] – at ~ 28° from the sun or moon have pointed to the presence of metastable cubic ice at ~ 230 K.[55] These halos can only be explained by reflections from the faces of octahedral crystals formed from ice-$\mathrm{I_c}$ nuclei, as supported by computer simulations.[56] In addition, recent X-ray diffraction studies of micrometre-sized droplets suspended in oil have shown that a fraction of cubic ice is formed in pure water at 235 K.[57,58] Based on these observations, it has been proposed that the nucleation of cubic ice is an intermediate step in the formation of hexagonal ice from supercooled water droplets in the atmosphere. At temperatures above ~ 180 to 190 K, the release of latent heat during freezing can cause ice-I_c nuclei to be annealed to stable ice-I_h.[57] Alternatively, ice-I_c nuclei can serve as nucleation centres for the formation of ice-I_h.[57,59]

The formation and transformation of cubic ice in the atmosphere is of significant interest, given the higher vapour pressure of ice-I_c relative to ice-I_h (the vapour pressure of the metastable phase will be larger than that of the stable phase). The presence of both phases in clouds can lead to the growth of the latter at the expense of the former, in a Bergeron-Findeisen-type process.[25,57-59] This process will produce larger ice crystals that are more likely to sediment (settle out) and fall, resulting in the dehydration of ice clouds.

The hexagonal nuclei of ice-I_h and octagonal nuclei of ice-I_c will grow to form distinct crystal habits. The habits formed from the former, stable phase, have been characterized by laboratory studies[60] and field observations.[61-63] The majority of these habits can be considered in terms of a common shape element: the six-fold symmetric prism depicted in Figure 2.6(a).[12] Growth will occur preferentially at the basal (top and bottom) or prism planes (six sides) depending on the temperature and supersaturation with respect to ice. The term supersaturation refers to conditions in which the relative humidity exceeds 100%, in this case with respect to the saturation vapour pressure of ice (rather than the saturation vapour pressure of water, as considered previously in Equation 1.2). Common crystal habits formed from ice-I_h nuclei include the hexagonal plates, columns, and dendrites shown in Figure 2.6(b)-(d), though numerous other habits have been observed (interested readers are referred to Ref 12 and references contained therein for a detailed summary of habits and formation conditions).

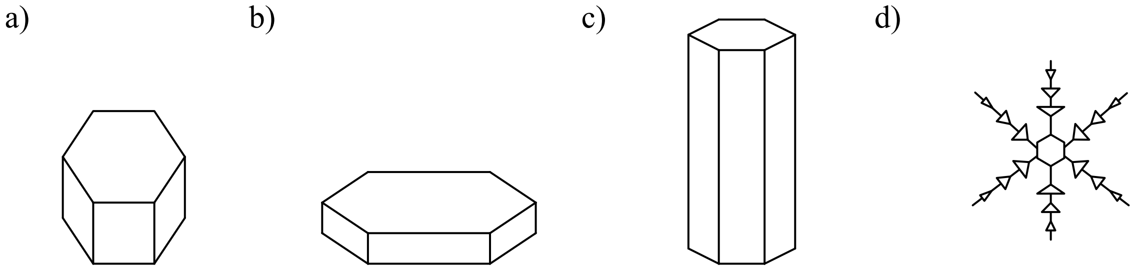

Figure 2.6: Common crystal habits formed from (a) hexagonal prismatic ice-I_h nuclei: (b) hexagonal plates; (c) hexagonal columns; and (d) dendrites.

Crystal habits formed directly from ice-I_c are less well-known, due to its rapid conversion to ice-I_h under most atmospheric conditions. Indeed, the growth of hexagonal ice-I_h on an octahedral ice-I_c nucleus is believed to be responsible for a 70.5° angle observed in common dendritic snowflakes.[59,64] The octagonal, and perhaps decagonal, crystals believed to produce the halo at ~ 28° provide the best evidence of habits formed from ice-I_c nuclei that are not converted to ice-I_h (Figure 2.7),[55,56] along with aircraft observations of crystals with distinctly cubic morphology in Antarctic ice clouds.[65]

The light scattering properties of ice crystals will vary depending on the habit(s) formed.[61,62] Crystal habit is therefore an important input parameter for climate models. For example, the assumption of hexagonal plates, rather than spheres, as the predominant particle habit in climate models results in a 0.4 K difference in the calculated global temperature.[66] Climate models typically assume "pristine" crystal habits such as those illustrated in Figure 2.6. A central problem, however, is that the use of these common crystal habits is not necessarily representative of the frequency of occurrence of habits for a given set of atmospheric conditions.[61,62] Furthermore, these pristine habits can be complicated by clumping, contact freezing, and additional vapour-phase transfer to the

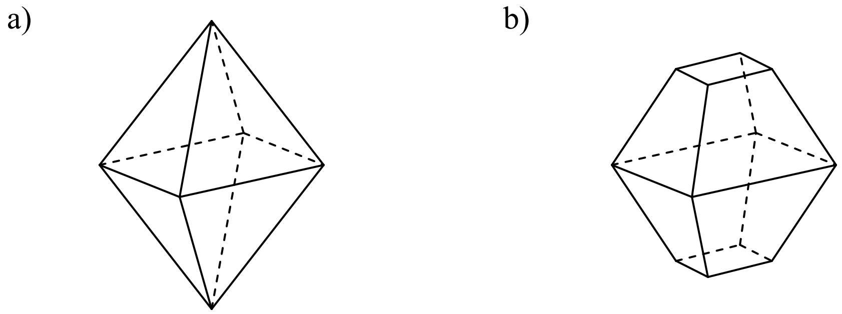

Figure 2.7: (a) Octahedral and (b) decagonal crystal habits formed from ice-I_c nuclei.

resulting agglomerates in each case. The resulting “irregular” particles will have different shapes and sizes, altering their scattering properties. Aircraft observations have shown that only a small fraction of ice crystals in natural clouds are described by pristine habits, with the majority classified as irregular particles formed by secondary processes (*e.g.* 97% irregular particles in Arctic ice clouds).[61,62] Thus, to properly assess the radiative influence of ice clouds, further knowledge of these irregular habits and their frequency of occurrence as a function of the ambient conditions is required.

2.7. Application to Cirrus Clouds

Homogeneous ice nucleation, secondary growth processes, and crystal structure and habit are all important from a fundamental standpoint, but are also directly applicable to the formation and growth of cirrus clouds. Below about 240 K, cirrus cloud particles are formed by homogeneous nucleation in pure water and dilute aqueous solution aerosols.[10,12,67,68] (In the presence of ice nuclei, such as crystalline $(NH_4)_2SO_4$,[69] nucleation can proceed heterogeneously at warmer temperatures.[12,67]) The particles then grow *via* mass transfer and collisions to form predominantly irregular crystal habits.[10] As mentioned previously, the contribution of cirrus clouds to Earth’s radiative balance is significant. Accordingly, detailed parameterization of the fundamental properties and formation processes of ice particles in cirrus clouds, as per the discussion in Sections 2.2 to 2.6, is a key requirement of climate models.

CHAPTER THREE

EXPERIMENTAL METHODOLOGY

3.1. Introduction

To simulate the conditions of the upper troposphere and lower stratosphere, a laminar aerosol flow tube apparatus with cryogenic capability is employed. The following chapter outlines this experimental approach, including the associated elements of aerosol generation, evaporation/drying, and detection. The underlying precepts of laminar flow and extinction spectroscopy are discussed, as well as the analysis procedures employed to determine the properties of aerosols (*e.g.* size, phase, refractive indices) from their extinction spectra.

3.2. Laminar Aerosol Flow Tubes

Aerosol flow tubes, or AFTs, have been used widely to study the phase transitions and physical properties of model atmospheric aerosols since their introduction for this purpose more than a decade ago.[70] The primary advantage of AFTs is the ability to study flowing particles suspended in air, eliminating potential interferences from particle contact with support media, such as oils or stages. The aerosols are typically introduced to the apparatus in a carrier gas flow, and are then conditioned at a certain temperature and relative humidity to give a desired size distribution and/or composition. The aerosols are then passed to a region where the temperature and humidity conditions are changed to initiate the process of interest, such as deliquescence, efflorescence, or freezing. Finally, the aerosols travel to the detection section, where changes in their physical properties and size distribution are observed using infrared extinction spectroscopy. The specific design and implementation of AFTs for use in the different aspects of the current study are described in the following chapters.

An important consideration in AFT studies is the establishment of laminar, or streamline, flow. As opposed to turbulent flow, laminar flow ensures that the aerosols being studied have well-defined pathways and residence times within the AFT, and hence, that the aerosols observed in the detection section have been exposed only to the desired conditions. Laminar flow is defined by the Reynolds number, Re, which gives the ratio of inertial to viscous forces for the flow of a given medium in a tube or pipe, and can be expressed in the form:[1]

$$\mathrm{Re} = \frac{ud}{\nu} \tag{3.1}$$

where u is the flow velocity, d is the pipe diameter, and ν is the kinematic viscosity (ratio of viscosity to density). For values of Re between 1 and approximately 2100, the flow will be laminar. Thus, given a certain medium and tube diameter, one can determine the range of flow velocities which will produce laminar flow conditions.

3.3. Aerosol Generation

The liquid aerosols to be studied can be generated inside the flow tube, through homogeneous or heterogeneous condensation of supersaturated vapour, or can be generated externally. An ultrasonic nebulizer (Ultra-Neb 99, DeVilbiss Co.) is used to produce particles in the 0.5 to 10 μm diameter range. A high frequency (1.63 MHz) signal is applied to a piezoelectric transducer at the bottom of a plastic reservoir filled with solution. The transducer oscillates at the frequency of the applied voltage, transferring energy to the surrounding liquid, and inducing cavitation in the surface layer. The resulting droplets separate from the bulk in the form of aerosol, which is entrained in a flow of dry nitrogen and transferred to the AFT. The aerosol output (number density, in particles cm^{-3}) can be adjusted by varying the amplitude of the applied signal. The stability of the output is sensitive to changes in the level and temperature of the liquid in the reservoir. To minimize output variability for a given signal amplitude, the liquid level is held constant using a drip-feed setup, and its temperature is held reasonably constant at ~ 313 K by running the nebulizer for ~ 30 minutes prior to introducing any aerosols to the AFT ("warming up" the nebulizer).[71]

Smaller particles (median diameter of ~ 0.3 μm) are generated using a constant output atomizer (TSI 3076, TSI Inc.), shown in Figure 3.1. In this apparatus, compressed gas is expanded through a small-diameter orifice (340 μm), forming a high velocity jet. This jet produces a low pressure region, according to the Bernoulli principle. The resulting pressure gradient between this region and an attached solution reservoir causes the solution to be drawn up through a narrow tube into the jet path. The liquid is then separated, or atomized, into a fine particle spray. The smallest droplets will evaporate by the Kelvin effect, wherein the saturation vapour pressure over the curved surface of a droplet is greater than that over a flat surface; this effect is significant for small droplets in the sub-micrometre size range (see Section 7.2.1 for a more detailed description).[12] Larger droplets will have sufficient momentum to hit the wall opposite the orifice and drain into the solution reservoir. The remaining droplets are entrained by the gas flow and exit through the top of the apparatus. If the gas pressure is held constant, the output of the atomizer is extremely stable.

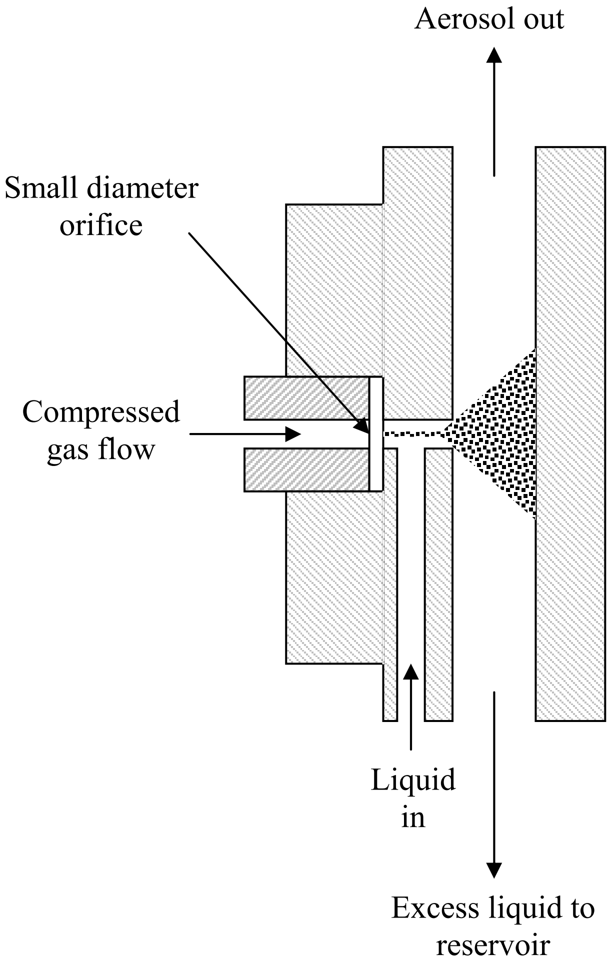

Figure 3.1: Schematic cross-section of constant output atomizer (adapted from Ref 72).

3.4. Evaporation and Drying of Aerosols

Aerosols can be partially evaporated to reduce their size, or in the case of aqueous salt solutions, completely evaporated (effloresced) to produce dry, crystalline particles. Evaporation and drying can be accomplished by lowering the relative humidity of the aerosol flow through diffusion-limited exchange with desiccants, such as silica gel and solid potassium hydroxide (KOH) pellets. The simplest implementation involves passing the aerosol flow over a bed of the hygroscopic material. To increase the drying efficiency, however, a standard diffusion dryer setup is typically employed, which increases the surface area of desiccant to which the aerosol flow is exposed. This setup comprises two concentric tubes: an inner tube composed of fine, porous mesh, through which the aerosol flow is passed; and an outer tube, capped at each end to contain the desiccant material. Silica gel can be used in either configuration, but must be periodically heated to remove adsorbed water and maintain the drying efficiency. Potassium hydroxide pellets can be used only in the bed configuration, and must be replaced intermittently, as uptake of water by this compound eventually results in the formation of basic KOH solution.

As an alternative to desiccants, dryers employing Nafion® membranes can be employed. Nafion is a synthetic copolymer with a tetrafluoroethylene (Teflon®) backbone and exposed sulfonic acid groups (Figure 2.2). The former confers resistance to chemical attack, while the latter provides selective removal of water. Each sulfonic acid group can adsorb up to 13 molecules of water; as a result, Nafion can adsorb as much as 22% of its own weight in water.

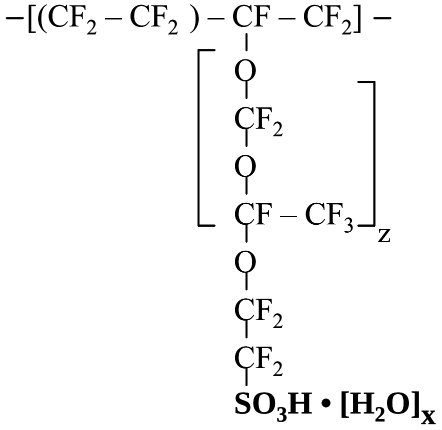

Figure 3.2: Chemical structure of Nafion® copolymer used in aerosol evaporation and drying. Sulfonic acid groups are shown in bold text. For z = 1,2,3…, x = 1 – 13.

For use in dryers, Nafion membranes can be obtained as tubing of various diameters (Perma Pure LLC). The aerosol is passed through the Nafion tubing, which comprises the inner tube in a concentric arrangement. In the outer tube, typically composed of glass, a counter-flow of dry nitrogen is passed. Water from the aerosol flow is adsorbed onto the membrane wall. The humidity gradient between the inner and outer tubes causes the adsorbed water to evaporate into the dry nitrogen counter-flow, through a process known as perevaporation. The counter-flow is then exhausted to the atmosphere, maintaining the humidity gradient. The removal of water from the aerosol flow reduces the relative humidity, resulting in the evaporation of the sample. Nafion dryers are superior to silica gel and KOH dryers, as there is no need to heat or replace the drying material. As the sole means of maintenance, Nafion dryers must be periodically rinsed with water to dissolve any salt species that may adsorb onto the membrane wall; this adsorption can reduce the drying efficiency.

3.5. Infrared Extinction Spectroscopy

The scattering and absorption of light by aerosols depend upon particle size, composition (including phase), and shape. Hence, it is possible to obtain information regarding these properties by observing aerosol interactions with light. The sum of absorption and scattering, termed extinction, results in the attenuation of light according to the well-known Beer-Lambert law, also known as Bouger's Law:[1,5,11]

$$\frac{I(\nu)}{I_0(\nu)} = \exp[-\sigma_{ext}(\nu)L] \tag{3.2}$$

where $I_0(\nu)$ is the intensity of light of a given frequency, ν, incident upon an aerosol sample, $I(\nu)$ is the attenuated intensity due to extinction, and L is the path length of light through the sample. The frequency-dependent extinction coefficient, $\sigma_{ext}(\nu)$, gives the fractional loss of light intensity per unit path length, and has units of $(\text{length})^{-1}$. Since extinction is the sum of absorption and scattering:

$$\sigma_{ext}(\nu) = \sigma_{sca}(\nu) + \sigma_{abs}(\nu) \tag{3.3}$$

where $\sigma_{sca}(\nu)$ and $\sigma_{abs}(\nu)$ are the scattering and absorption coefficients, respectively. (Equations 3.2 and 3.3 can also be considered in terms of wavelength, λ, or wavenumber, $\tilde{\nu}$, by application of Equation 1.4).

Extinction spectra give the attenuation of light by absorption and scattering as a function of the frequency of light. Spectra of aerosols in laminar flow tubes are typically obtained in the mid-infrared (mid-IR), from about 670 to 4000 cm^{-1} (2.5 to 14.9 μm). In this region, condensed phase aerosols have distinct, often broad absorption features, the locations and shapes of which provide a qualitative indication of the constituent compounds and their phases. These features may be obscured by sharp, gas-phase absorption lines, usually from water vapour and atmospheric CO_2. The spectral contribution from scattering by micrometre- and submicrometre-sized particles is significant above about 2000 cm^{-1}. The shape of the spectrum in this region gives a qualitative means of assessing particle size.

3.6. FTIR Measurements

In the present studies, extinction spectra are obtained between 460 – 6000 cm^{-1} (approximately 1.7 to 22 μm) using a Fourier-transform infrared (FTIR) spectrometer

(Bruker Tensor 37). The collimated IR beam from the spectrometer, which is modulated by a Michelson interferometer, intersects the flowing aerosols in an observation cell capped with 3.8 cm diameter KRS-5 (thallium bromide-iodide) windows, located in the detection section of the AFT. The observation path length through the cell, *L*, varies with the particular AFT configuration employed. The attenuated IR beam is then passed into a nitrogen-purged detector box, composed of stainless steel, and "floating" on a foam base to minimize electrical interference. Inside the box, the beam is focussed by an off-axis parabolic mirror onto the active area of a photoconductive mercury cadmium telluride (MCT) detector (FTIR-22-1.0, Infrared Associates, Inc.), which is cooled with liquid nitrogen to minimize thermal noise. The resulting interferogram is amplified and sent back to the spectrometer, where it is digitized and transformed into a spectrum. The spectrometer is interfaced to a laboratory PC using Ethernet cable.

Spectra are recorded and processed on the PC using Bruker OPUS software. Each spectrum is typically an average of 80 scans, collected at 2 cm^{-1} resolution and 40 kHz metrology frequency. Background spectra are obtained prior to aerosol introduction for a given set of experimental conditions. Averaging over 80 scans provides signal-to-noise ratios of 10^4 and greater, and is sufficiently rapid (on the order of about 1 minute) to minimize background instability. To obtain pure aerosol spectra, water vapour spectra recorded at the same temperatures are routinely subtracted from the measured extinction spectra. In cases where small amounts of gaseous CO_2 are present, their spectral contributions are removed by generating straight lines in the spectra between 662 – 673 cm^{-1} and 2300 – 2400 cm^{-1}.

3.7. Scattering Theories

Quantitative determination of the composition, phase, and size of aerosols from their extinction spectra can be obtained from theories of light scattering and absorption (scattering theories). The key factors governing these processes are the wavelength of light, the size of the particles, and the complex refractive indices of the material (Equation 1.3). Wavelength and particle size are considered in terms of the scattering parameter, α (Equation 1.1). Scattering theories are separated into three regimes based on the value of α:[73] (1) the Rayleigh regime for $\alpha < 0.1$; (2) the Mie regime for $0.1 < \alpha < 100$; and (3) the geometric optics regime for $\alpha > 100$.

For aerosols between 0.1 and 20 μm in diameter in the mid-IR, which is the size range of interest for the present studies, values of α fall in the Mie regime. The absorption and scattering of light by small particles in this regime is described by Mie theory, which is based on the interaction of a plane wave of radiation with spherical particles.[74] As noted previously, however, particle shape also influences the scattering properties of aerosols. Transition-matrix, or T-matrix, theory has been developed in this regard, applying the basic approach of Mie theory to aspherical particles.[75,76] The use of Mie or T-matrix theory to determine size, phase, and composition information from extinction spectra is referred to as an inversion. Inversion methods are used widely to extract fundamental information that cannot be measured directly.

3.8. Aerosol Characterization Procedure

A computational aerosol characterization procedure has been developed in our laboratory to invert experimental extinction spectra as described above. This procedure was initially designed to characterize atmospheric aerosols from IR satellite measurements,[77] but has been more recently applied to laboratory IR spectra.[78] The procedure first calculates (simulates) extinction spectra over the range 460 – 6000 cm^{-1} using Mie[74] or T-matrix[76] source code and the optical constants of the material(s) being studied. These calculations consider only forward scattered radiation (same direction as the incident light), as the extinction coefficient is greatest in the forward direction. Spectra are calculated for 96 monodisperse radii between 0.05 and 11.8 μm. The T-matrix calculations also require the aspect ratio of particles, defined as the ratio of the maximum size dimension to the minimum size dimension. In this case, spectra are calculated for 96 monodisperse equivalent spherical radii (radii of spheres having the same area as the aspherical particles) over the same size range. The resulting set of spectra in each case is referred to as the "basis set". Basis set spectra are computed for all components and phases believed to be present in a given aerosol sample. Several of the basis set spectra for liquid water aerosols are illustrated in Figure 3.3.

The procedure then considers the following least-squares minimization problem:[78]

$$\chi^2 = \min\left\{\left|K \cdot P - \tau + \gamma \cdot S \cdot P\right|^2\right\} \tag{3.4}$$

In Equation 3.4, K is an F x M matrix representing the basis set, where F is the number of frequencies for which extinction has been calculated, and M is the number of radii (96). Hence, each column in K gives the extinction spectrum for a single radius. The vector τ is the experimental extinction spectrum, which has dimensions of F x 1. The solution vector, P, has dimensions of M x 1, and is multiplied by the matrix K to give a calculated extinction spectrum, which is another F x 1 vector. Thus, P gives the contribution of the spectrum for each radius in the basis set (each column in K) to the calculated spectrum.

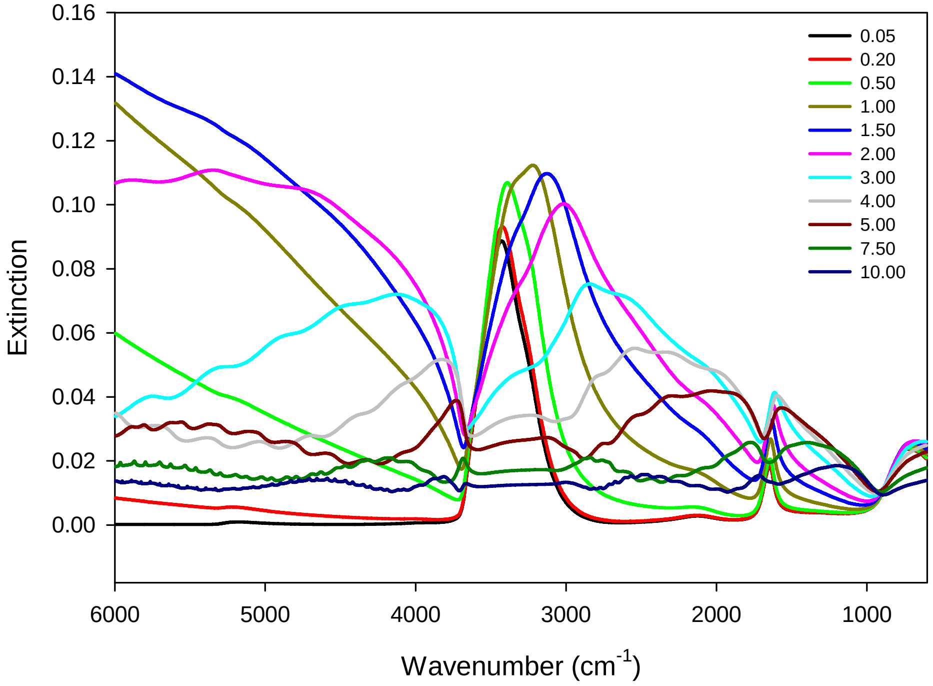

Figure 3.3: Selected monodisperse extinction spectra in the basis set for liquid water. The legend gives the corresponding particle radii in μm.

The procedure iteratively varies the value of P to minimize the sum of the squares of the differences between the calculated and experimental spectra. The "goodness of fit" between the calculated and experimental spectra is indicated by the value of χ^2. The solution vector P corresponding to the minimum value of χ^2 is output. Considered in other terms, P gives the number of particles of each radius in the basis set whose combined spectral contribution best represents the experimental extinction spectrum; therefore, P gives the particle size distribution of the sample.

The strong similarity of basis set spectra for smaller particles can lead to jagged and unrealistic size distributions.[78] The $\gamma \cdot S \cdot P$ term in Equation 3.4 is a constraint applied to smooth the output distributions without significantly affecting the quality of fit. The matrix S minimizes the third derivatives, and in turn, the jaggedness, of P. The extent of smoothing is controlled by the parameter γ. This raises questions regarding the uniqueness of the solution vector, as several values of γ may give the same χ^2 value, but different particle size distributions. To account for this, the value of γ is also varied within the procedure. As γ increases, the value of χ^2 typically reaches a minimum value before increasing. The final value of γ is chosen by the procedure when χ^2 increases by a small, user-defined percentage of the minimum value. In other words, the maximum amount of smoothing is applied that gives agreement between calculated and experimental spectra within this percentage.

For multi-component mixtures (different compounds and/or phases), the spectral contributions are additive.[78] For a sample of n components:

$$K \cdot P = (K_1, K_2, \ldots K_n) \cdot (P_1, P_2, \ldots P_n) \tag{3.5}$$

Thus, given a basis set for each component, computed using the corresponding optical constants, a particle size distribution for each compound and/or phase is output. The relative contributions of each give the fractional composition of the aerosol sample.

The particle size distributions are normalized by volume, and have units of cm^{-3}. These distributions are converted into volume distributions, in units of μm^3 cm^{-3}, by multiplying the number of particles in each of the 96 size bins by $4\pi r^3/3$, where r is the radius of the bin. The volume distributions are more representative of the aerosol samples, as extinction depends more strongly upon the volume of aerosols than the number of aerosols. In the present work, the composition of aerosol samples will be considered in terms of the volume fraction of each compound and/or phase.

Of final note, the aerosol characterization procedure is subject to minor artifacts in the output distributions.[71] Baseline shifts over the course of extinction measurements can be interpreted as extinction by large particles. This is manifested as an exponentially increasing tail towards larger radii in the output size and volume distributions. The contribution of these tails to the total volume is seldom greater than 10%. In addition, the procedure often attempts to improve small-scale discrepancies between the calculated and experimental spectra by including the spectral contribution of large numbers of the smallest particles in the basis set. This appears as a large spike in the size distributions at the smallest radii; however, the total volume of these particles is so small that these features rarely appear in the volume distributions.

3.9. Optical Constants Determination

It is also possible to determine the complex indices of refraction of materials from their IR extinction spectra. A computational inversion procedure has been developed in this regard, the details of which have been published previously.[79] The procedure is based on the iterative approach originally proposed by Clapp *et al.*,[80,81] using an "initial guess" of the $k(\tilde{\nu})$ values for a given material as a starting point. This initial guess can be obtained from a pre-existing set of refractive indices in the literature, or can be obtained directly from extinction spectra of samples that do not appreciably scatter IR light (herein referred to as "non-scattering" samples), such as small, sub-micrometre particles and thin films. The latter approach is described below. The iterative procedure is detailed in Section 3.9.2.

3.9.1. Initial Guess from Non-Scattering Samples

Recalling Equations 3.2 and 3.3, the extinction at a particular wavenumber, $E(\tilde{\nu})$, can be expressed as follows:

$$E(\tilde{\nu}) = -\ln\left(\frac{I(\tilde{\nu})}{I_0(\tilde{\nu})}\right) = \left(\sigma_{abs}(\tilde{\nu}) + \sigma_{sca}(\tilde{\nu})\right)L \tag{3.6}$$

For a non-scattering spectrum, $\sigma_{sca}(\tilde{\nu})$ = 0, and thus, the absorption coefficient at each wavenumber can be determined from the corresponding extinction value, provided the path length of light is known.

$$\sigma_{abs}(\tilde{\nu}) = \frac{E(\tilde{\nu})}{L} \tag{3.7}$$

To provide adequate signal-to-noise, samples with some residual scattering are often employed.[71] In these cases, the contribution of scattering is simulated using a fourth-order polynomial:[82]

$$E_{sca}(\tilde{\nu}) = a\tilde{\nu}^4 \tag{3.8}$$

where *a* is an adjustable parameter. The simulated scattering curve is subtracted from the experimental spectrum to yield a pure absorption spectrum.

With negligible contribution from scattering, it is assumed that the absorption coefficient at each wavenumber is directly proportional to the imaginary index of refraction, $k(\tilde{\nu})$, at that wavenumber (recall from Section 1.2 that the imaginary component is related to absorption):

$$k(\tilde{\nu}) = \frac{\sigma_{abs}(\tilde{\nu})}{4\pi\tilde{\nu}} \tag{3.9}$$

Using Equation 3.9, a set of $k(\tilde{\nu})$ values can be determined over the wavenumber range of the non-scattering extinction spectrum. These values comprise the initial guess to be used in the iterative procedure.

3.9.2. Iterative Procedure

A flow chart showing the iterative procedure for determining optical constants from extinction spectra is given in Figure 3.4. The inputs for the procedure are the initial guess values of $k(\tilde{\nu})$ (from the literature or the method in Section 3.9.1) and an experimental extinction spectrum of the material. In the procedure's inner loop, the real indices of refraction, $n(\tilde{\nu})$, are calculated from the $k(\tilde{\nu})$ values using a subtractive Kramers-Kronig (KK) transform:

$$n(\tilde{\nu}_i) = n_\infty + \frac{2P}{\pi}\int_0^\infty \frac{\tilde{\nu} \cdot k(\tilde{\nu})}{\tilde{\nu}_i^2 - \tilde{\nu}^2} d\tilde{\nu} \tag{3.10}$$

In Equation 3.10, n_∞ denotes the "anchor point," or imaginary index of refraction at infinite frequency, typically taken from a value in the visible range (~ 14000 to 25000 cm^{-1}). The term P in Equation 3.10 indicates that the Cauchy principal value of the integral is used; this corrects for singularities in the integral when $\tilde{\nu}_i$ is equal to $\tilde{\nu}$.[71]

The output set of $n(\tilde{\nu})$ and $k(\tilde{\nu})$ values are then used in the aerosol characterization procedure described in Section 3.8. A basis set of 96 monodisperse spectra is calculated using Mie or T-matrix theory, which is then iteratively fit to the experimental spectrum. The resulting χ^2 value for the fit is recorded. The $k(\tilde{\nu})$ values are then rescaled linearly by a small amount, through multiplication by a scaling coefficient, *k'*. The corresponding $n(\tilde{\nu})$ values are calculated using a KK transform, and

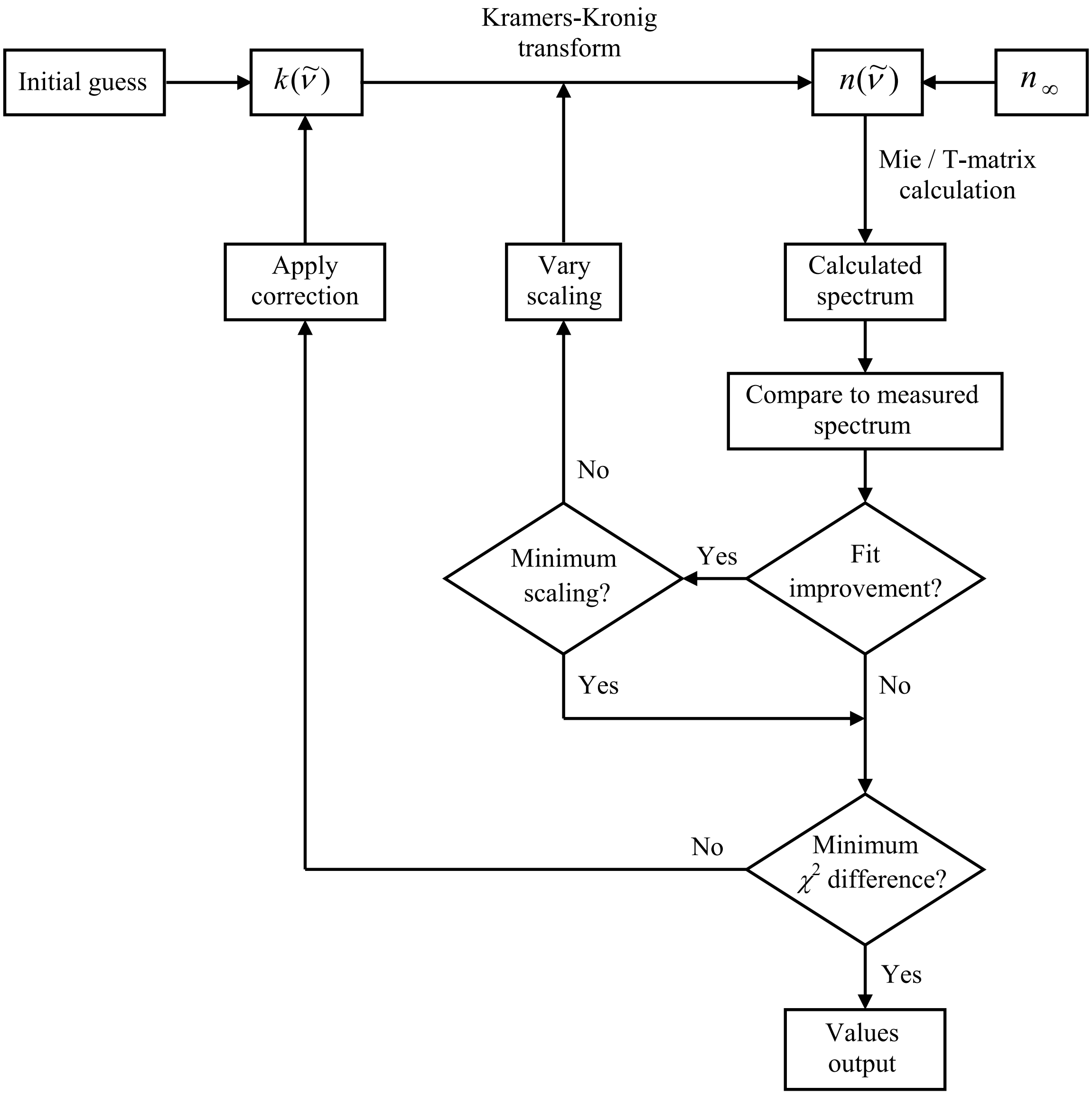

Figure 3.4: Flow chart depicting iterative procedure by which complex indices of refraction are determined from measured extinction spectra.

the characterization procedure is run again. The new χ^2 is compared against the previous value. If the new value is less than the previous value, *k'* is reduced, and the inner loop is repeated. This continues until there is no further fit improvement, or *k'* is reduced below a user-defined minimum value.

When either of the above criteria is met, the procedure continues to the outer loop. At this point, there is good general agreement between the measured spectrum and that calculated from the rescaled optical constants; however, small-scale discrepancies can still exist. It is possible to improve the agreement between measured and calculated spectra by correcting $k(\tilde{\nu})$ at each wavenumber using the approach of Dohm *et al.*.[81] This correction entails the variable rescaling of $k(\tilde{\nu})$ at each wavenumber, as opposed to the single scaling coefficient used for all wavenumbers in the inner loop. The inner and outer loops are then repeated until the difference between successive χ^2 values falls below a second user-specified minimum value. When this condition has been achieved, the final values of $n(\tilde{\nu})$ and $k(\tilde{\nu})$ are output by the procedure.

For a given material at a specified temperature, the measured extinction spectra are obtained for samples of different-sized particles. The samples should be large enough to scatter IR light, in order to constrain the values of $n(\tilde{\nu})$, which are determined from the scattering portions of spectra (above ~ 2000 cm^{-1}). The above procedure is run for each measured spectrum, and the output refractive indices are averaged. These averaged values are then taken as the final set of complex indices of refraction for the material at that temperature.

CHAPTER FOUR

CRYOGENIC FLOW TUBE DESIGN AND OPTIMIZATION

4.1. Introduction

Based on previous AFT designs developed in our laboratory,[83,84] a cryogenic AFT apparatus has been constructed which allows atmospherically-relevant temperatures to be precisely set and controlled. The design and operating conditions have been carefully considered with respect to the establishment of laminar flow, and the minimization of disturbances in the flow due to mixing and variations in temperature. This aspect of the study was guided by computational fluid dynamics (CFD) simulations, in collaboration with colleagues in the Department of Mechanical Engineering, University of Waterloo. The CFD simulations allow easy manipulation of experimental variables such as tube geometry, temperature, and flow rate, and analysis of the resulting temperature and velocity profiles in the gas flow. The following chapter outlines the apparatus construction, temperature and flow control systems, and modifications based on the CFD simulations. The simulation results are provided for illustrative purposes; the reader is referred elsewhere for the specific details of the model geometry and boundary conditions.[85,86]

4.2. Cryogenic Aerosol Flow Tube Apparatus

The cryogenic aerosol flow tube apparatus is shown in Figure 4.1. The flow tube consists of four, thermally-conductive copper sections, each 37.5 cm long, with an inner diameter (i.d.) of 8.9 cm. The copper sections are joined and thermally isolated by thin-

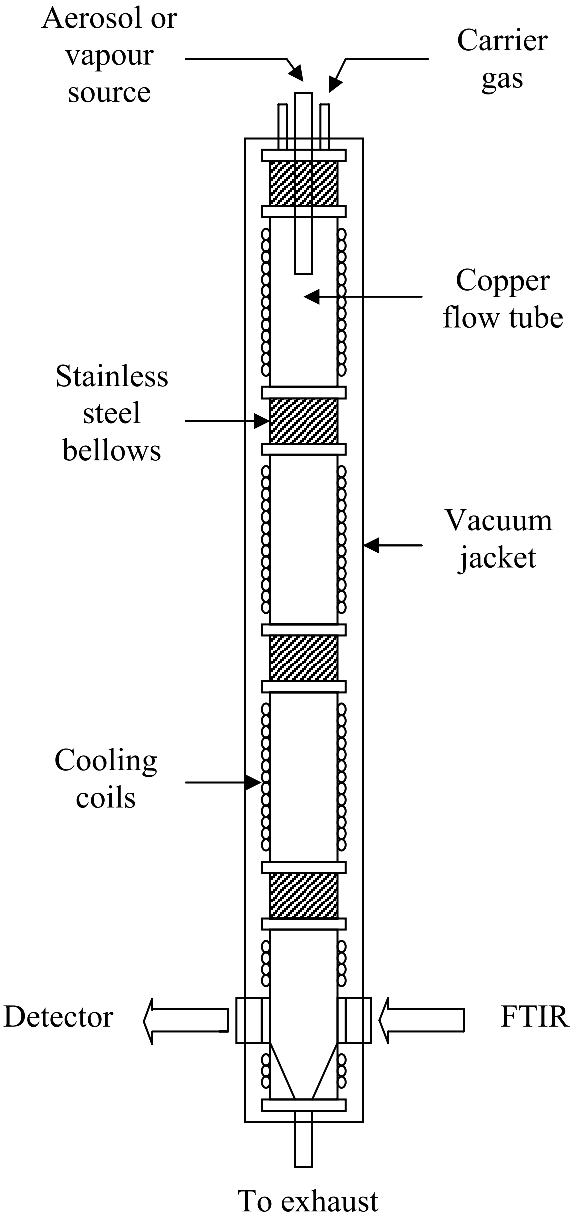

Figure 4.1: Schematic representation of cryogenic aerosol flow tube apparatus.

walled stainless steel bellows (7.0 cm long, 8.9 cm i.d.). Each copper section is connected to a bellows using stainless steel mating flanges, sealed with spring-loaded PTFE/Teflon® coated O-rings (American Variseal Corp.). These seals maintain their integrity under cryogenic conditions; the elasticity of the metal spring compensates for thermal variations in the hardware.

The flow tube and bellows comprise the inner assembly, which is enclosed within a vacuum jacket composed of 21.9 cm i.d. stainless steel pipe. Annular nylon supports located at the bottom of each section hold the inner assembly in the jacket centre. The jacket is evacuated by a mechanical pump and roots blower to approximately 0.1 hPa, preventing conductive heat transfer between the flow tube and the laboratory environment. Additionally, the inner assembly is wrapped with a few layers of aluminized Mylar® film to reduce radiative heat transfer from the vacuum jacket to the flow tube.

The vacuum jacket is divided into four, 45.7 cm long sections, each enclosing one copper tube section and bellows. Adjacent jacket sections are joined by stainless steel mating flanges, and sealed with Buna O-rings. Each jacket section is equipped with two 15.2 cm diameter stainless steel access ports, offset by 90 degrees (front and side). The ports are capped with stainless steel end plates, and sealed with Buna O-rings. Each end plate is fitted with an eight-pin feedthrough for four thermocouples, and two feedthroughs for cooling lines to enter and exit the inner assembly. These thermocouples and cooling lines are both implemented in the temperature control system (Section 4.3).

The bottom section of the flow tube is equipped with optical ports for spectroscopic observation. These ports are located 25.4 cm below the top of the section, on opposite sides of the flow tube. The ports comprise 6.4 cm i.d. stainless steel bellows, sealed on the outside with KRS-5 windows. A slow flow of nitrogen is directed towards the inner surface of each window from four points arranged around the window perimeter to prevent vapour condensation and aerosol deposition (window purge flow; see Section 4.4). The region between the windows comprises the observation cell. The IR beam intersects a cylindrical section of the aerosol flow in this region, and extinction spectra are acquired using the setup and methods described in Section 3.6. The observation path length, L, is 8.9 cm, corresponding with the inner diameter of the flow tube.

4.3. Temperature Control System

A schematic drawing of the flow tube temperature control system is shown in Figure 4.2. A mixture of liquid and gaseous nitrogen from an external reservoir is supplied at ~ 700 kPa through an insulated line to a 30 L stainless steel Dewar. A cryogenic solenoid valve (8222G2LT/AC, Asco Valve Inc.) controls the flow of nitrogen coolant into the Dewar. The relative proportion of liquid to gaseous nitrogen varies with the consumption rate; the greater the refrigerant flow, the more liquid nitrogen passes into the Dewar. At typical flow rates employed to maintain flow tube temperatures in the vicinity of 240 to 230 K, the nitrogen flow is primarily gaseous.

Immediately following the Dewar, the coolant flow is split into four separate lines – one for each section of the flow tube – composed of 1.3 cm i.d. copper pipe. The flow through each line is controlled manually using a Swagelok bellows valve (SS-BNS4) and a flow meter (model 5671003-01-001, Controls Corporation of America) located after the flow tube. The cooling lines are connected to the feedthroughs on the jacket end plates of each section described above. Inside the vacuum jacket, the chilled nitrogen is delivered to cooling coils on each section *via* a 30.5 cm length of 1.3 cm i.d. thin-walled, convoluted stainless steel tubing (Swagelok Co.).

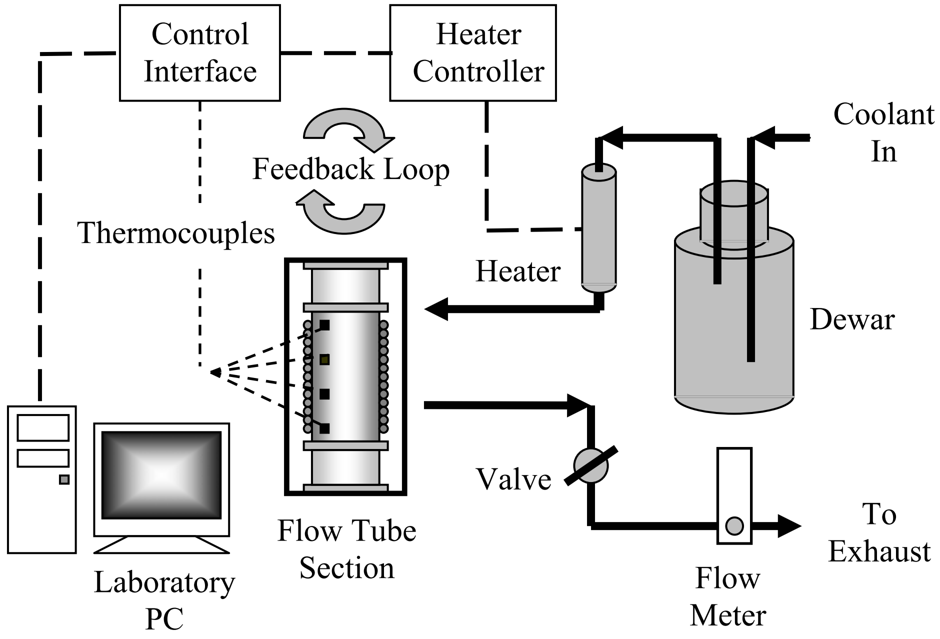

Figure 4.2: Schematic diagram of temperature control system. Solid, long-dashed, and short-dashed lines represent the coolant flow, LabVIEW control pathway, and temperature readings, respectively.

The cooling coils are composed of 0.6 cm i.d. copper tubing wrapped around the outer wall of each copper section and secured with thermally-conductive epoxy (Stycast® 2850 FT, Emerson and Cuming). Two concentric coils are employed. The coolant is introduced at the top of the outer coil, flows downward, and from the bottom it is transferred to the top of the inner coil, through which it flows downward again. Tests of different coolant flow configurations indicate that this parallel flow provides the most efficient and uniform cooling relative to alternative pathways. After circulating through both coils, the nitrogen coolant exits at the bottom of the inner coil and leaves the apparatus *via* a second 30.5 cm length of convoluted stainless steel tubing connected to the second feedthrough on the jacket end plate. At the exit, it passes through the flow control valves (bellows and flow meter) described previously before being exhausted to a laboratory fume hood.

This cryogenic AFT system has the ability to maintain temperatures ranging from 100 to 300 K. The independent cooling of individual sections allows a wide variety of axial temperature profiles to be employed. Fine temperature control is achieved through the use of 400 W in-line electrical heaters (AHP-5051, Omega Engineering, Inc.) located along the inlet cooling line of each section. Voltage applied to the heaters by an electrical controller warms the coolant gas flow. To prevent overheating, thermocouples attached to the body of each heater are monitored by the controller, and should the temperature exceed the set threshold (typically 323 K), the heater voltage is removed.

The temperatures of the AFT sections are monitored using sixteen type T (copper/constantan) thermocouples (Special Limits of Error wire, Omega Engineering, Inc.) – four per section – attached to the outer wall of the copper flow tube. For each section, the first thermocouple is 5.1 cm from the top and the remaining three are located at 8.9 cm intervals below it. Each thermocouple is secured by a thin loop of copper wire soldered to the tube wall and aluminum adhesive tape. The thermocouples are accurate to within ± 0.5 K. To improve the accuracy of temperature readings, these thermocouples are calibrated against a thermistor accurate to within ± 0.1 K (Omega Engineering, Inc.).

The thermocouples and heaters are integrated via a FieldPoint Modular Distributed Input/Output interface (National Instruments FP-1601, FB-TC-120, and FP-TB-10), and operated by LabVIEW code. This code allows the temperature of each section to be independently monitored, set, and controlled. Following initial equilibration, the average temperature of a section wall typically remains within ± 0.1 K of the set-point. Direct measurements show that axial temperature deviations along a section are within ± 0.5 K.

4.4. Flow Control

The total nitrogen flow through the AFT is controlled by a mass flow controller (810 C Mass-Trak, Sierra Instruments, Inc.) operated *via* the FieldPoint Modular Distributed I/O interface by LabVIEW code, or a mass flow meter (FMA 1824, Omega Engineering, Inc.) regulated with a needle valve. After passing through the mass flow controller/meter, the nitrogen flow is split into separate streams for the bulk carrier gas, humidified gas, nebulizer, and window purge flows. These flows are controlled independently using a series of floating-ball flow meters (Advanced Specialty Gas Equipment FM4333 and FM4334). The humidified gas flow is produced by passing dry nitrogen gas through a heated water container, and can be used as a carrier flow to increase the relative humidity inside the flow tube, or purely as an aerosol source flow to be condensed homogeneously or heterogeneously inside the cooled flow tube. The atomizer is driven by a separate dry nitrogen flow, which is precisely controlled using a pressure gauge to minimize variations in output.

Typical total flow rates used in the present study are in the vicinity of 10 standard litres per minute (SLPM), with standard conditions specified as 293 K and 101.3 kPa. The corresponding flow velocity is ~ 3 cm s^{-1}, resulting in Re ~ 157, which is well within the laminar regime. Under these conditions, the residence time of particles in the flow tube is about 55 s, which is sufficiently long for the wall temperature to be transferred to the gas (see Section 4.6). The total flow is generally divided into 7 SLPM dry and/or humidified carrier gas flow and 3 SLPM aerosol or aerosol source flow. The window purge flow is 0.05 SLPM, and is considered separately from the 10 SLPM total flow described above. A backing pressure of 35 pounds per square inch (psi) (241.3 kPa) is used to generate an atomizer flow of 3 SLPM.

The aerosol or aerosol source flow is introduced to the apparatus *via* a heated, 50.8 cm long stainless steel inlet. The inlet comprises two concentric tubes: a 2.5 cm o.d. inner tube delivers the aerosol flow, and a 3.8 cm o.d. outer tube encloses the inner tube and heating assembly. This assembly consists of three wire-wound silicon rubber heaters (Minco Products, Inc.) affixed to thin copper sheets, and wrapped around the inner tube. Each heater is controlled independently using one of three Powerstat® Auto Transformers. The inlet enters the top section of the flow tube through a 3.8 cm i.d. Quick Disconnect adaptor (MDC Vacuum) located in the centre of the flow tube lid. The lid itself is a 17.1 cm diameter stainless steel plate, sealed to the top of the vacuum jacket with a spring-energized PTFE/Teflon® coated O-ring.

4.5. Inlet Design

As described above, the aerosol or aerosol source flow is introduced through an inlet in the centre of the tube axis. The means of introducing the carrier gas must be considered carefully, as the mixing of aerosol and carrier flows can potentially disrupt the laminar profile in the inlet region. The aerosols are either created, or their sizes are adjusted, in the inlet region, so it is important that the conditions here are well-controlled.

To assess the influence of inlet configuration, flow profiles in the inlet region were modelled using CFD. The initial flow tube design used a side inlet to introduce the carrier gas flow. This type of configuration can cause recirculation of the gas, as illustrated in Figure 4.3(a). Recirculation in the inlet region can lead to significant particle growth in two ways: first, particles produced by homogeneous or heterogeneous nucleation of supersaturated vapour can experience additional growth if they return to the region of the tube in which they were formed; and second, recirculation leads to collisions between aerosol particles, causing agglomeration. The net result is that the particles become bigger, and their number density decreases in an uncontrollable manner. To reduce the potential for recirculation, we designed a coaxial inlet in which the aerosol and carrier gas are both introduced along the axis of the flow tube. Figure 4.3(b) shows that for the specific case modelled, this type of configuration eliminates recirculation in the inlet region.

The actual implementation of the axial inlet design differs from that depicted in Figure 4.3(b). In the current design, the carrier gas is introduced through four, equally-spaced, 1.3 cm i.d. inlets on the flow tube lid. These inlets are positioned on a 3.8 cm diameter circle around the central aerosol inlet. Below the lid, the carrier gas is pre-cooled by passing around a 7.6 cm long cylindrical coil of 0.6 cm i.d. copper tubing connected to the outlet of the top section cooling line. In this way, the temperature of the coil is automatically adjusted upon changes in the temperature of the top section. The pre-cooling of carrier gas reduces the time required for the gas to attain the wall temperature of the top tube section. The aerosols are introduced below the coil through the inlet described above. Mixing with the pre-cooled gas provides faster, more efficient cooling of the aerosol flow.

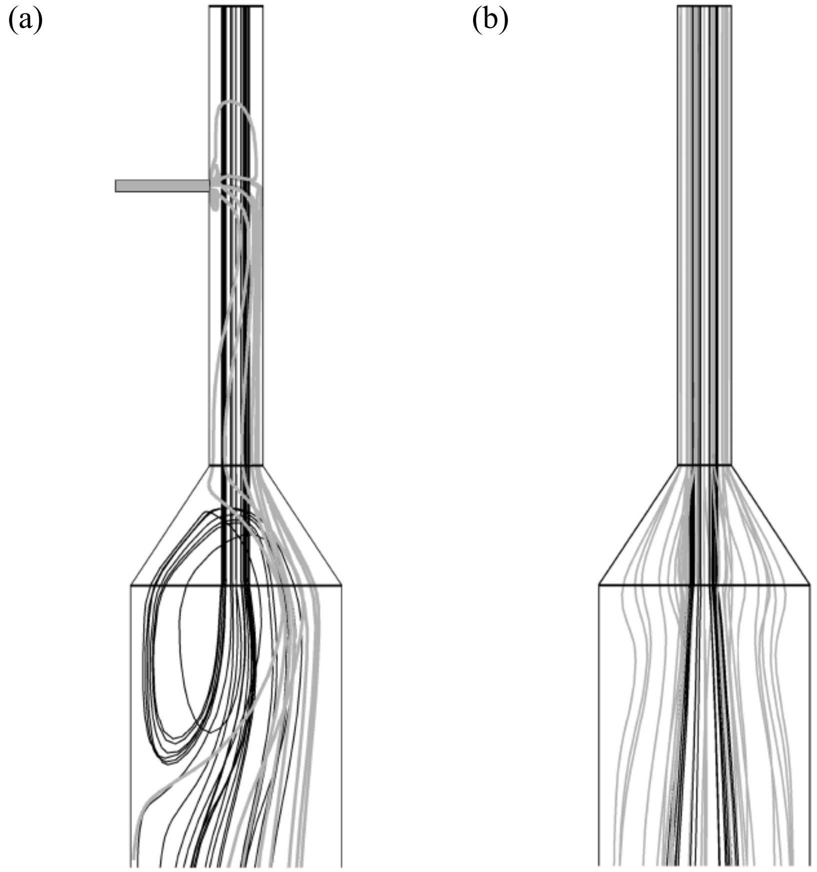

Figure 4.3: CFD model results showing flow patterns using (a) side and (b) axial inlet designs. Black and grey streamlines represent the aerosol (3 SLPM) and carrier gas flows (1 SLPM), respectively.

4.6. Wall-to-Gas Heat Transfer

Beyond the inlet region, the cooling efficiency is determined by heat transfer from the walls to the gas in the tube interior. Residence times are sufficiently long to ensure that the aerosols acquire the desired wall temperature; however, the large diameter of the tube results in radial temperature gradients in which the flow is coldest at the tube walls and warmest in the centre. Radial temperature gradients promote buoyancy effects in the flow. Figure 4.4 shows a CFD simulation of velocity and temperature profiles for a

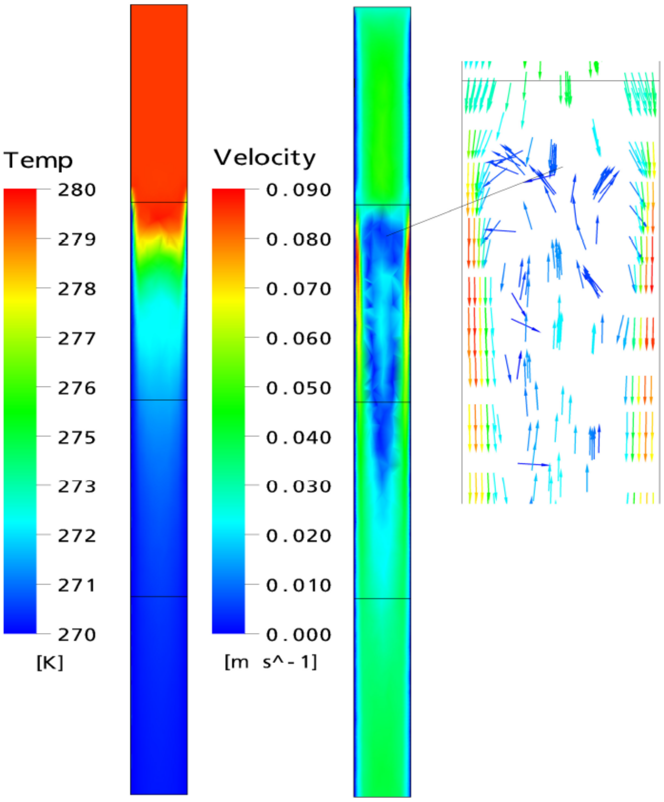

Figure 4.4: CFD model results for a typical cooling scenario in the cryogenic flow tube (mean flow velocity of 3 cm s^{-1}, inlet temperature of 280 K, wall temperature of 270 K, and flow tube diameter of 8.9 cm). The inset shows the recirculation present under these conditions.

cooling scenario in which the top tube section is held at 280 K, while the lower three sections are held at 270 K. The colder gas near the wall is more dense, and travels downward more quickly relative to the gas in the centre. If the downward mass flow rate near the wall becomes high enough, mass conservation requires that the flow in the centre of the tube moves upward, creating a recirculation zone (inset of Figure 4.4). This buoyancy-induced recirculation facilitates heat transfer between the gas and tube wall, but causes the residence time for the aerosol particles to be undetermined, and can lead to significant particle growth.

The extent of buoyancy-induced recirculation can be considered analytically using the buoyancy parameter:[87]

$$\frac{\mathrm{Gr}}{\mathrm{Re}^2} = \frac{\left[g\beta L^3 \Delta T / \nu^2\right]}{\left[\rho \bar{u} L / \mu\right]^2} \tag{4.1}$$

where Gr is the Grashof number (the ratio of buoyancy to viscous forces), Re is the Reynolds number, g is gravity, β is the volumetric thermal expansion coefficient, L is the characteristic length of the geometry (in this case, the diameter of the flow tube), ΔT is the temperature difference between the tube wall and flow, ν is kinematic viscosity, ρ is density, $\bar{u}$ is average velocity, and μ is molecular viscosity. The buoyancy parameter, Gr/Re^2, is a dimensionless value that compares the strength of buoyancy forces with that of inertial forces. When Gr/Re^2 is greater than unity, the flow is dominated by buoyant forces. A radial temperature difference of 1 K in our 8.9 cm diameter flow tube yields Gr/Re^2 ~ 4.5 for a flow velocity of 3 cm s^{-1}, accounting for the recirculation observed in Figure 4.4.

From Equation 4.1, the buoyancy parameter is proportional to the tube diameter and the temperature difference, and inversely proportional to the square of the average velocity. Thus, buoyant recirculation in the flow can be suppressed by using faster flow velocities and/or smaller tube diameters. Implementation of the former will increase the value of Re and decrease particle residence times, both of which are undesirable, and so the latter approach was employed. A set of cross-shaped copper fins was placed in each section of the flow tube as shown in Figure 4.5, reducing both the tube diameter and radial temperature difference by factors of approximately two. The corresponding value

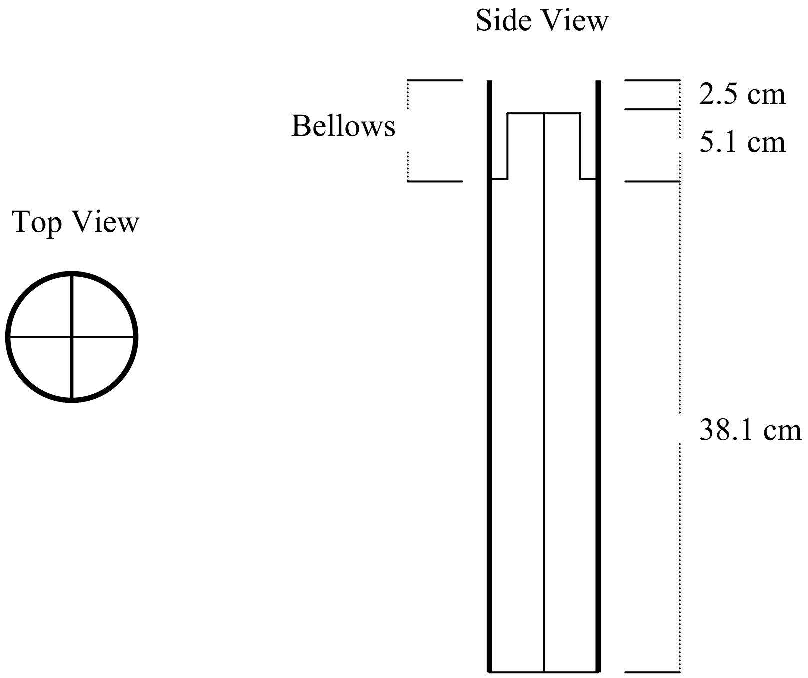

Figure 4.5: Top and lateral views of a flow tube section with copper fins inserted.

of Gr/Re^2 is ~ 1.1, indicating that from an analytical standpoint, the effects of buoyancy-induced recirculation should be minimized.

Figure 4.6 shows the CFD analysis of temperature and velocity profiles for the flow tube configuration with fins. In this case, the second tube section was held at 246 K, and the third section was held at 236 K. The fins cool the flow close to the central axis, reducing radial temperature gradients, and preventing the formation of recirculation zones. It can be seen from Figures 4.5 and 4.6 that the fins extend into the bellows between the sections, without touching the bellows wall. These extensions begin to cool the gas prior to its introduction to the lower section, providing a smoother temperature transition between the sections. Indeed, the addition of fins propagates the wall

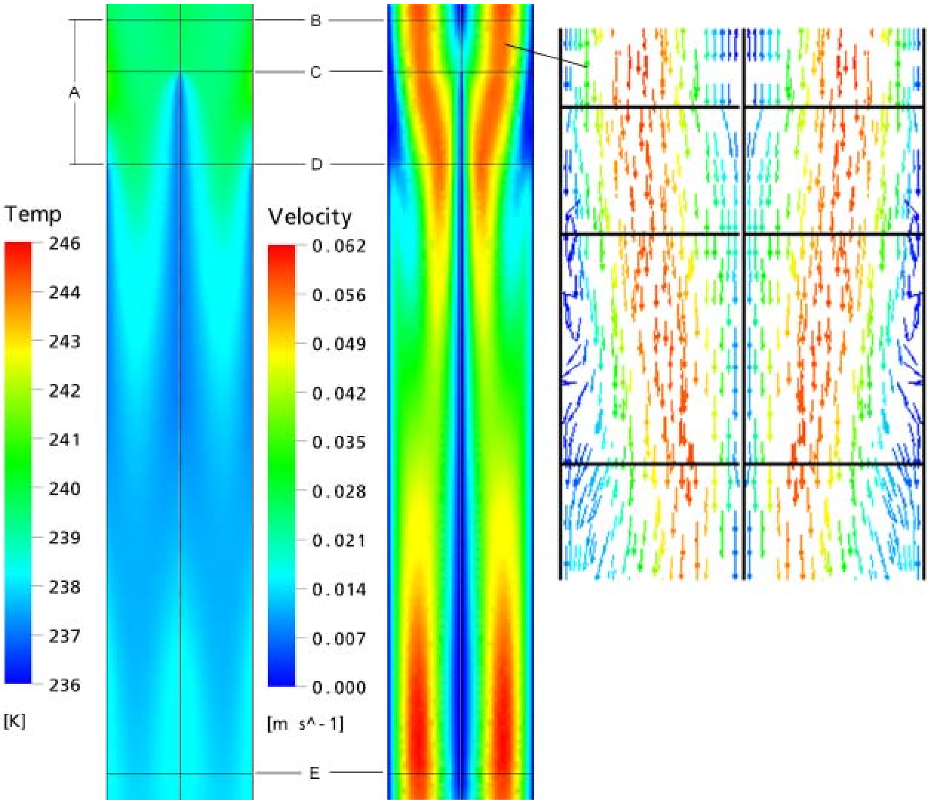

Figure 4.6: Temperature and velocity profiles within the flow tube after the addition of fins (flow velocity of 3 cm s^{-1}, inlet temperature of 246 K, wall temperature of 236 K, and flow tube diameter of 9.0 cm). Location designations are as follows: A – bellows region; B – end of second section; C – fins begin; D – third section begins; E – third section and fins end.

temperature of the lower section radially in approximately 40% of the time required in their absence.

One must note that the fin configuration depicted in Figures 4.5 and 4.6 applies only to the two middle sections of the flow tube. In the top section, the fins are soldered to the bottom of a length of 5 cm diameter pipe, through which the aerosol inlet is passed. The pipe fits inside the copper pre-cooling coil. In the bottom section, a 5 cm diameter hole is cut in the fins at the axial position of the observation ports to avoid obscuring the optical pathway. This hole maintains the aerosol observation path length at 8.9 cm, avoiding the reduction in path length, and hence, detection sensitivity, that typically accompanies reductions in tube diameter.

Regardless of the specific configuration, it is evident from Figure 4.6 that the coldest temperatures are found at the tube wall and fins. These cold surfaces can thus serve as sinks where vapour can condense and/or freeze (creating a water or ice coating), depending on the aerosol properties and experimental conditions. The inclusion of fins significantly increases the available surface area for condensation and/or freezing to occur. Overall, however, the benefits of minimizing recirculation in the flow compensate for diffusive losses, which can be accounted for analytically (see Section 7.2.1).

4.7. CFD Model Validation

To validate the CFD model, simulated axial temperature profiles were compared against direct measurements made in the flow. In the particular case investigated, the top two sections of the flow tube were held at 240 K, and the bottom two sections were held at 235.5 K. A total flow rate of 10 SLPM (mean flow velocity of 3 cm s^{-1}) was employed. Direct measurements of the interior wall and centreline flow temperatures were made within one quadrant of the cryogenic AFT under the prescribed conditions. For the wall measurements, a type T thermocouple was affixed to one end of a flexible, V-shaped attachment on an extendable rod. The attachment spread open within the quadrant, pressing firmly against the tube wall on one side, and the fin joint in the tube centre on the other side. For the centreline measurements, a type T thermocouple on an extendable rod was housed in the centre of a Teflon® coil, maintaining the thermocouple in the quadrant centre, and preventing any contact with the wall and fins. The measured axial interior wall temperatures were then used in the CFD simulation as boundary conditions, conducted using identical geometry (tube quadrant) and flow velocity.

The comparison between the measured and simulated centreline temperature profiles is shown in Figure 4.7. The two profiles show excellent agreement, thereby validating the CFD model. It is also important to note how the centreline temperatures lag behind the interior wall temperature upon passing into the colder section. This demonstrates that one cannot determine the residence time of aerosols at a given temperature based solely on the flow velocity and the axial distance of the section maintained at that temperature; the time required for wall-to-gas heat transfer must be taken into account. This is extremely important when modelling the kinetics of aerosol transformations such as nucleation, which are highly temperature-dependent. Also important in modelling studies is the use of mass-averaged temperature profiles (dotted line in Figure 4.7) rather than centreline profiles, as the aerosols are spread out over the entire tube cross-section. Modelling studies in the present work are discussed further in Chapter 7.

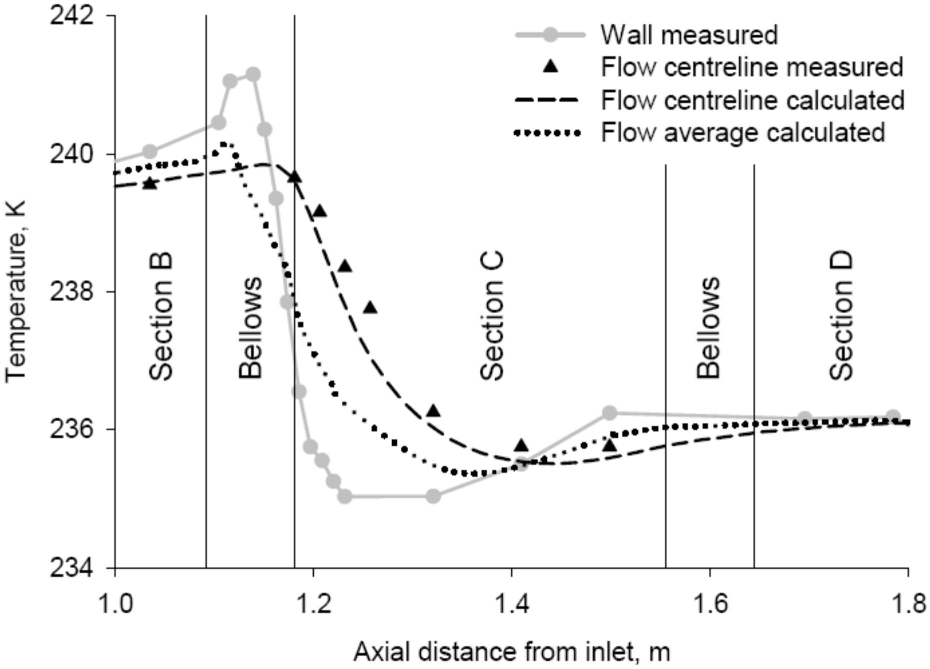

Figure 4.7: Comparison of measured and calculated axial temperature profiles in one quadrant of the flow tube (flow velocity of 3 cm s^{-1}, section B held at 240 K, sections C and D held at 235.5 K). Note that tube sections are labelled A – D, top to bottom.

CHAPTER FIVE

FREEZING OF SUPERCOOLED WATER AEROSOLS

5.1. Introduction

To assess the dependence of homogeneous nucleation on particle volume and/or surface area and temperature, freezing experiments are conducted wherein these variables are manipulated. In the present work, particle radius, and in turn, the surface-to-volume ratio of particles, is varied by changing the means of aerosol generation. The cryogenic aerosol flow tube is then used to expose the particles to well-defined temperature conditions. The onset and extent of freezing can be determined directly from extinction spectra, or from the aerosol characterization procedure described in Section 3.8. The latter provides additional information about the size of particles, which are subject to growth by mass transfer.

To validate our experimental approach, the nucleation, or freezing, points determined using the above methods are compared with relevant values in the literature. Cziczo and Abbatt studied the freezing of micrometre-sized water aerosols produced from a constant output atomizer using a similar temperature-controlled flow tube apparatus.[15] The nucleation point was determined by inspection of temperature-dependent changes in extinction spectra to be 234 K. In addition, previous studies of droplet freezing in expansion cloud chambers by DeMott and Rogers[27] and Anderson *et al.*[88] showed nucleation at 239 K and 233 K for droplets with radii of 5 μm and 1 μm, respectively.

5.2. Experimental

In all freezing experiments, the top two sections of the cryogenic AFT are held at 240 K to condition the aerosols. This ensures that all particles are exposed to the same initial conditions, and are cooled sufficiently to provide smooth temperature transitions into the lower two sections, where the temperature is varied between 240 – 233 K (candidate freezing temperature). As discussed in section 4.4, a total flow rate of 10 SLPM is used, with 7 SLPM carrier flow and 3 SLPM aerosol flow. The aerosols are generated by nebulization or atomization of Millipore®-filtered water, or by the heterogeneous condensation of humidified carrier gas on ~ 20 nm dry sodium chloride (NaCl) particles. In the latter case, the condensation nuclei are produced by atomizing a dilute, 10^{-4} mol L^{-1} (M) solution of reagent-grade NaCl (Sigma-Aldrich Co.) in Millipore®-filtered water, and passing the aqueous particles through a 60 cm long Nafion dryer. Extinction spectra of the flowing aerosols are obtained in the bottom section of the AFT. Similar to the case outlined in Section 4.7, CFD simulations of cooling scenarios covering the range of candidate freezing temperatures have shown that the residence times of aerosols in the bottom two AFT sections are sufficiently long (approximately 35 s) for the aerosols to acquire the desired temperature prior to spectroscopic observation.

5.3. Results and Discussion

5.3.1. Temperature-Dependent Changes in Extinction Spectra

The evolution of aerosol extinction spectra as the candidate freezing temperature is successively reduced is illustrated in Figure 5.1. The specific case shown is for water aerosols produced directly from the atomizer; however, the changes in absorption

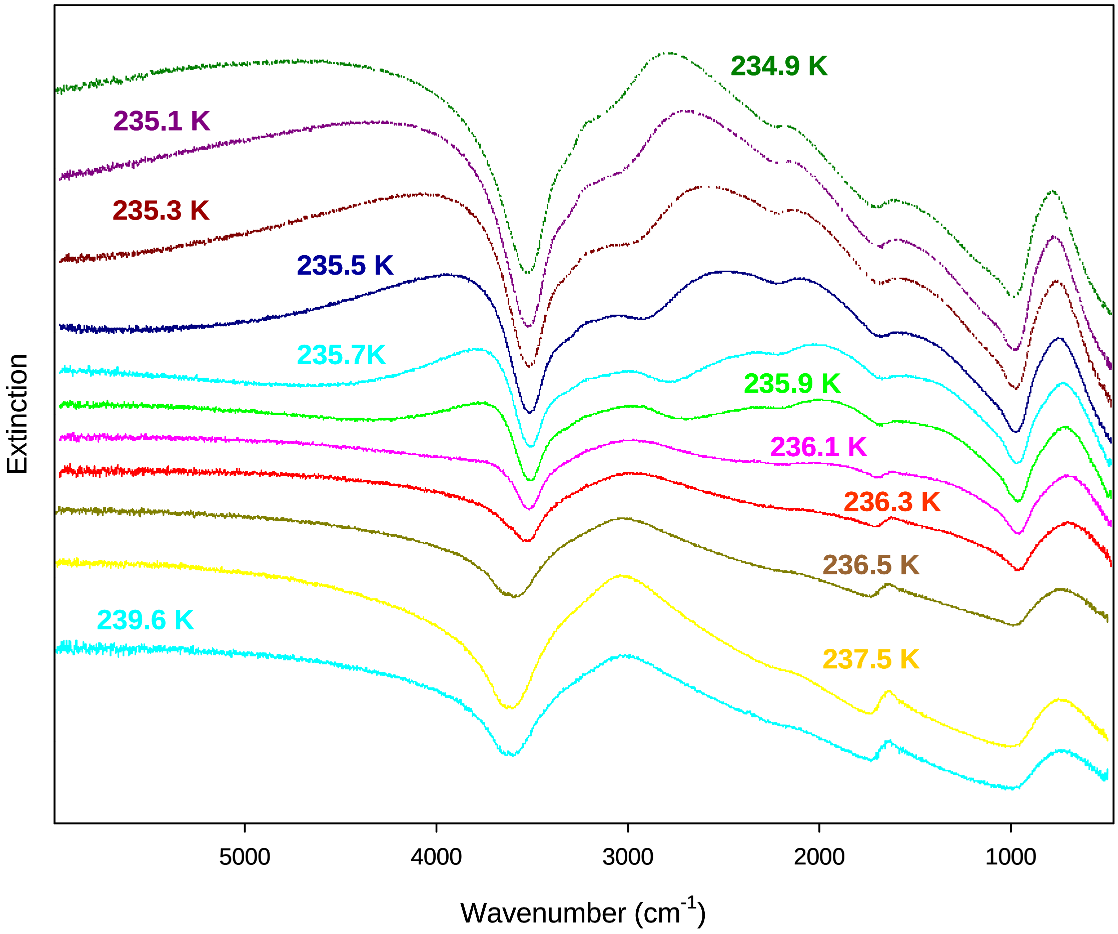

Figure 5.1: Temperature-dependent changes in extinction spectra of aerosols obtained from atomization of pure water. Spectra are scaled and offset for clarity, with labels above each spectrum indicating the candidate freezing temperature.

features signifying the freezing onset are the same, regardless of aerosol size. The changes of interest are: (1) the stretching feature at ~ 3400 cm^{-1}, characterized by changes in the O-H bond lengths of water molecules, broadens and shifts to lower wavenumbers; (2) the bending feature at ~ 1640 cm^{-1}, characterized by changes in the H-O-H bond angle, broadens; and (3) the librational feature at ~ 700 cm^{-1}, characterized by the hindered tilting and rotation of hydrogen-bonded water molecules, sharpens and shifts to higher wavenumbers. These changes in absorption features are all in accordance with the observations of Cziczo and Abbatt,[15] and previous observations by Clapp *et al.*.[80] The distinct changes in shape that occur above about 4000 cm^{-1}, where water and ice do not absorb, are due to changes in scattering. This is reflective of changes in particle size due to mass transfer. As discussed in Section 2.5, mass transfer growth is most significant near the homogeneous nucleation point, and is gradually suppressed upon cooling to lower temperatures.

Visual assessment of Figure 5.1 suggests that freezing begins at 236.1 K. Small, yet distinct, variations in the absorption features of interest are observed as the candidate freezing temperature is reduced from 239.6 K, but it is not until 236.1 K that these features begin to change appreciably. In addition, the drastic changes in the scattering region due to mass transfer growth indicate that nucleation has occurred at or above 235.9 K.

Based on the assessment above, the extinction spectra undergo the most significant changes at the homogeneous nucleation point. This provides the basis for the determination of freezing points from the temperature-normalized variance of difference spectra.[89] In this method, extinction spectra obtained at successively lower temperatures are subtracted from one another, and the variance of each difference spectrum over a given wavenumber range is plotted against the average temperature of the two spectra. The freezing point is taken as the average temperature at which the maximum variance occurs. Application of this method to the extinction spectra from freezing experiments employing the three separate means of aerosol generation gives the variance plots shown in Figure 5.2. The variance of the difference spectra was taken over the range 470 – 3300 cm^{-1}. In each case, the point of maximum variance, and hence, the homogeneous nucleation point, is at approximately 236.2 K. For the atomizer data, this is in excellent agreement with the visual assessment of the freezing point from Figure 5.1. Moreover, the freezing points determined for all three data sets are in good general agreement with the literature values, which range from 233 to 239 K, thereby validating our experimental approach and methodology.

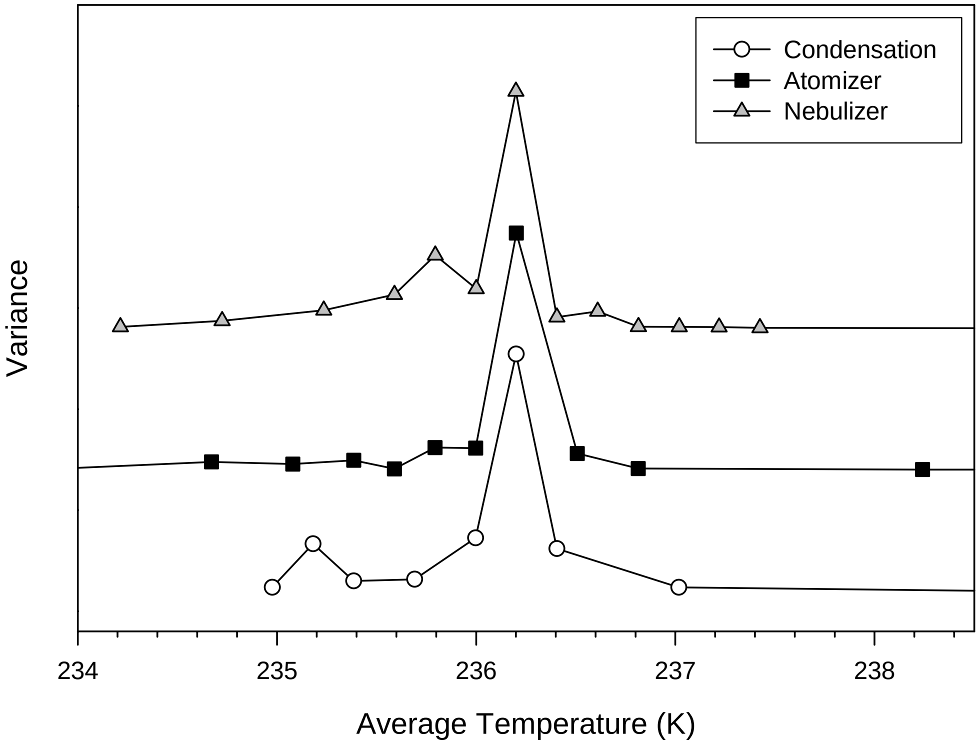

Figure 5.2: Temperature-normalized variance of difference spectra for aerosols produced by condensation, atomization, and nebulization. Variance was taken over the range 470 – 3300 cm^{-1}. Curves are scaled and offset for clarity.

5.3.2. Results from Characterization Procedure

A second appraisal of the nucleation points was conducted using the aerosol characterization procedure (Section 3.8). Basis set spectra were generated for water and ice using Mie theory and the optical constants of Bertie and Lan for water at 300 K,[90] and the values of Warren for ice at 240 K.[91] Both components were used to calculate fits to experimental spectra. A sample fit obtained from the procedure is shown in Figure 5.3 for a freezing trial in which aerosols produced by heterogeneous condensation on NaCl nanoparticles were cooled to a candidate freezing temperature of 237.5 K. The excellent agreement between the measured and calculated extinction spectra ($\chi^2 \sim 0.1$ for $\gamma = 0.02$) is representative of the general quality of fits produced by the characterization procedure. The corresponding particle number and volume distributions output by the procedure are given in Figures 5.4 and 5.5, respectively. These distributions provide information regarding the size and composition (phase) of aerosol samples. In the present studies, this information is typically obtained from volume distributions, which are more representative of the aerosol samples. From Figure 5.5, it is evident that the aerosol samples are partially frozen at 237.5 K.

The size of the aerosols produced by each generation method is an important point to consider, as the dependence of freezing on droplet volume and/or surface area (both functions of radius) is a focal point of this work. In particular, it is important to know the size of aerosols in the flow tube at the end of the conditioning sections, before they are exposed to the candidate freezing temperature. The manufacturer's specifications for the size output of the atomizer and nebulizer (Section 3.3) are not representative of the aerosol sizes following conditioning. In each case, the aerosols are generated at room

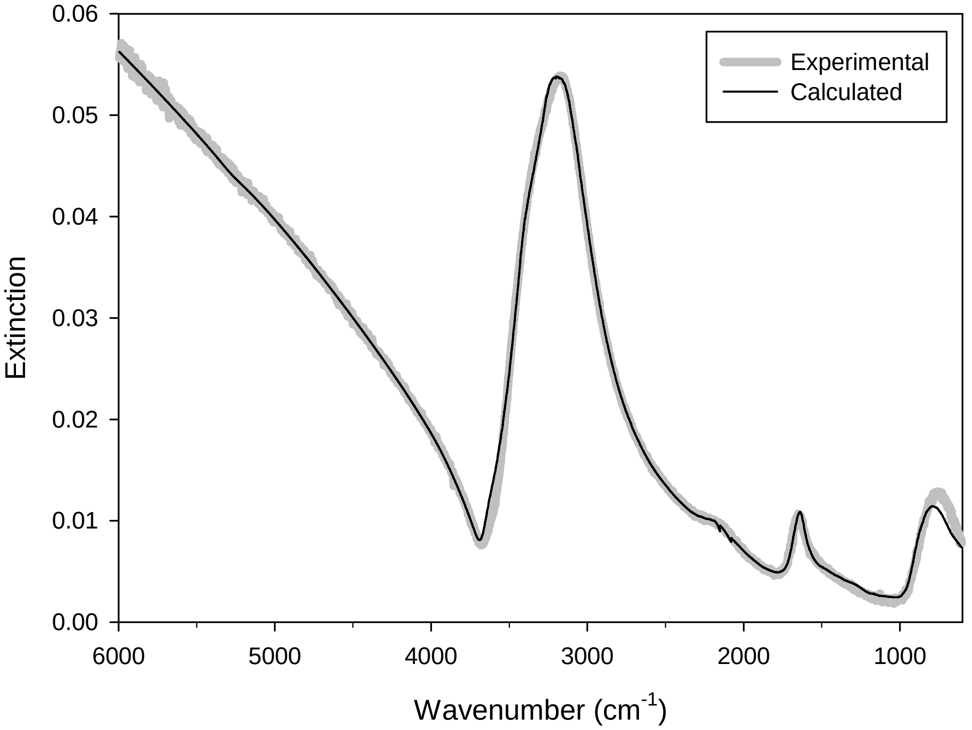

Figure 5.3: Measured extinction spectrum and calculated fit for a given freezing trial (aerosols produced by heterogeneous condensation, candidate freezing temperature of 237.5 K). Basis set spectra of water and ice were used to calculate the fit.

temperature and entrained in a flow of dry nitrogen carrier gas. The droplets equilibrate their vapour pressures with the surrounding gas; the smallest particles evaporate completely due to the Kelvin effect. As the aerosol is cooled to the conditioning temperature, the surrounding vapour condenses on the aerosols, as well as the tube wall and fins. In addition, vapour pressure gradients between particles with different sizes and/or temperatures can result in evaporation and growth due to the Kelvin effect and/or mass transfer, respectively. In the case of mass transfer, the aerosols nearest to the wall and fins will have the lowest temperatures (recall Figure 4.6), and hence, the lowest

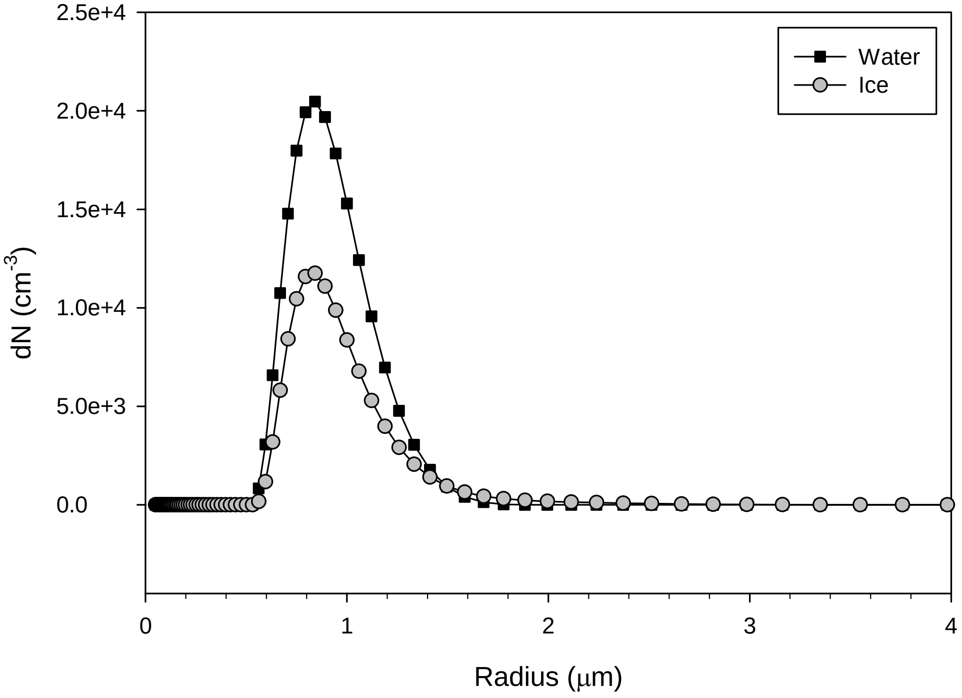

Figure 5.4: Number distributions of water and ice aerosols determined from the fit in Figure 5.3.

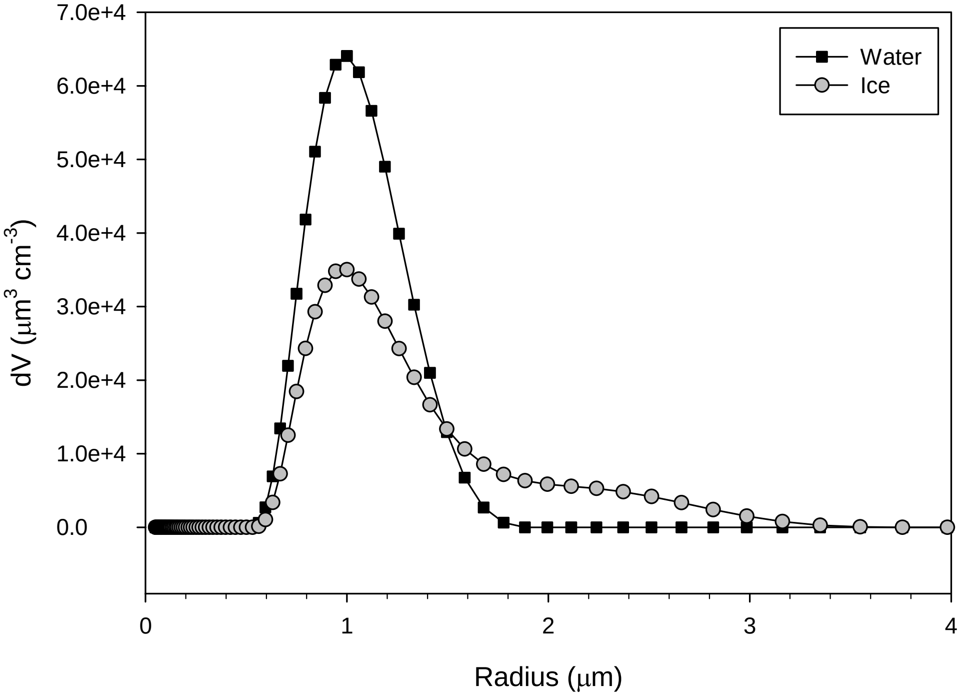

Figure 5.5: Volume distributions of water and ice aerosols determined from the fit in Figure 5.3.

saturation vapour pressures; these aerosols will grow at the expense of the warmer droplets in the quadrant interior, which will have higher saturation vapour pressures.

Contrary to the case for aerosols produced by atomization and nebulization, there was no predetermined size for the aerosols produced by heterogeneous condensation of vapour on dry NaCl. It was believed, however, that smaller aerosols could be generated by limiting the amount of vapour available for condensation. This was accomplished by controlling the humidified nitrogen flow (aerosol source flow) introduced to the dry particles in the flow tube.

To estimate the sizes of the conditioned aerosols from each generation method, freezing experiments were conducted with all four flow tube sections held at the conditioning temperature of 240 K. It was assumed that the vapour pressures of aerosol particles, and of condensed material on the tube wall and fins, had equilibrated in the first two sections, and that the aerosols did not experience appreciable changes in size beyond this point. Analysis of the resulting extinction spectra produced the volume distributions of supercooled water droplets for each generation method shown in Figure 5.6. The conditioned aerosols produced by heterogeneous condensation have radii between approximately 0.4 and 2 μm, with a maximum in the volume distribution at about 1 μm. Those produced by the constant output atomizer have radii between 0.6 and 5 μm, with a maximum at approximately 1.7 μm. Nebulization produces conditioned aerosols with radii between 1 and 7 μm, with a maximum at about 2.7 μm. Based on these sizes, the aerosols produced by condensation, atomization, and nebulization will henceforth be referred to as small, medium, and large particles, respectively.

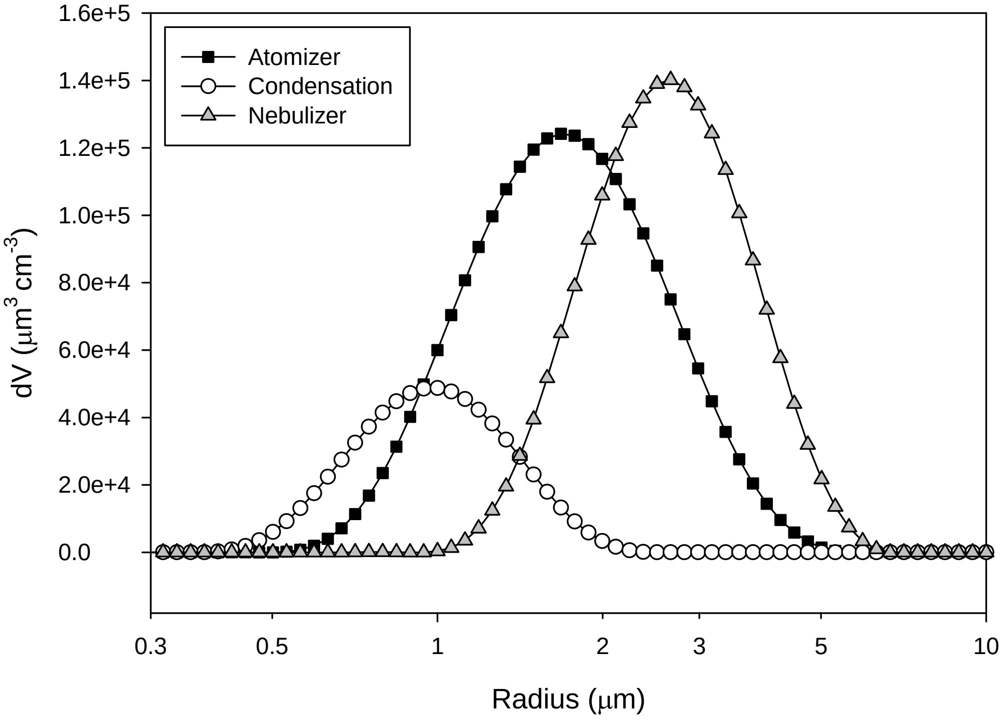

Figure 5.6: Volume distributions showing the sizes of water aerosols produced by each generation method following conditioning at 240 K. A logarithmic abscissa is used to facilitate comparison between the distributions.

As noted previously, aerosol phase is determined from the volume distributions output by the characterization procedure. The freezing of aerosols of each size is assessed based on the volume fraction of ice particles, or "fraction frozen," at each candidate freezing temperature. The resulting freezing curves (fraction frozen vs. temperature) ideally cover volume fractions of ice from 0 to 1, showing the full temperature evolution of the freezing process. The nucleation point is taken as the mid-point of each curve, corresponding with a fraction frozen of 0.5. The freezing curves for small, medium, and large particles determined in the present study are plotted in Figures 5.7 to 5.9, respectively. It is immediately apparent that these curves differ from the ideal case,

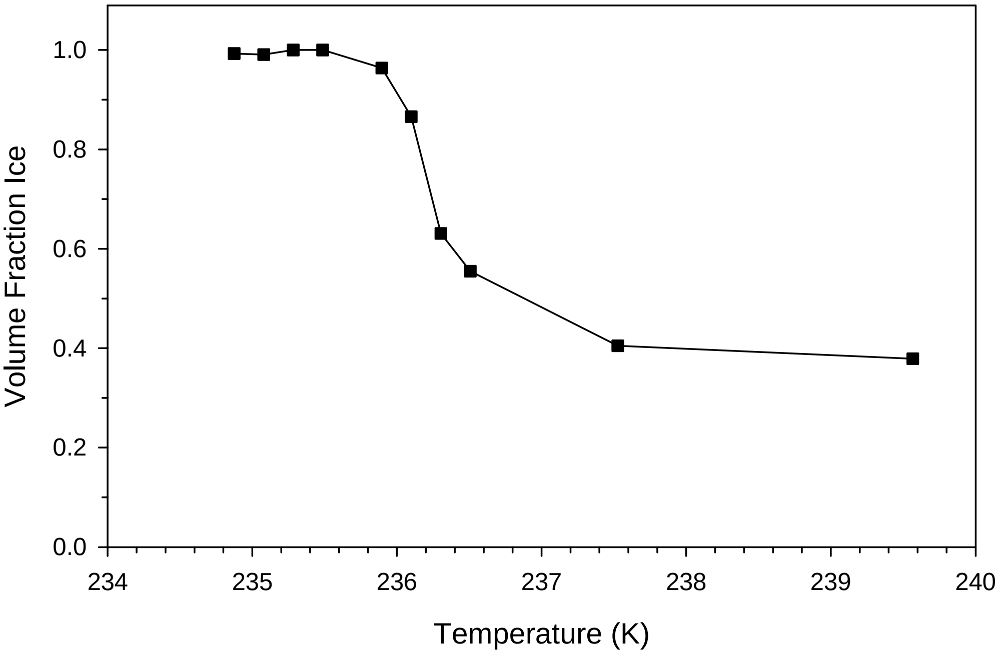

Figure 5.7: Freezing curve for small aerosols produced by heterogeneous condensation.

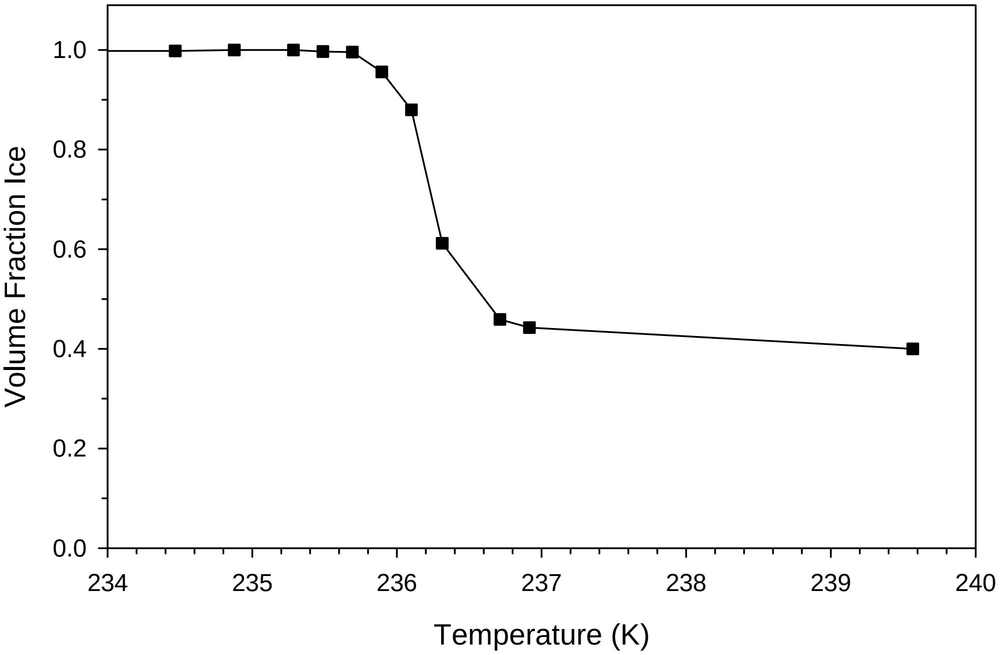

Figure 5.8: Freezing curve for medium aerosols produced by atomizer.

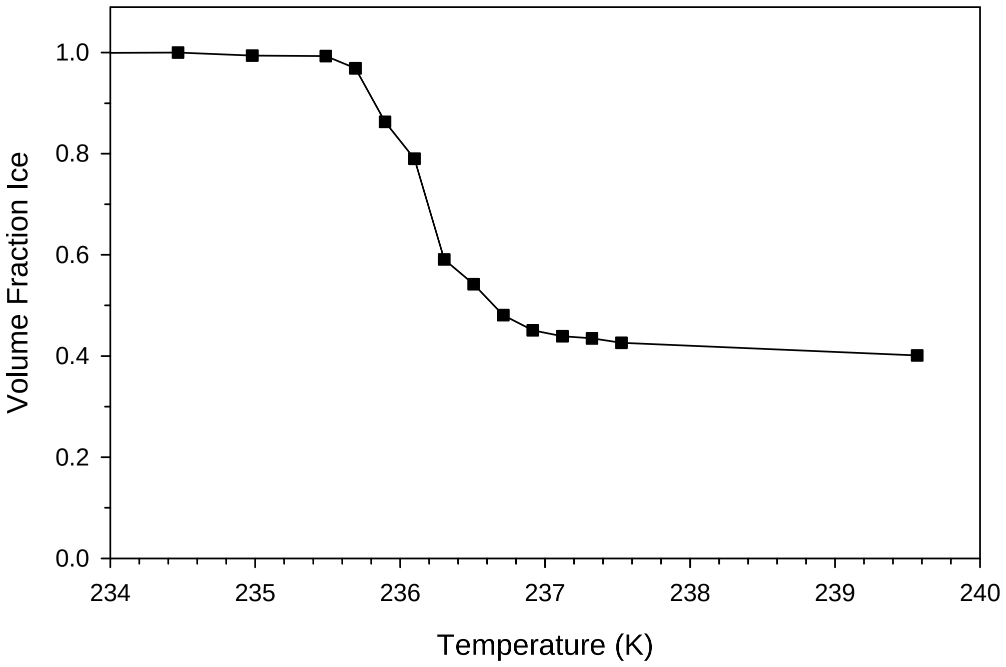

Figure 5.9: Freezing curve for large aerosols produced by nebulizer.

showing significant volume fractions of ice (0.4 and higher) at temperatures as warm as 239.6 K. This raised concerns regarding the potential for heterogeneous nucleation in our aerosol samples, which could account for warmer freezing temperatures.

Heterogeneous nucleation was first considered with respect to the small aerosols formed on NaCl nanoparticles. A comparison study was performed in which a dilute NaCl solution (10^{-4} M) was atomized directly, and the resulting freezing curve showed little variation from the results for medium aerosols in Figure 5.8. The results of this study, and the fact that the freezing behaviour of aerosols produced from NaCl nuclei was almost identical to that observed for pure water aerosols produced by the atomizer and nebulizer, suggested that the seemingly erroneous ice fractions in Figures 5.7 were not due to the presence of NaCl. Furthermore, it has been previously suggested that salt concentrations less than 10^{-3} M should have no influence on freezing.[27]

Contaminants in the Millipore-filtered water used to prepare the aerosols were also considered as potential heterogeneous nuclei; however, even if this material was present at parts-per-million levels, the concentration of potential nuclei would still be lower than in the aerosols produced from 10^{-4} M NaCl solution. Essentially ruling out heterogeneous nucleation, consideration turned to the aerosol characterization procedure from which the volume fractions of ice were determined.

5.3.3. Errors in Retrievals

In the discussion of the temperature-dependent changes in extinction spectra pertaining to Figure 5.1, it was noted that small changes in the absorption features of supercooled water are observed as the temperature is reduced to the nucleation point. These changes show similar trends to those associated with the freezing onset, and thus, the spectra are said to become more “ice-like” as the temperature is lowered. These changes are not sufficiently large to affect analysis by spectral variance, but can, however, interfere with analysis by the aerosol characterization procedure.

The basis set spectra of water used in the characterization procedure are calculated using complex refractive indices obtained at 300 K. These room temperature values are unable to reproduce the “ice-like” character in the extinction spectra of supercooled water, as illustrated in Figure 5.10 ($\chi^2 \sim 0.4$ for $\gamma = 0.02$). When the basis set spectra of ice are included, and both components are used to fit the same extinction spectrum, the fit is improved significantly (Figure 5.3). Thus, the ice spectra compensate

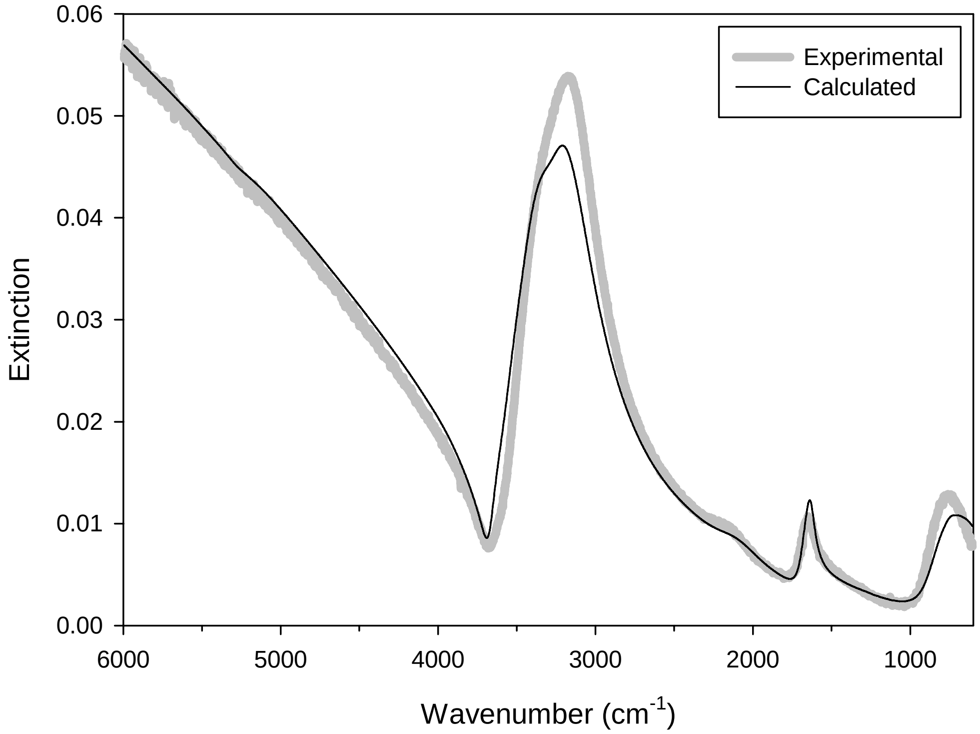

Figure 5.10: Measured extinction spectrum and calculated fit for the same freezing trial as in Figure 5.3 using only basis set spectra of water.

for the deficiency of the 300 K optical constants. While no ice is physically present in the supercooled water samples, the inclusion of the basis set spectra of ice to improve fit quality is interpreted as such by the characterization procedure. To attempt to circumvent this issue, and improve the freezing curves in Figures 5.7 to 5.9, temperature-dependent complex indices of refraction were determined for supercooled water over our range of experimental temperatures. This aspect of the study is detailed in Chapter 6.

CHAPTER SIX

SUPERCOOLED WATER OPTICAL CONSTANTS

6.1. Introduction

The temperature-dependent changes in the extinction spectra of supercooled water prior to the freezing onset are attributed to the formation of ordered domains, or "clusters" of water molecules. This ordering has been demonstrated previously in computer simulations,[92,93] wherein the extent to which molecules in supercooled water form tetrahedral arrangements with their nearest neighbours (as in the structure of ice; see Section 2.6) was probed as a function of temperature. It was found that the degree of ordering, or clustering, increased as the temperature was reduced, and was accompanied by changes from open or chain-like linear molecular structures to more compact structures, often with five- and six-member rings (see example in Figure 6.1). The results from computer simulations were corroborated by those from neutron diffraction[94] and IR spectroscopy[93] studies. The latter were conducted in our laboratory, and showed that as the temperature was reduced from 283 K, the librational mode of water around 700 cm^{-1} increased in intensity while shifting to higher wavenumbers. This is in agreement with our later results (see Figure 5.1 and related discussion), and is indicative of increased librational motion and intermolecular interactions, both of which are characteristic of increased ordering.

Cluster formation in supercooled water necessarily influences the complex indices of refraction. The presence of an "ice-like" component, which increases in extent as the temperature decreases, will cause the optical constants to diverge further and further from

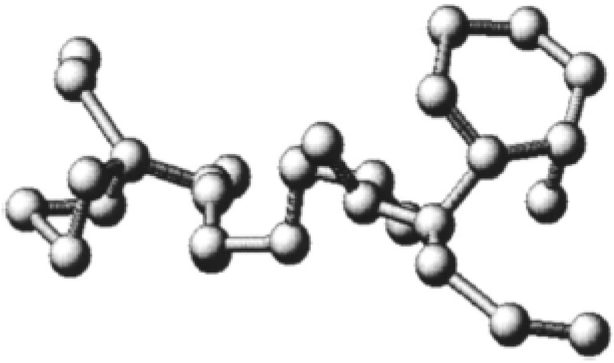

Figure 6.1: Cluster of 30 water molecules (balls represent O atoms) observed in computer simulations of supercooled water at 260 K.[93]

the pre-existing values obtained at 300 K. This is manifested as increasing ice fractions in our freezing curves prior to the nucleation point (Figures 5.7 to 5.9). To improve our freezing curves, and provide improved values for use in other laboratory and remote sensing studies, we obtained temperature-dependent complex indices of refraction for supercooled water. Values for ice at temperatures below the freezing point were also obtained. The experimental approach and resulting indices of refraction have been published previously.[79] The following chapter details these aspects of the study, and provides a comprehensive report of the freezing curves obtained using the new optical constants.

6.2. Experimental

The experimental approach was similar to that of the freezing experiments in Section 5.2. Water aerosols were generated using an atomizer, nebulizer, or heterogeneous condensation of vapour on dry NaCl nanoparticles. The total flow rate was maintained at 10 SLPM, with 0.5 – 3 SLPM aerosol or aerosol source flow and 7 – 9.5 SLPM carrier flow. The aerosols were conditioned in the top section of the cryogenic flow tube at 283 K, and cooled to between 278 and 230 K in the lower sections over the course of successive trials. Extinction spectra were recorded in the bottom section of the flow tube.

Complex refractive indices of supercooled water and ice were determined from extinction spectra of each component using the computational procedure described in Section 3.9. The "initial guess" values of $k(\tilde{\nu})$ used in the procedure were taken from the 300 K values of Bertie and Lan for water,[90] and the 240 K values of Warren for ice.[91] The anchor points, n_∞, for water were chosen at a wavelength of 0.5145 μm as follows: 1.3350, 1.3368, and 1.3371 for temperatures of 240, 263, and 278 K, respectively. The value for ice was taken from previous studies in which the optical constants of ice were determined from extinction spectra at 210 K (n_∞ = 1.232 at 2.5 μm).[80] The optical constants output by the procedure for spectra obtained using each generation method (each different size) were averaged at each experimental temperature.

6.3. Results and Discussion

6.3.1. Complex Indices of Refraction for Supercooled Water and Ice

The averaged indices of refraction obtained for supercooled water at 278, 263, and 240 K, and for ice at 235 K, are plotted in Figure 6.2. Temperature-dependent variations are evident in the supercooled water values, particularly in the regions between about 3000 – 3600 cm^{-1} and below about 1000 cm^{-1}. Both the real and imaginary

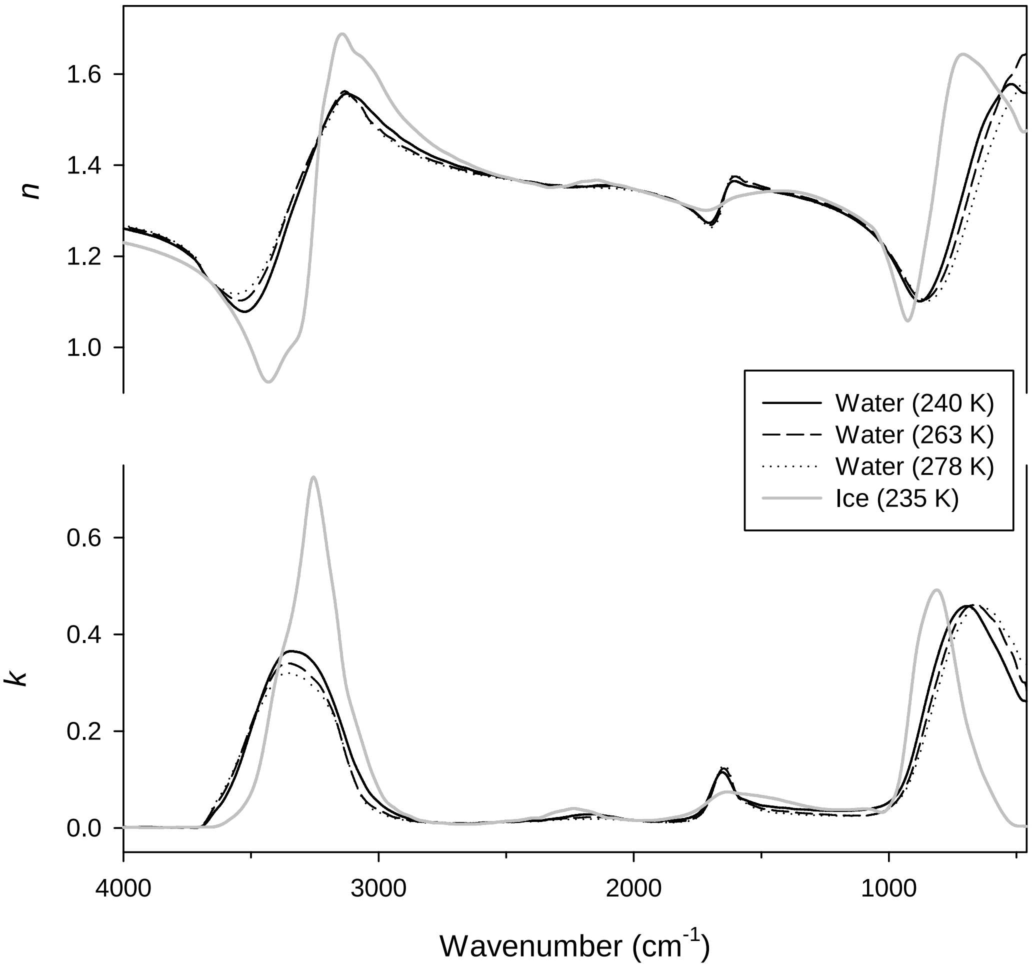

Figure 6.2: Averaged temperature-dependent refractive indices for supercooled water and ice. Values are truncated at 4000 cm^{-1} for clarity.

components become increasingly like the values for ice as the temperature is reduced, in accordance with the above discussion of cluster formation in supercooled water.

The supercooled water optical constants determined in the present study are compared against the values of Bertie and Lan and Warren in Figures 6.3 and 6.4. Recall that these literature values were used to generate the basis set spectra for water and ice producing the seemingly erroneous freezing curves in Figures 5.7 to 5.9. It is apparent that over both the 400 – 1000 cm^{-1} (Figure 6.3) and 1000 – 4000 cm^{-1} (Figure 6.4) spectral regions, the supercooled water refractive indices obtained in this study diverge further from the room temperature values of Bertie and Lan as the temperature is reduced, while becoming increasingly similar to the ice values of Warren. This demonstrates why the aerosol characterization procedure required increasing contributions from the basis set spectra calculated from the ice values at lower experimental temperatures.

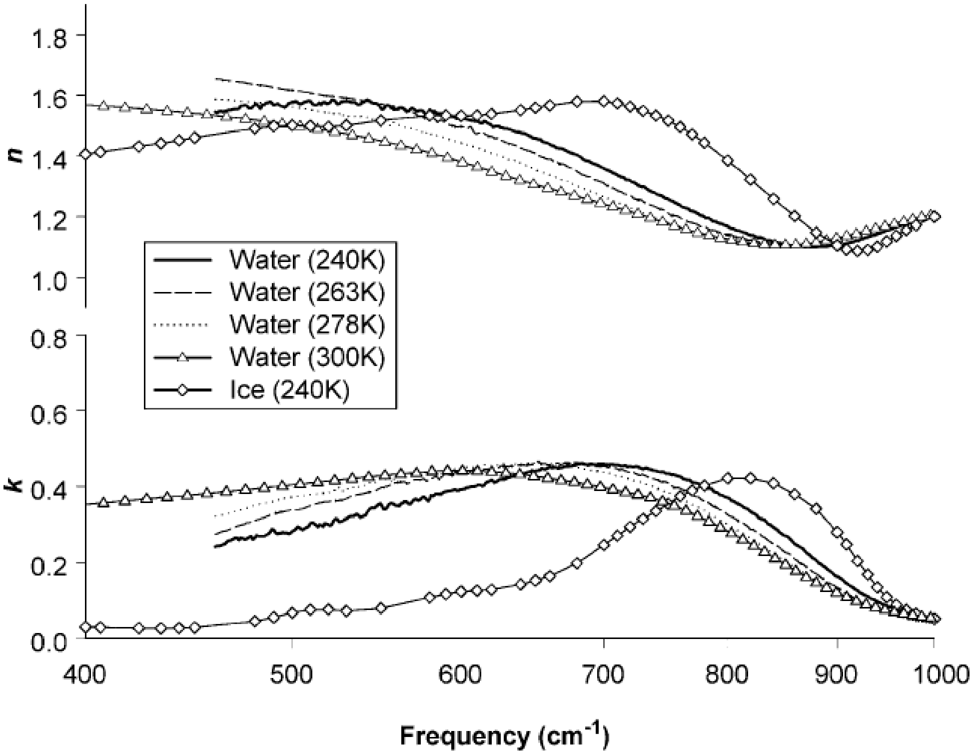

Figure 6.3: Comparison of temperature-dependent indices of refraction for supercooled water obtained in the present study with the values of Bertie and Lan (water at 300 K) and Warren (ice at 240 K) between 400 – 1000 cm^{-1}.[79]

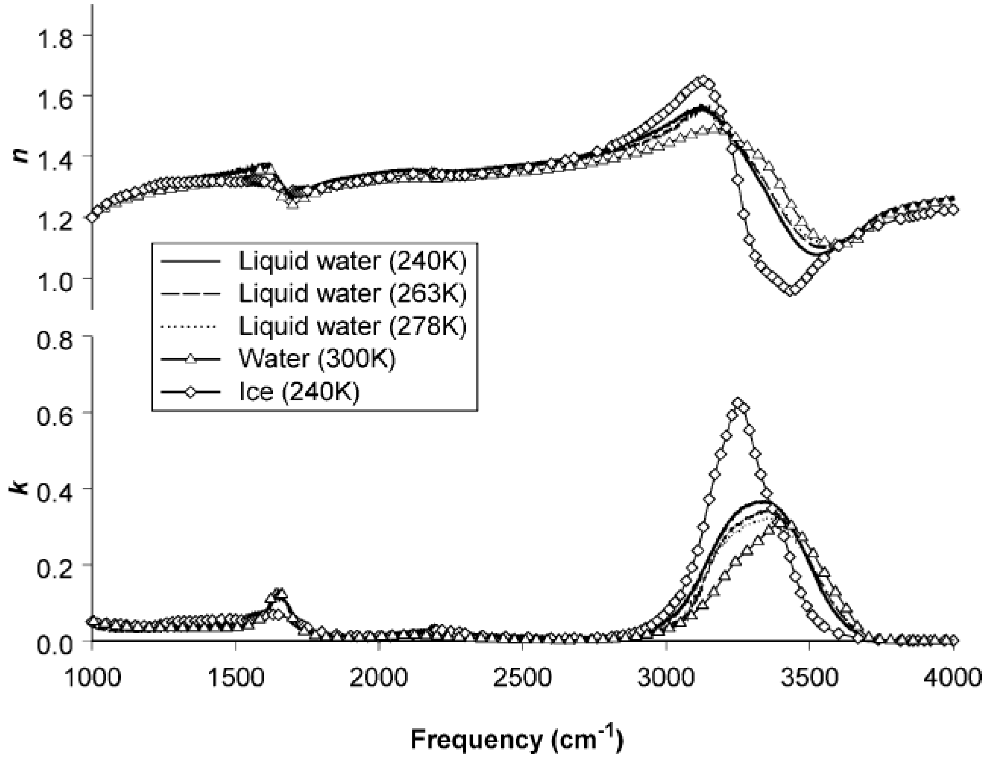

Figure 6.4: Same comparison as in Figure 6.3 extended over the wavenumber range between 1000 – 4000 cm^{-1}.[79]

The uncertainties in the averaged indices of refraction determined in the present study were estimated using the statistical approach of Dohm *et al.*.[81] In this approach, the standard deviation of *n* and *k* from the mean value at each wavenumber is taken as the uncertainty in each component. Uncertainties in both the real and imaginary components were determined to be largest (4%) between 3100 – 3400 cm^{-1}, and less than 2% over the remainder of the spectral range.

6.3.2. Improved Freezing Curves

The averaged indices of refraction determined for water at 240 K and ice at 235 K were used to generate new basis set spectra to be used in the aerosol characterization procedure. The experimental data producing the freezing curves in Figures 5.7 to 5.9 was then re-analyzed using these values. The agreement between calculated and experimental spectra improved, as shown in Figure 6.5 for the same experimental spectrum fit using the previous optical constants for water and ice in Figure 5.3 ($\chi^2 \sim 0.05$ for $\gamma = 0.02$). The resulting freezing curves for small, medium, and large particles are plotted alongside the previous results in Figures 6.6 to 6.8, respectively.

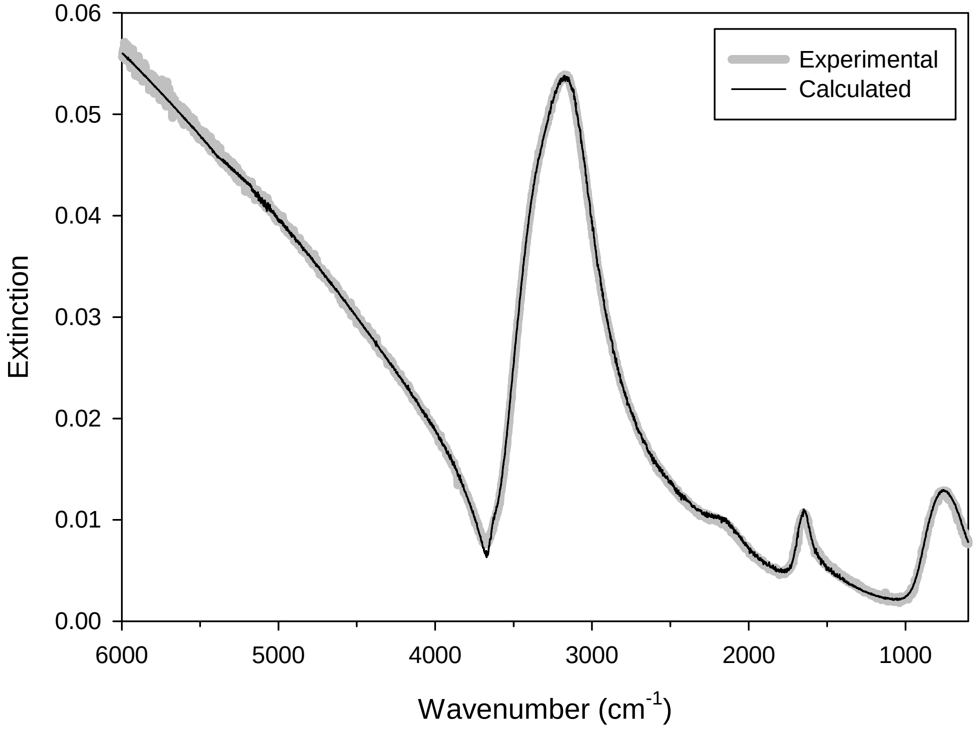

Figure 6.5: Measured extinction spectrum and calculated fit for a given freezing trial (aerosols produced by heterogeneous condensation, candidate freezing temperature of 237.5 K) using new basis set spectra for water (240 K) and ice (235 K). (Compare with fit using previous water and ice basis set spectra in Figure 5.3).

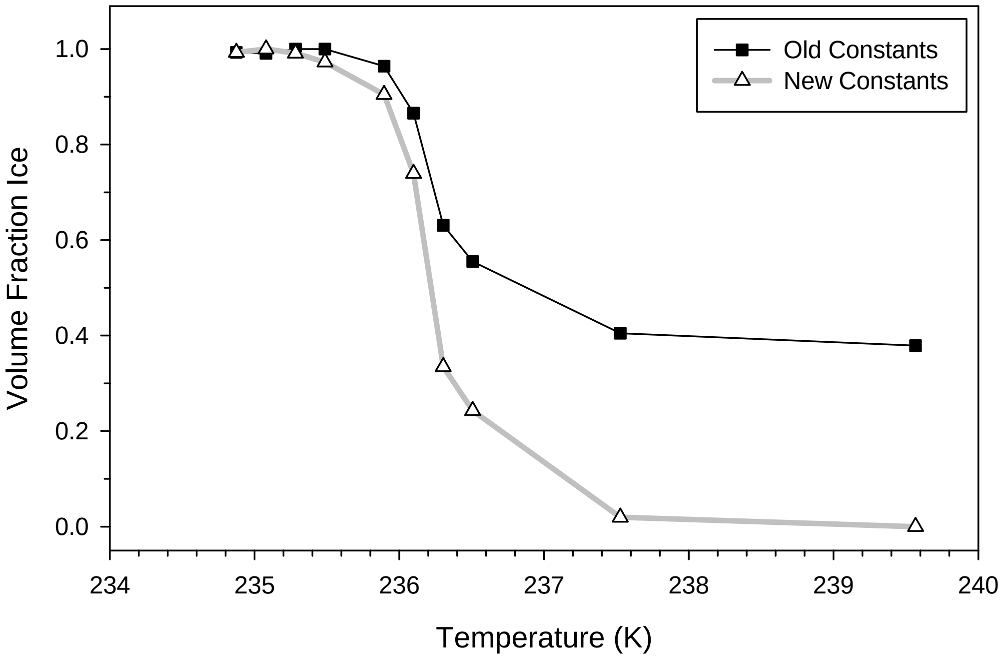

Figure 6.6: Freezing curves for small aerosols obtained using old and new optical constants for water and ice to generate basis set spectra.

Using the new optical constants, the freezing curves show minimal ice fractions at warmer temperatures, and cover the full extent of the freezing process (volume fractions of ice from 0 to 1) over the range of our experimental measurements. The temperature at the mid-point of each curve, corresponding with an ice fraction of 0.5, is taken as the homogeneous nucleation point. From visual inspection of Figures 6.6 to 6.8, it can be seen that the nucleation points for small, medium, and large aerosols are all at approximately 236.2 K. This is identical to the results from spectral variance detailed in Section 5.3.1, and corresponds well with the values from the literature (233 to 239 K). The excellent agreement between results obtained by different methods in the present

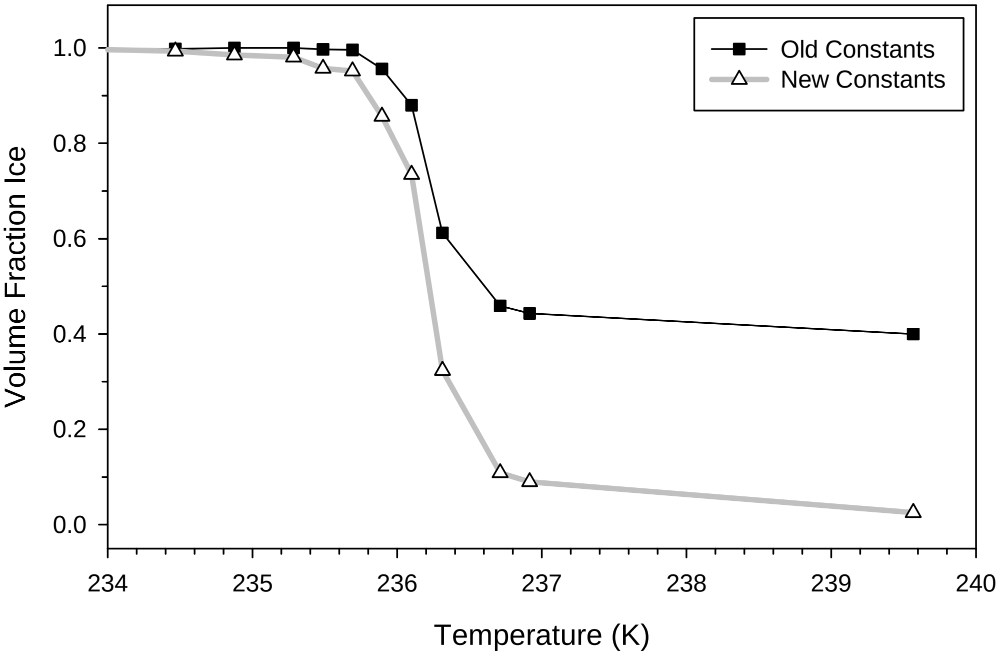

Figure 6.7: Freezing curves for medium aerosols obtained using old and new optical constants.

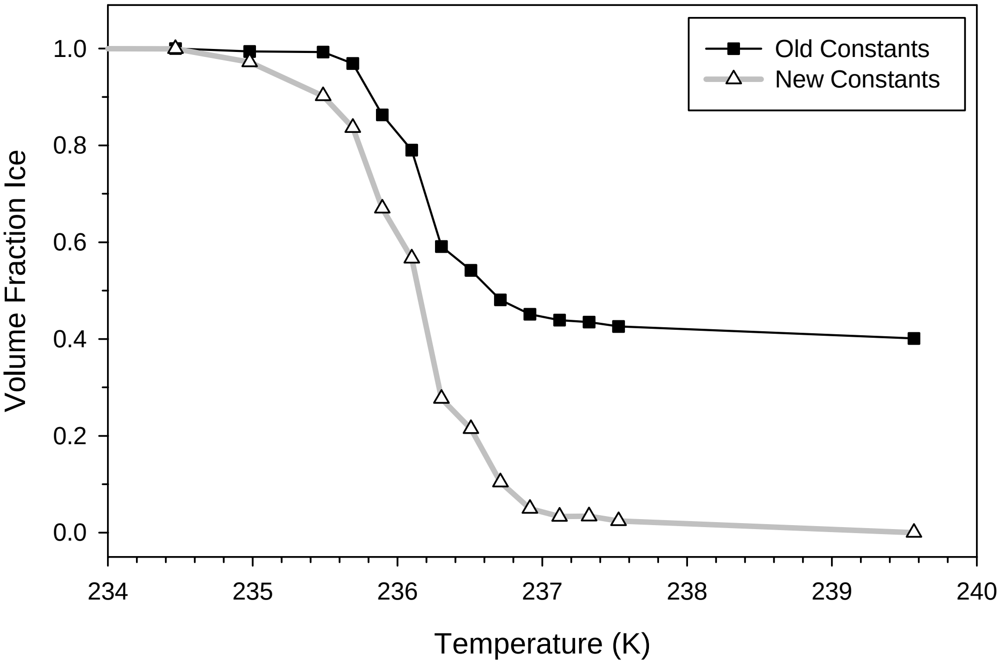

Figure 6.8: Freezing curves for large aerosols obtained using old and new optical constants.

study, and with independent studies in the literature, is taken as validation for our experimental approach. The subsequent treatment of freezing data to determine homogeneous nucleation rates is the subject of the following chapter.

The errors in the volume fractions of ice used to construct the freezing curves have been estimated from replicate trials performed at a given experimental temperature. Errors range from 2 to 3% at either end of the curves, where the samples are predominantly water or ice, to 10% near the mid-points (nucleation points), where the phase composition is most sensitive to small fluctuations in temperature. In the intermediate regions, errors rarely exceed 5%.

CHAPTER SEVEN

DETERMINATION OF NUCLEATION RATES

7.1. Introduction

Previous investigations of homogeneous nucleation rates have made use of diverse experimental methods and droplet sizes. Early work by Butorin and Skripov probed the freezing of 10 – 250 μm radius water droplets suspended in vacuum oil using calorimetric analysis.[31] Later studies by Taborek investigated emulsified droplets with radii between 3 and 300 μm using differential thermal analysis.[32] Both of these methods identified freezing events based on the corresponding release of latent heat. More recent work by DeMott and Rogers studied 5 μm radius droplets in a cloud expansion chamber,[27] as noted previously in Section 5.1. The number of ice particles formed, and hence the fraction frozen, was determined from extinction measurements of particles in a laser beam. The most recent studies have probed the freezing of individual droplets levitated in a cooled electrodynamic balance. Duft and Leisner[28] determined the freezing onset for levitated droplets with radii of 19 and 49 μm by analyzing the phase function of scattered light, while Krämer *et al.*[30] and Stöckel *et al.*[29] detected freezing in droplets with radii of 30 and 50 μm, respectively, based on particle interactions with linearly-polarized light.

In each of the above cases, homogeneous nucleation rates were determined from freezing data using a first-order kinetic approach of the general form:

$$\ln\left(\frac{N_j^0 - N_i}{N_j^0}\right) = -J_V(T)Vt \tag{7.1}$$

where N_j^0 is the initial number of liquid droplets, N_i is the number of frozen droplets, $J_V(T)$ is the temperature-dependent volume-based nucleation rate, V is droplet volume, and t is the exposure or residence time. Equation 7.1 can also be expressed as follows:

$$\frac{N_i}{N_j^0} = 1 - \exp\left[-J_V(T)Vt\right] \tag{7.2}$$

Hence, from experimental determination of the fraction frozen, N_i/N_j^0, for droplets with known volumes and residence times, one can determine the homogeneous nucleation rate for a given experimental temperature.

Considering homogeneous nucleation as a surface-based process, Equation 7.2 can be rewritten as:

$$\frac{N_i}{N_j^0} = 1 - \exp\left[-J_S(T)St\right] \tag{7.3}$$

where $J_S(T)$ is the temperature-dependent surface-based nucleation rate and S is the droplet surface area. Since the only difference between using Equations 7.2 or 7.3 to determine the nucleation rate is the functional dependence of radius (volume or surface), values of $J_V(T)$ can be converted into values of $J_S(T)$ using Equation 2.10.

Recalling Section 2.4, however, nucleation in aerosol samples can occur by both volume- and surface-based processes, with the relative contribution of each determined by droplet size and the nature of the interface between the droplets and surrounding media. Equations 7.2 and 7.3 can therefore be combined to give the following:

$$\frac{N_i}{N_j^0} = 1 - \exp\left[-\left\{J_V(T)V + J_S(T)S\right\}t\right] \tag{7.4}$$

where the term in curled brackets is the total nucleation rate, $J_T(T)$, from Equation 2.11.

The approach outlined above cannot be applied to the determination of nucleation rates in the present study, as the fraction of droplets frozen is determined not only by homogeneous nucleation, but by both homogeneous nucleation and mass transfer. Previous studies of homogeneous ice nucleation in laminar aerosol flow tubes have shown that at temperatures near the nucleation point, only a small fraction of the aerosols freeze (1 in 10^4 to 10^6), followed by significant vapour-phase exchange from the remaining liquid droplets to the nascent ice particles.[17] The confounding role of mass transfer in nucleation rate determination is limited to studies of droplets suspended in air in flow tubes and cloud chambers. No vapour-phase exchange will occur for droplets suspended in emulsions, or for single droplets levitated in an electrodynamic balance, though evaporative losses are a concern in the latter.[29]

To separate the contributions from homogenous nucleation and mass transfer in experimental measurements of aerosols in laminar flow tubes, microphysical models have been employed. Hung and Martin[17,89,95] developed an inversion model in which the volume-based nucleation rate was treated as an adjustable parameter, and homogeneous nucleation and mass transfer were considered as sequential processes. The nucleation rate, $J(T)$, was iteratively varied to produce the best agreement between the volume fraction of ice calculated by the model, and that determined by FTIR observation, for a given freezing temperature.

A similar model has been developed in the present study to determine both volume- and surface-based nucleation rates from experimental freezing data. The following chapter details the model and underlying microphysics, and compares the resulting nucleation rates with literature values. The preponderance of surface and/or volume nucleation in our flow tube studies is also discussed.

7.2. Model Description

Implemented in Matlab (The Mathworks, Inc.), the model developed in our laboratory inverts experimentally measured volume distributions of supercooled water and ice aerosols to determine temperature-dependent homogeneous nucleation rates. The model considers the volume distributions before and after the freezing event, which are referred to as the initial and final distributions, respectively. The initial supercooled water distribution is taken as one of the small, medium, or large distributions in Figure 5.6, obtained after conditioning at 240 K. The final supercooled water and/or ice distributions are taken from experiments conducted with the bottom two tube sections at a given candidate freezing temperature.

The model consists of microphysics and minimization components (but will henceforth be referred to simply as the microphysics model), and is depicted schematically in Figure 7.1. The microphysics component comprises a series of differential equations describing homogeneous ice nucleation and diffusion-limited exchange between aerosol particles and vapour-phase water. The latter includes particle growth/evaporation due to both mass transfer between frozen and liquid droplets and the Kelvin effect. Nucleation and vapour-phase exchange processes are considered simultaneously, unlike the sequential approach of Hung and Martin.[17,89,95] The microphysics component takes the initial supercooled water distribution and solves the differential equations based on the flow velocity, axial temperature profile in the flow

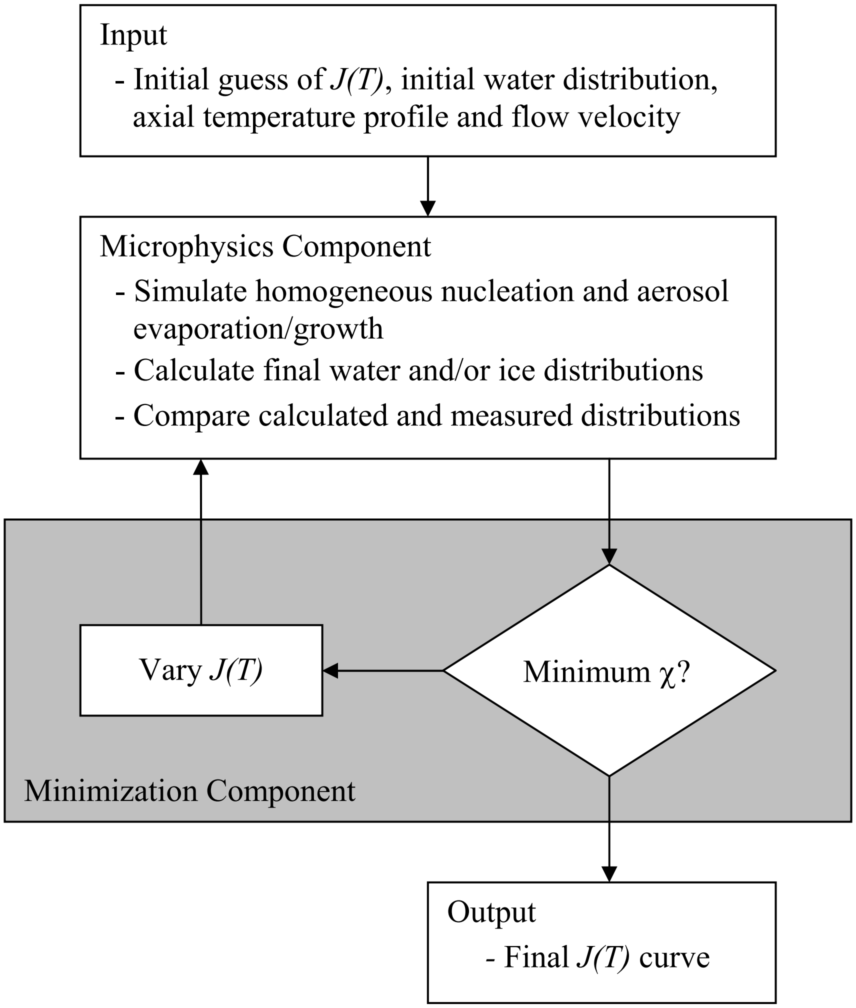

Figure 7.1: Schematic representation of aerosol microphysics model.

tube, and nucleation rate function *J(T)*. One can assume a volume- and/or surface-based process by employing $J_V(T)$ and/or $J_S(T)$. Calculated volume distributions of supercooled water and/or ice are output. The normalized sum of squares of differences, χ, between the calculated and experimentally-measured (final) supercooled water and ice distributions serves as the basis for the minimization component. This component iteratively varies the function *J(T)* over successive model runs to minimize the value of χ. The microphysics and minimization components are discussed in greater detail in the following sections. The Matlab model code is provided in Appendix B.

7.2.1. Microphysics Component

The volume distributions output by the aerosol characterization procedure give the volume of particles in each of the 96 bins corresponding with the radii in the spectral basis set (see Sections 3.8 and 5.3.2). The bins have zero width, and are referred to as nodes; particles can reside only at the nodes. The indices i and j are used to denote ice and water nodes, respectively.

As described above, the model calculates the time evolution of the initial supercooled water distribution due to homogeneous nucleation and diffusion-limited exchange. The rate of increase in the number of ice particles due to homogeneous nucleation is given by the differential forms of Equations 7.2 and 7.3, which are expressed as follows:

$$dN_i / dt = N_j \, J_V(T) \, V_j \tag{7.5}$$

$$dN_i / dt = N_j \, J_S(T) \, S_j \tag{7.6}$$

where N_i is the number of ice particles in node i, N_j is the number of liquid water droplets in node j, and $V_j = (4/3)\pi r_j^3$ and $S_j = 4\pi r_j^2$ are the volume and surface area of a droplet of radius r_j, respectively. Regardless of the assumed surface and/or volume dependence, the decrease in the number of water droplets resulting from homogeneous nucleation is given as follows for each node:

$$dN_j / dt = -dN_i / dt \tag{7.7}$$

Equations 7.5 to 7.7 are based on the assumptions that nucleation events in droplets are independent, that ice formation is the result of only one nucleation event per droplet, and that once nucleated, a droplet is immediately converted into ice.

The temperature dependence of the volume- and surface-based nucleation rates is taken into account by using the following functional expressions:[34]

$$J_V(T) = N_L \frac{k_B T}{h} \exp\left(-\frac{\Delta G^V}{RT} \right) \tag{7.8}$$

$$J_S(T) = N_S \frac{k_B T}{h} \exp\left(-\frac{\Delta G^S}{RT} \right) \tag{7.9}$$

In Equations 7.8 and 7.9: $N_L = 3.35 \times 10^{22}$ cm^{-3} and $N_S = 1.04 \times 10^{15}$ cm^{-2} are the bulk and surface number densities of water molecules in liquid water, respectively; k_B is the Boltzmann constant; h is Planck's constant; and R is the ideal gas constant. The terms ΔG^V and ΔG^S represent the free energy of nucleus formation in the bulk volume and on the surface of droplets, respectively. The temperature dependence imparted by the above equations is important for calculating the number of ice particles formed as the initial supercooled water distribution travels along the axial temperature profile in the flow tube. Furthermore, it is the temperature-dependent values, $J_V(T)$ and/or $J_S(T)$, that are the desired model output.

The free energies in Equations 7.7 and 7.8 can be considered in terms of the activation enthalpy, ΔH_{act}, and entropy, ΔS_{act}, as follows:

$$\Delta G^V = \Delta H_{act}^V - T\Delta S_{act}^V \tag{7.10}$$

$$\Delta G^S = \Delta H_{act}^S - T\Delta S_{act}^S \tag{7.11}$$

The activation enthalpy and entropy are not assigned any physical meaning or significance, and are treated solely as adjustable parameters in the minimization component (Section 7.2.2).

Diffusion-limited exchange processes result from differences between the saturation vapour pressures above particles and the partial pressure of water vapour in the surrounding gas. These processes include the evaporation and growth of liquid particles due to the Kelvin effect, and the growth of ice particles at the expense of the remaining liquid droplets by mass transfer. The rate of radius change for water droplets and ice particles by the combination of these processes is determined as follows:[5]

$$\frac{dr_j}{dt} = \frac{D^*_{v,j} M_w}{R\rho_{water}} \frac{1}{r_j} \left(\frac{p_\infty}{T_\infty} - \frac{p_j}{T_j} \right) \tag{7.12}$$

$$\frac{dr_i}{dt} = \frac{D^*_{v,i} M_w}{R\rho_{ice}} \frac{1}{r_i} \left(\frac{p_\infty}{T_\infty} - \frac{p_{ice}}{T_i} \right) \tag{7.13}$$

where r_j is the radius of liquid node j; r_i is the radius of ice node i; $D^*_{v,j}$ and $D^*_{v,i}$ are the gas-phase diffusion coefficients for water and ice, corrected for non-continuum effects;[12] M_w is the molecular weight of water; ρ_{water} is the density of supercooled water; ρ_{ice} is the density of ice; p_∞ is the far-field water partial pressure; p_j is the saturation vapour pressure above droplets in liquid node j, which is corrected for the Kelvin effect; p_{ice} is the saturation vapour pressure of ice; T_∞ is the ambient gas temperature; T_i and T_j are the surface temperatures of ice particles and water droplets, respectively. It is assumed that $T_\infty = T_i = T_j$, as the gain/release of heat by particles by condensation/evaporation will not change the particle surface temperatures by more than 0.1 K.[17] The determination of corrected values of $D^*_{v,i/j}$ and p_j, and the calculation of p_∞, are discussed further below.

Diffusion-controlled exchange is generally predicated on the assumption that the water vapour density is continuous above the surface of droplets.[12] This assumption does not hold for small particles whose radii approach the mean free path, λ, of vapour molecules. Following the approach of Fuchs, the gas-phase diffusion coefficient, D_v, can be corrected for small particles by considering the continuum extends to a distance, Δv, above the particle surface. The corrected form, $D^*_{v,i/j}$, is calculated using the following expression:

$$D^*_{v,i/j} = \frac{D_v}{\left[\dfrac{r_{i/j}}{r_{i/j} + \Delta v} + \dfrac{D_v}{r_{i/j}\,\alpha_{i/j}}\left(\dfrac{2\pi M_w}{RT_{i/j}}\right)^{1/2}\right]} \tag{7.14}$$

where α is the mass accommodation coefficient. Values of $\alpha_j = 0.5$ and $\alpha_i = 1$ were used in the present studies for water and ice, respectively (the water value was extrapolated from the temperature-dependent data in Ref 96). The distance Δv was taken as 1.3 λ.[12]

Special consideration must also be paid to small particles when calculating the saturation vapour pressures above the surfaces of liquid droplets. As noted previously, the vapour pressure above curved droplet surfaces is greater than that above flat surfaces, according to the Kelvin effect. The corresponding Kelvin equation is given as follows:[12]

$$\frac{p_j}{p_{sat}} = \exp\left(\frac{2M_w\sigma}{RT_j\rho_{water}r_j}\right) \tag{7.15}$$

In Equation 7.15, p_{sat} is the saturation vapour pressure over a flat water surface, and σ is the surface tension of water. The difference between p_j and p_{sat} becomes increasingly significant as the radius of droplets is decreased, and is particularly important for droplets with radii in the sub-micrometre range.

The far-field water partial pressure, p_∞, is calculated from the total concentration of gaseous water, N^V, using the ideal gas law:

$$p_\infty = \frac{N^V}{N_A} R T_\infty \tag{7.16}$$

where N_A is Avogadro's constant. The value of N^V is determined by assuming that the concentration of gaseous water is in a steady-state with respect to condensation and evaporation to and from liquid droplets and ice particles, and is subject to losses to the ice-coated tube walls and fins.

$$\frac{dN^V}{dt} = \sum_{j=1..96} \frac{dN_j^V}{dt} + \sum_{i=1..96} \frac{dN_i^V}{dt} - k\left(N^V - N_{ice}\right) \tag{7.17}$$

The first two terms in Equation 7.17 represent the contributions from the liquid droplets and ice particles, where:

$$\frac{dN_j^V}{dt} = \frac{dm_j}{dt} \frac{1}{v_{water} \rho_{water}} \tag{7.18}$$

$$\frac{dN_i^V}{dt} = \frac{dm_i}{dt} \frac{1}{v_{ice} \rho_{ice}} \tag{7.19}$$

$$\frac{dm_j}{dt} = 4\pi r_j^2 \rho_{water} N_j \frac{dr_j}{dt} \tag{7.20}$$

$$\frac{dm_i}{dt} = 4\pi r_i^2 \rho_{ice} N_i \frac{dr_i}{dt} \tag{7.21}$$

In the above equations, m_j is the mass concentration of liquid droplets in node j, m_i is the mass concentration of ice particles in node i, and v_{ice} and v_{water} are the molecular volumes of liquid water and ice, respectively. The third term in Equation 7.17 represents the loss of gaseous water to the ice-coated tube walls and fins, where N_{ice} is the concentration of gaseous water from the saturation vapour pressure of ice, and k is the first-order rate constant for radial diffusion to the walls in a laminar flow:[97,98]

$$k = \frac{\mu D_v}{r_t^{\,2}} \tag{7.22}$$

In Equation 7.22, $\mu = 3.66$ is the Sherwood number for a cylindrical pipe and r_t is the tube radius. In the present studies, $k = 0.138\ \mathrm{s}^{-1}$.[99]

From Equations 7.12 and 7.13, the changes in size of liquid water droplets and ice particles are determined by the difference between the far-field vapour pressure and the saturation vapour pressures of particles. Thus, a particle may be added to a node by condensation growth of smaller particles, or evaporative losses from larger particles. Likewise, a particle may be removed from a node by its evaporation to a smaller size, or its growth to a larger size by condensation. This vapour-phase exchange between nodes has been implemented in the model using the recently-reported approach of Prakash *et al.*.[100] The change in the number of liquid droplets in each node j is considered in terms of four separate vapour pressure scenarios, as given by the individual terms in Equation 7.23:

$$\frac{dN_j}{dt} = \begin{cases} -\dfrac{v_{water}}{v_j - v_{j-1}} \dfrac{dN_{j-1}^V}{dt} & if\,(p_\infty > p_{j-1}) \\ \dfrac{v_{water}}{v_{j+1} - v_j} \dfrac{dN_{j+1}^V}{dt} & if\,(p_\infty < p_{j+1}) \\ -\dfrac{v_{water}}{v_{j+1} - v_j} \dfrac{dN_j^V}{dt} & if\,(p_\infty > p_j) \\ \dfrac{v_{water}}{v_j - v_{j-1}} \dfrac{dN_j^V}{dt} & if\,(p_\infty < p_j) \end{cases} \tag{7.23}$$

where v_j is the volume of a particle in node j, and v_{j-1} and v_{j+1} are the volumes of particles in adjacent nodes. The first two terms in Equation 7.23 will increase the number density of particles in node j, while the last two terms will decrease the number density. An equivalent set of equations is used to describe the change in the number of ice particles in each node i due to vapour-phase exchange, where p_j is replaced by p_{ice}.

The inputs for the microphysics component are the initial volume distribution of supercooled droplets, the time evolution of temperature (determined from the flow velocity and axial temperature profile), and values of ΔH_{act} and ΔS_{act} for the calculation of the nucleation rate, $J(T)$. Recalling Section 4.7, mass-averaged axial temperature profiles obtained from CFD simulations are used in the model. By evaluating the differential and algebraic expressions in Equations 7.5 to 7.23, the model calculates the time evolution of the far-field partial pressure, supercooled water and ice distributions, and the volume fraction of ice, as shown in Figures 7.2 and 7.3.

The initial volume distribution of supercooled water droplets in Figure 7.3 (solid black curve) has a maximum at a radius of ~ 1.7 μm (medium particles). As the temperature is reduced along the profile in Figure 7.2, the volume density of water particles first increases slightly due to condensation growth upon cooling, and then decreases as soon as the first particles are frozen, at which point the volume density of ice particles increases. The ice particles are larger, with a maximum at a radius of ~ 3 μm, due to mass transfer following the freezing event. The final distribution is composed entirely of ice particles (grey triangles) in this case, though supercooled water can potentially persist for trials using different temperature profiles and/or initial sizes. The

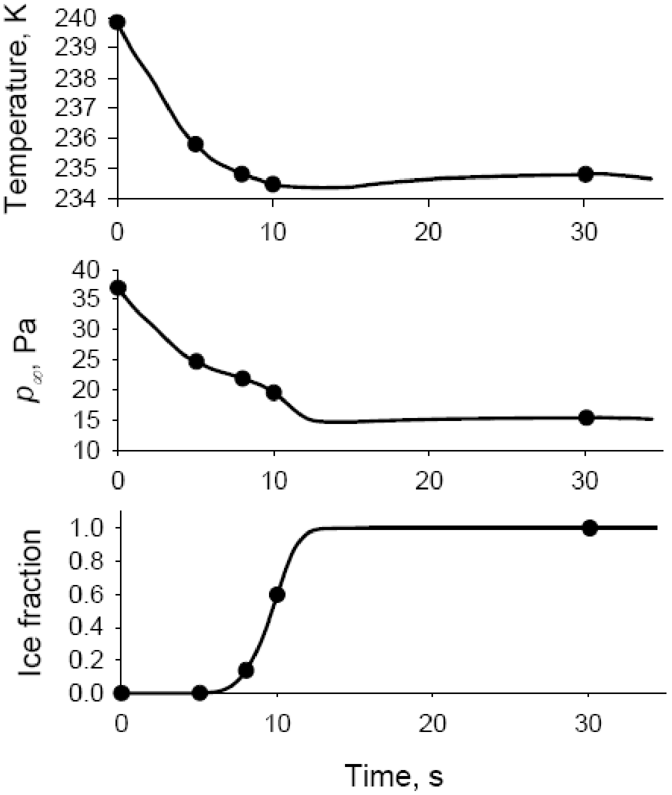

Figure 7.2: Time evolution of temperature, far-field partial pressure of water, and volume fraction of ice calculated by the model for a given cooling scenario (candidate freezing temperature of 235 K, mean flow velocity of 3 cm s^{-1}). The solid circles indicate the times for which the volume distributions of supercooled water and ice are shown in Figure 7.3.[101]

calculated distributions of supercooled water and/or ice are output to the minimization component, described in the following section.

7.2.2. Minimization Component

The minimization component iteratively varies the values of ΔH_{act} and ΔS_{act} to minimize the normalized sum of squares of differences, χ, between the volume distributions of supercooled water and ice calculated by the model and those measured in

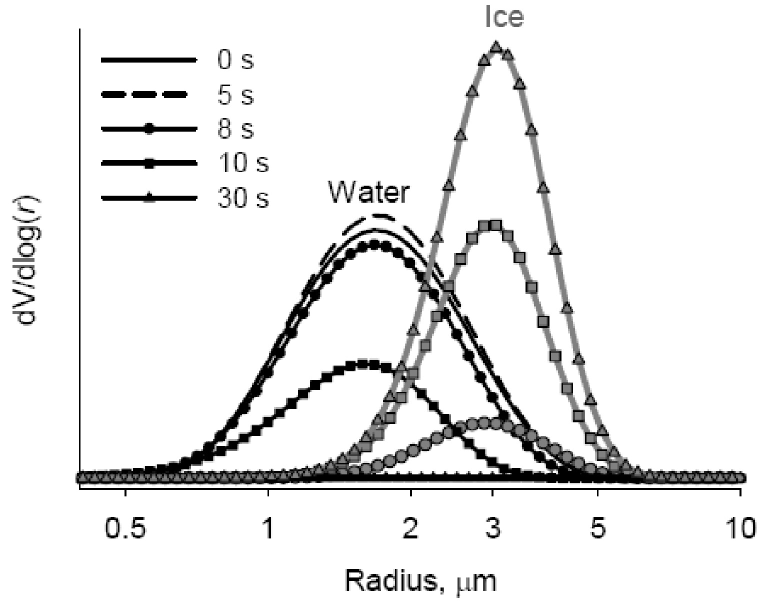

Figure 7.3: Time evolution of supercooled water and ice distributions corresponding with the changes shown in Figure 7.2.[101]

freezing experiments (final distributions). For a set of n experiments, this minimization criterion takes the form:

$$\chi = \sum_{k=1..n} \left(\frac{\sum_{i=1..96} (V_{i,k}^{\exp} - V_{i,k}^{calc})^2}{\sum_{i=1..96} V_{i,k}^{\exp}} \right) + \sum_{k=1..n} \left(\frac{\sum_{j=1..96} (V_{j,k}^{\exp} - V_{j,k}^{calc})^2}{\sum_{j=1..96} V_{j,k}^{\exp}} \right) \tag{7.24}$$

where V_i is the volume density of ice particles in node i, and V_j is the volume density of liquid droplets in node j. The n experiments refer to freezing experiments conducted using different candidate freezing temperatures, and hence different temperature profiles, and/or different initial size distributions of supercooled water (small, medium, or large particles). An example of calculated fits to experimentally measured volume distributions producing a minimum value of χ is given in Figure 7.4.

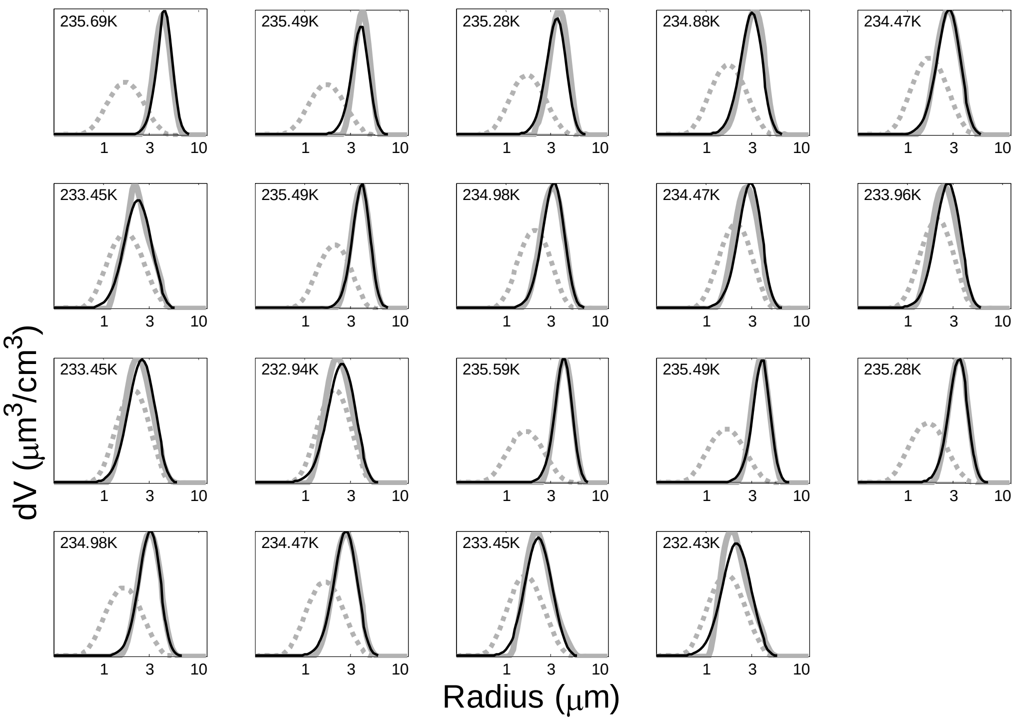

Figure 7.4: Initial supercooled water (dashed grey curves), experimentally measured ice (solid grey curves), and calculated ice (solid black curves) distributions for n = 19 freezing experiments conducted using medium particles (temperatures given in inset of each plot). Distributions are plotted on a logarithmic radius scale.

Assuming volume-based nucleation, the minimization component finds the values of ΔH_{act}^{V} and ΔS_{act}^{V}, defining $J_V(T)$, that give the minimum value of χ. Similarly, if surface-based nucleation is assumed, the component finds the values of ΔH_{act}^{S} and ΔS_{act}^{S}, defining $J_S(T)$, that minimize χ. If both volume- and surface-based processes are assumed, all four activation parameters are varied to minimize χ, and values of $J_V(T)$ and $J_S(T)$ are obtained. These dual-process runs are important for assessing the relative contributions of volume and surface nucleation for a given set of experiments.

7.3. Results and Discussion

To determine values of $J_V(T)$ and $J_S(T)$ that apply to all of our particle sizes, model runs were performed using distributions from a collection of 34 freezing experiments on small, medium, and large particles. Subsets of 19 distributions from experiments on medium particles (shown in Figure 7.4), six distributions from small particles, and nine distributions from large particles were used. Separate runs assuming only volume nucleation, only surface nucleation, and both volume and surface nucleation were performed. The resulting values of χ were 978.8, 671.5, and 660.1, respectively. Thus, the poorest reproductions of the 34 measured distributions were achieved assuming volume-based nucleation, and the best reproductions were achieved using both volume- and surface-based nucleation. The latter result can likely be attributed to the additional degree of freedom imparted by fitting with both processes. It is interesting to note, however, the similarity of the χ values for surface-only and volume and surface runs. The potential ramifications of this similarity will be considered further in the following discussion.

The values of $J_V(T)$ determined from the volume-only and volume and surface runs are plotted with results from the literature in Figure 7.5. It should be noted that the model results are $J_V(T)$ curves calculated from ΔH_{act}^{V} and ΔS_{act}^{V} over the range of experimental temperatures, and not individual points. Based on model runs performed on replicate experimental distributions at a given temperature, errors in our $J_V(T)$ values are estimated to be within a factor of three to five (the upper bound is shown as the error bar in Figure 7.5). Assuming only volume-based nucleation, the model results agree well with the literature values. When surface-based nucleation is included in the model runs,

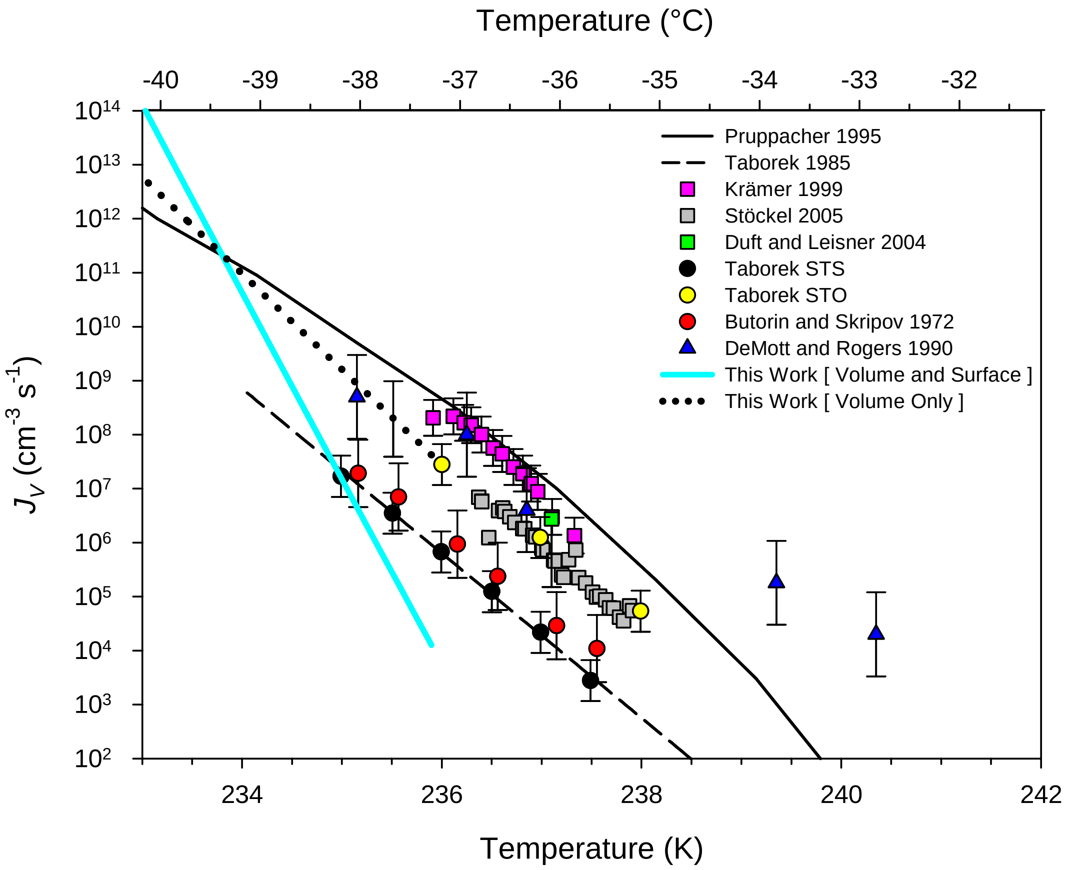

Figure 7.5: Comparison of model results for $J_V(T)$ assuming volume-only or both volume and surface nucleation with literature values. Squares, circles, and triangles denote studies performed using suspensions/emulsions, levitated droplets, and cloud chambers, respectively. The different surfactants used by Taborek are designated as STS for sorbitan tristearate and STO for sorbitan trioleate.

however, the $J_V(T)$ curve shifts away from the volume-only and literature values, with a steeper dependence on temperature.

The cause for this shift is evident upon inspection of the model results for $J_S(T)$, which are plotted alongside the literature values in Figure 7.6. In this case, the model results are $J_S(T)$ curves calculated from ΔH_{act}^{S} and ΔS_{act}^{S} over the range of experimental temperatures. Again, the errors in our model results are estimated to be, at most, within a

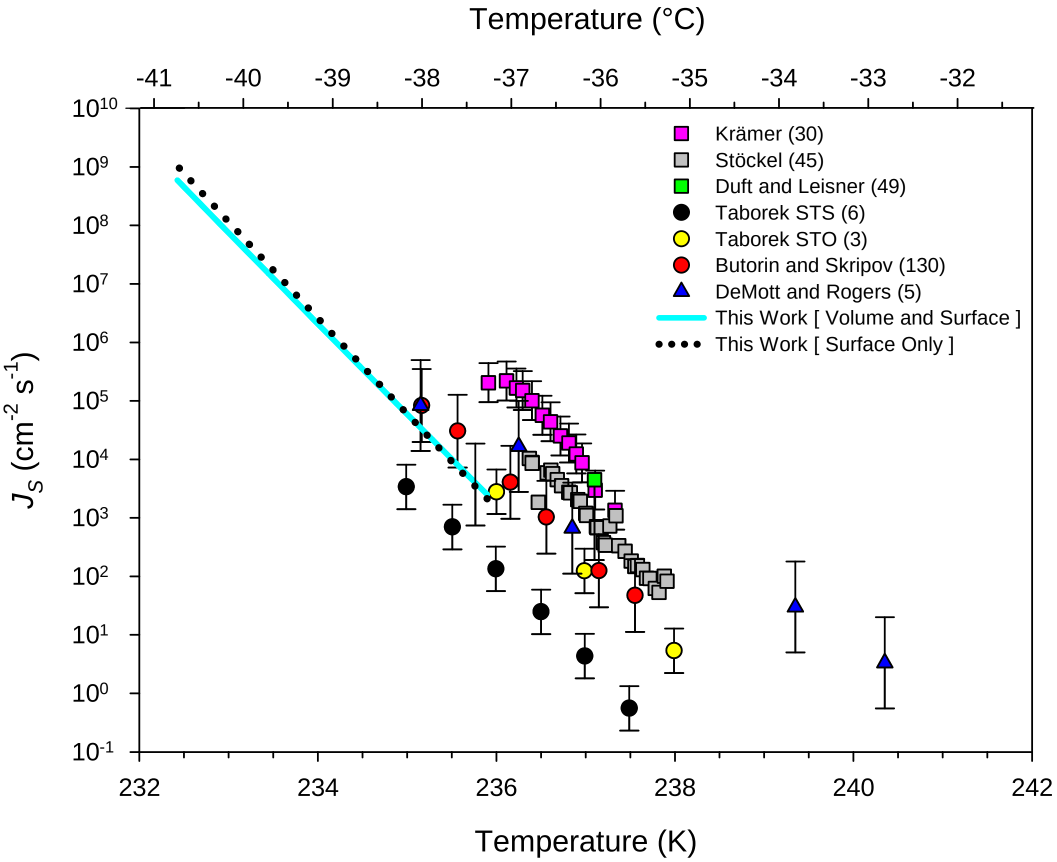

Figure 7.6: Comparison of model results for $J_S(T)$ assuming surface-only or both volume and surface nucleation with literature values. Literature values were obtained by application of Equation 2.10 to the $J_V(T)$ values in Figure 7.5. Mean radii used in the conversion are given in parentheses in the legend. Ambient phase and surfactant designations follow from Figure 7.5.

factor of five. The literature values in Figure 7.6 have been obtained by the conversion of those in Figure 7.5 using the approach of Tabazadeh *et al.* (Equation 2.10).[34] The $J_S(T)$ values from surface-only runs correspond well with the literature values. In addition, the $J_S(T)$ values from the volume and surface runs agree extremely well with both the surface-only results and the literature values. The similarity of the $J_S(T)$ curves suggests the predominance of surface-based nucleation for our range of particle sizes, as even with the additional degree of freedom provided by volume nucleation in the surface and volume runs, the results strongly resemble the surface-only case. This is a reflection of the similarity of the χ values for these runs noted above.

It is difficult to assess whether volume nucleation occurs to some small extent, or is merely a means of improving fits to the experimentally measured size distributions within the model. Either could account for the slightly improved value of χ when volume nucleation is considered alongside surface nucleation. The observed shift of the $J_V(T)$ curve in the combined volume and surface run, however, suggests that these values may not be meaningful, and are merely the result of the model attempting to use both processes to fit experimental results which can be fit almost equally well using only surface-based nucleation (for this reason, an error bar is not provided for the $J_V(T)$ curve from the combined volume and surface run in Figure 7.5).

Regardless, these results demonstrate the importance of surface-based nucleation for describing the freezing of droplets with radii between 1 and 2.7 μm. The surface area-to-volume ratio varies from ~ 3 to 1 μm^{-1} over this size range. Recalling the discussion of surface vs. volume-based nucleation in Section 2.4, it has been previously suggested that surface nucleation will be most significant for particles with radii less than 1 μm,[28] which will have even larger surface area-to-volume ratios. To further assess the apparent predominance of surface nucleation in our studies, it is therefore desirable to extend our range of experimental radii below 1 μm, perform similar model runs, and compare the resulting $J_V(T)$ and $J_S(T)$ curves with those above.

CHAPTER EIGHT

SMALL FLOW TUBE STUDIES

8.1. Introduction

The generation of particles with radii less than 1 μm following conditioning is difficult in the cryogenic flow tube apparatus. A flow velocity of 3 cm s^{-1} provides sufficient time for heat transfer from the tube wall and fins to the flow, but also provides ample time for particle growth by condensation and diffusion-limited exchange processes (Kelvin effect and mass transfer). An increase in flow velocity would reduce particle residence times, and hence, particle growth, but would need to be accompanied by a corresponding increase in tube length to ensure adequate thermal transfer, which is not possible in the current configuration. To accommodate these seemingly conflicting requirements, a new, smaller, cryogenic flow tube apparatus has been constructed. The small flow tube has a narrower diameter and longer section lengths, providing sufficient radial heat transfer for faster flow velocities (shorter residence times), and dramatically reducing the propensity for buoyancy-induced recirculation. The primary objective of this apparatus is the generation of conditioned aerosols smaller than 1 μm, in order to extend our range of accessible surface area-to-volume ratios for the investigation of surface vs. volume nucleation. The following chapter details the small flow tube apparatus, and the results from the related freezing experiments and modelling studies. The $J_V(T)$ and $J_S(T)$ curves are assessed in terms of the predominant nucleation process, and are compared against the corresponding curves in the previous chapter.

8.2. Experimental

8.2.1. Small Flow Tube Apparatus

The small flow tube apparatus is depicted schematically in Figure 8.1. The general design and construction are similar to that of the cryogenic flow tube (Chapter 4). The small flow tube comprises two copper sections, each with an inner diameter of 2.6 cm, and outer diameter of 2.9 cm. The top section is 121.9 cm long, and the bottom section is 91.4 cm long. The copper sections are joined by a stainless steel vacuum adaptor, which has an inner diameter of 2.9 cm on each end to accommodate the sections, and narrows to 2.5 cm between the sections to provide thermal separation. The lower end of the bottom section is soldered to the top of a 2.6 cm i.d. copper cross. The horizontal ends of the cross are soldered to stainless steel observation ports capped with 3.8 cm diameter KRS-5 windows, thus forming the observation cell. A 7.6 cm length of copper pipe (2.6 cm i.d., 2.8 cm o.d.) is soldered to the bottom of the copper cross, and is connected to the exhaust line.

The temperature control system is identical to that of the cryogenic flow tube (Section 4.3), with two concentric, 0.6 cm i.d. copper cooling coils affixed to the outer wall of each section with thermally-conductive epoxy. Four type T thermocouples are placed along the outer wall of each section: 15.2 cm from each end of the top section, and at 30.5 cm intervals in between; and 11.4 cm from each end of the bottom section, and at 22.9 cm intervals in between. The LabVIEW control program and feedback loop maintain average section temperatures within ± 0.2 K of set-point values. A 5 cm-long post-cooling coil is wrapped around the short length of pipe below the observation section. The outlet coolant flow from the bottom tube section passes through this coil,

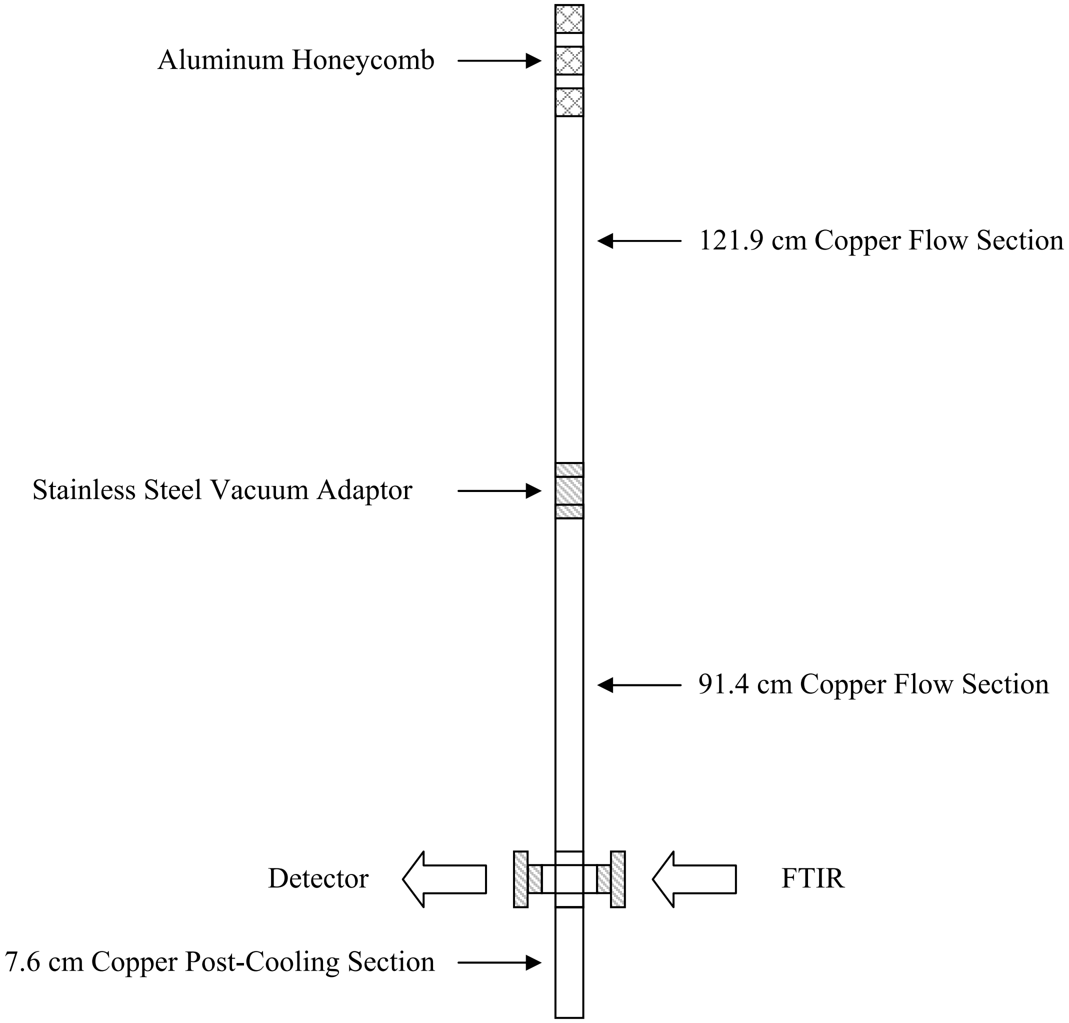

Figure 8.1: Schematic diagram of small flow tube apparatus. The copper flow and post-cooling sections are wrapped in 0.6 cm i.d. copper cooling coils (not shown).

cooling the attached length of pipe. This helps to provide uniform cooling of the observation section, as well as smooth temperature transitions between the observation section and exhaust, thereby reducing the potential for buoyancy-induced recirculation.

The flow tube assembly is insulated by concentric layers of foam pipe insulation, pink fibreglass insulation, and aluminum bubble wrap. The bubble wrap serves as the outer layer, and prevents radiative heat transfer from the laboratory environment. The insulated assembly is mounted on two C-shaped supports placed under the observation ports. A series of ring clamps hold the assembly in the centre of a stainless steel support structure.

The flow control system outlined in Section 4.4 is also used for the small flow tube. Aerosols are produced at 3 SLPM, typically by atomization or heterogeneous condensation, and introduced to the flow tube *via* a heated inlet. The inlet is a smaller-scale version of that used in the cryogenic flow tube, and is composed of concentric 0.95 cm o.d. (copper) and 1.3 cm o.d. (stainless steel) tubes. The inlet is passed through a modified version of the stainless steel vacuum adaptor described above. The bottom half of the adaptor has an inner diameter of 2.8 cm for attachment to the top section of the flow tube, while the top half of the adaptor has an inner diameter of 1.3 cm to accommodate the inlet. The inlet is passed through the adaptor, and extends 25.4 cm into the top section interior.

Carrier gas is introduced axially to the aerosol flow at 3 SLPM *via* four, 0.32 cm o.d. inlets spaced equally around the top of the inlet adaptor. The axial introduction of carrier gas prevents flow recirculation in the inlet region (Section 4.5). To evenly disperse and pre-cool the carrier flow, it is passed over three, 2.54-cm lengths of aluminum honeycomb (Texas Almet, Inc.). The honeycomb has a cell size of 0.15 cm, and fits snugly between the aerosol inlet and inner flow tube wall.

For total flow rates of 6 SLPM (3 SLPM aerosol, 3 SLPM carrier), the mean flow velocity is approximately 20 cm s^{-1}, resulting in Re ~ 300 and Gr/Re^2 ~ 0.02 (for $\Delta T = 1$ K in Equation 4.1). Thus, the flow should be laminar and free from buoyancy-induced recirculation. Particle residence times are on the order of 10 s. To ensure that these seemingly short residence times are sufficient for the aerosols to reach the desired freezing temperatures, a typical cooling scenario was modelled in CFD. Figure 8.2 shows the model results for an aerosol flow of 3 SLPM emerging from the bottom of the inlet at 283 K, and mixing with pre-cooled carrier gas (3 SLPM) at the top section temperature of 240 K. The flow clearly attains the bottom section temperature of 233 K before the observation cell. Note that only a 30° section of the tube geometry is shown; by application of symmetry, the model results can be extended to the full 360° geometry.

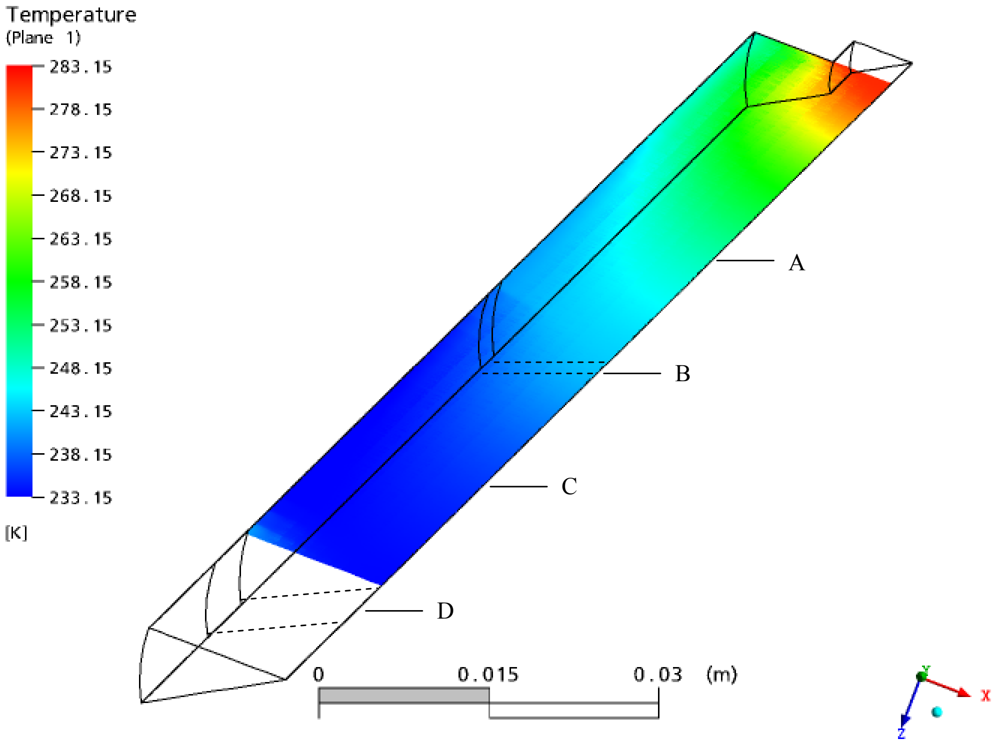

Figure 8.2: Temperature profile for a typical scenario in the small flow tube [3 SLPM aerosol flow at 283 K, 3 SLPM carrier flow at 240 K, cooling profile from 240 K (top section) to 233 K (bottom section)]. Location designations are as follows: A, top tube section; B, stainless steel vacuum adaptor; C, bottom tube section; and D, observation cell. Tube section (30°) is shown to scale, and is rotated for clarity.

8.2.2. Freezing Experiments

Freezing experiments in the small flow tube were conducted in a similar fashion to those described in Section 5.2 for the cryogenic flow tube. The top section temperature was maintained at 240 K to condition the aerosols, and the bottom section temperature (candidate freezing temperature) was reduced from 240 – 230 K over successive trials. Since the objective was to probe the freezing of smaller particles, aerosols were generated solely by heterogeneous condensation on NaCl particles. The NaCl particles were produced by the stepwise drying of aerosols produced by atomizing solutions of varying concentration (0.002, 0.02, and 0.2 M). The aerosols were first dried by passing through a 120 cm long Nafion dryer, composed of a 1.3 cm i.d. Nafion membrane enclosed within a 5 cm i.d. glass tube. A counter-flow of dry nitrogen of 20 – 25 SLPM was passed through the outer tube. Subsequent drying was achieved by passing the sample through a 25 cm long silica gel dryer, in which the aerosols travelled through a 1.3 cm i.d. inner tube (fine mesh) enclosed within a 10 cm i.d. outer tube filled with the desiccant. A humidified carrier flow of 0.4 SLPM was added to the samples prior to their introduction to the flow tube. Extinction spectra of the flowing aerosols were obtained in the observation cell, and analyzed using the aerosol characterization procedure.

8.3. Results and Discussion

8.3.1. Aerosol Volume and Size

Initial studies were conducted using the 0.02 M NaCl solution, with both tube sections held at the conditioning temperature of 240 K. The resulting extinction spectra are shown in Figure 8.3. To assess the drying efficiency, no humidified carrier was

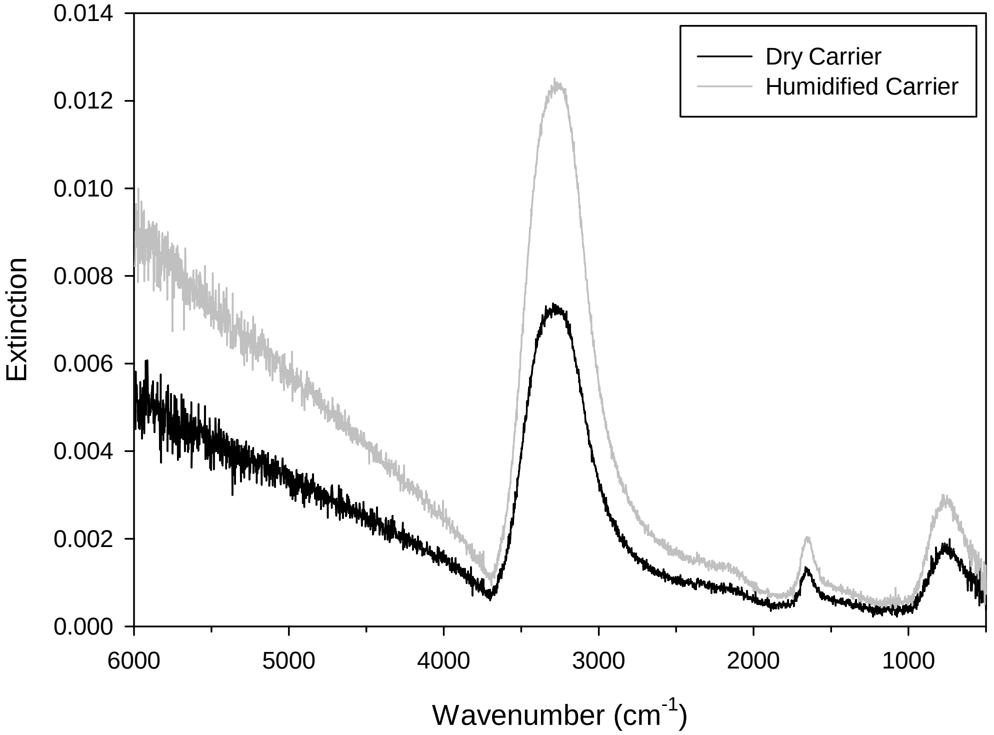

Figure 8.3: Extinction spectra for dried aerosols produced by atomizing 0.02 M NaCl solution. Spectra are shown for samples with and without the introduction of 0.4 SLPM humidified carrier flow.

added initially (black curve). The broad absorption features associated with liquid water are clearly visible for this sample, indicating that the aerosols were not completely dry. The corresponding volume distribution in Figure 8.4 shows that the drying was sufficient to reduce particle sizes below 1 μm, with a maximum in the distribution at a radius of ~ 0.6 μm. Hence, the main objective of the small flow tube study was achieved. Addition of the humidified carrier increased the total volume of particles and, in turn, the extinction intensity, while only increasing particle size to 0.63 μm (grey curves in Figures 8.3 and 8.4). For these reasons, the humidified carrier was used in all subsequent trials conducted with the bottom tube section at candidate freezing temperatures between 240 – 230 K.

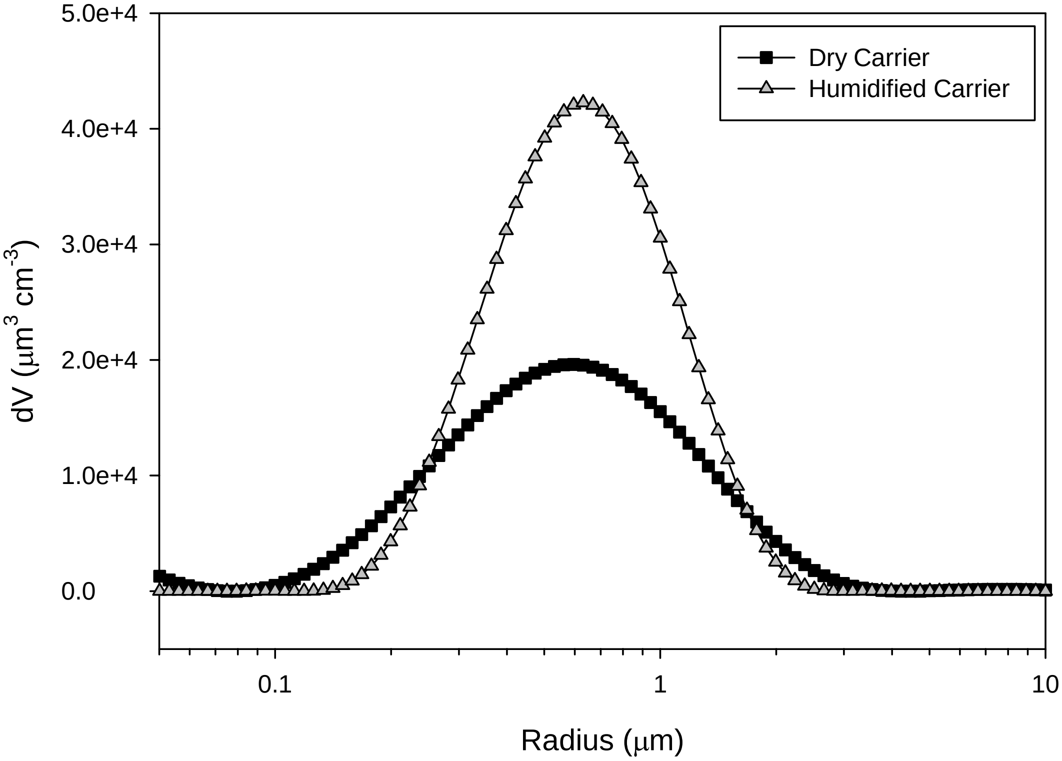

Figure 8.4: Volume distributions of aerosols obtained from extinction spectra in Figure 8.3.

8.3.2. Freezing Curves

The freezing curve for the aerosols produced from the 0.02 M solution (following drying and humidification) is plotted in Figure 8.5. The freezing point, coinciding with a volume fraction of ice of 0.5, is at approximately 234 K. This is lower than the value of 236.2 K obtained for small, medium, and large particles in the cryogenic flow tube (Section 6.3.2). The potential for solute effects (heterogeneous nucleation and/or freezing point depression) in the 0.63 μm particles produced from the 0.02 M solution is greater than that for the small particles in the cryogenic flow tube (produced from 10^{-4} M solution), because of the higher solute concentration. To attempt to rule out these effects in the small flow tube studies, freezing experiments were conducted using the 0.002 and

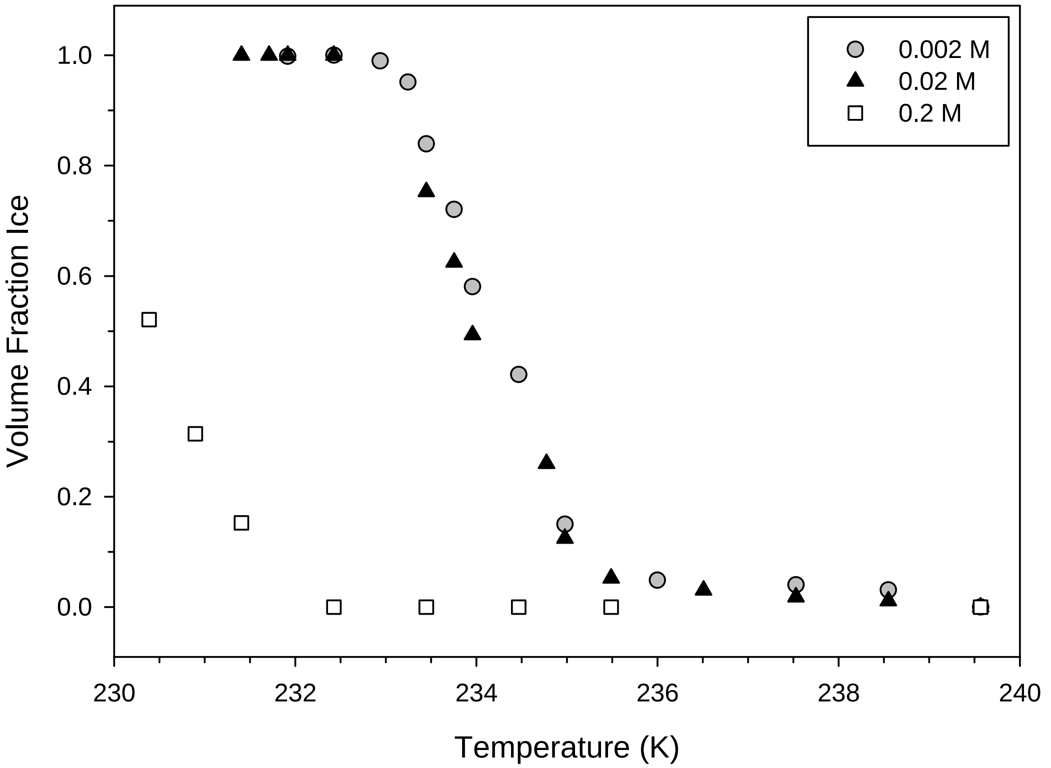

Figure 8.5: Freezing curves for aerosols produced by drying and humidifying atomizer output using 0.002, 0.02, and 0.2 M NaCl solutions.

0.2 M solutions for comparison. Identical drying and humidification techniques were employed. The resulting freezing curves are plotted alongside the 0.02 M results in Figure 8.5. The curve for the 0.2 M solution shows significant freezing point depression to ~ 230.4 K, while that for the 0.002 M solution agrees well with that of the 0.02 M solution at ~ 234 K. It therefore appears that freezing is independent of NaCl concentration for aerosols prepared from solutions with concentrations of 0.02 M or less. It should be noted that the conditioned aerosols produced from the 0.002 M solution are slightly larger, with a maximum in the volume distribution at a radius of 0.75 μm (Figure 8.6).

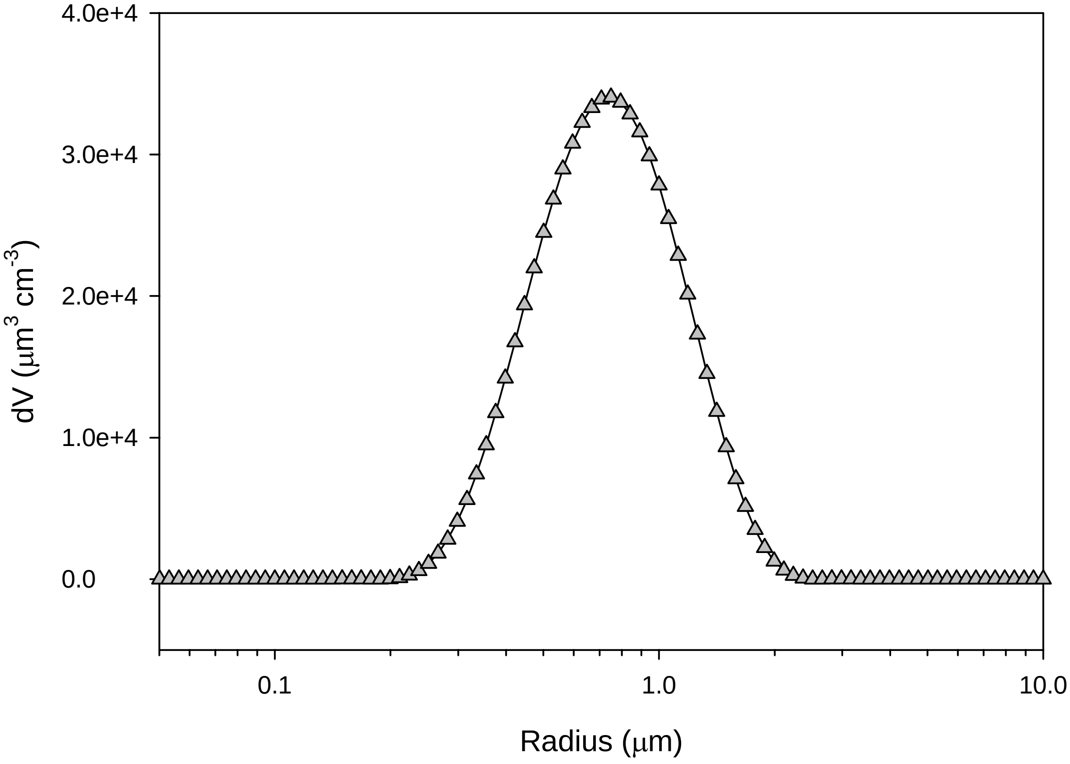

Figure 8.6: Volume distribution for conditioned aerosols produced by drying and humidifying atomizer output using 0.002 M NaCl solution.

Disregarding solute effects, the observed shift in the freezing curves for the more dilute NaCl solutions (0.02 and 0.002 M) relative to the cryogenic flow tube results is attributed to the shorter residence times in the small flow tube. In the smaller tube, the aerosols are exposed to the candidate freezing temperature for less than 4 s, as opposed to about 35 s in the cryogenic flow tube. Thus, even though the aerosols reach the desired temperature in both tubes prior to spectroscopic observation, the longer exposure to the candidate freezing temperature in the cryogenic flow tube results in more freezing and mass transfer growth, increasing the volume fraction of ice. This systematic difference between the flow tubes prohibits direct comparison of the freezing curves. However, since the microphysics model takes into account the temperature profile and flow rate for each experimental distribution, the results from both apparatus can be considered simultaneously within the microphysics model.

8.3.3. Model Results

To extend our investigation of surface- and volume-based nucleation in the previous chapter to particles with smaller radii, and hence, larger surface area-to-volume ratios, model runs were performed using volume distributions from a collection of 44 freezing experiments: five distributions from experiments on the 0.63 μm particles produced from 0.02 M NaCl in the small flow tube; five distributions from experiments on the 0.75 μm particles produced from 0.002 M NaCl in the small tube; and the 34 distributions from the studies of small, medium, and large particles in the cryogenic flow tube (Section 7.3). Similar to our previous investigation, separate runs were performed under the assumptions of only volume-based nucleation, only surface-based nucleation, and both volume- and surface-based processes. The resulting values of χ in this case were 1690.3, 1358.9, and 1359.2, respectively, which are significantly higher than those obtained for the runs using only 34 distributions. It must be noted, however, that the values of χ determined from Equation 7.24 are not normalized to the number of distributions, and are intended solely for comparison of equivalent model runs (same number of input distributions). Irrespective of their magnitude, the above χ values indicate that the volume-only runs produced the worst reproductions of the 44 measured distributions, while the best reproductions were achieved in the surface-only and combined volume and surface runs.

The inclusion of the small flow tube data in the model runs results in similar trends in $J_V(T)$ and $J_S(T)$ as observed in the previous chapter (see Figures 7.5 and 7.6 and related discussion in Section 7.3). The $J_V(T)$ values from the volume-only runs correspond well with the literature values, while those from the combined volume and surface runs show a marked shift in temperature dependence (Figure 8.7). Meanwhile, the $J_S(T)$ values from the combined surface and volume runs show excellent correspondence with the values from the surface-only model runs, and with the literature values (Figure 8.8). The correspondence of the $J_S(T)$ curves is reflective of the similarity of the χ values for these runs noted above, and following from the analysis in the previous chapter, is suggestive of the predominance of surface-based nucleation in our freezing experiments.

The $J_V(T)$ and $J_S(T)$ curves from the combined volume and surface runs employing 44 input distributions are compared against those from equivalent runs using 34 input distributions in Figure 8.9. The 44 distributions cover particle radii between 0.63 and 2.7 μm, and surface area-to-volume ratios between ~ 5 and 1 μm^{-1}, as compared to the more limited range of the 34 distributions, which cover radii between 1 and 2.7 μm, and surface area-to-volume ratios between ~ 3 and 1 μm^{-1}. The smaller particles shift the $J_S(T)$ curve slightly, resulting in a steeper temperature dependence, and larger $J_S(T)$ values for most of our temperature range. However, the $J_S(T)$ values still agree within an order of magnitude, providing further support for the prevalence of surface nucleation over our range of particle radii. This is in sharp contrast to the behaviour observed for the $J_V(T)$ curves, which show dramatically disparate temperature dependence, and differ by as much as 9 orders of magnitude at the lower end of our experimental temperature range. This behaviour discounts the importance of volume-based nucleation in our studies and,

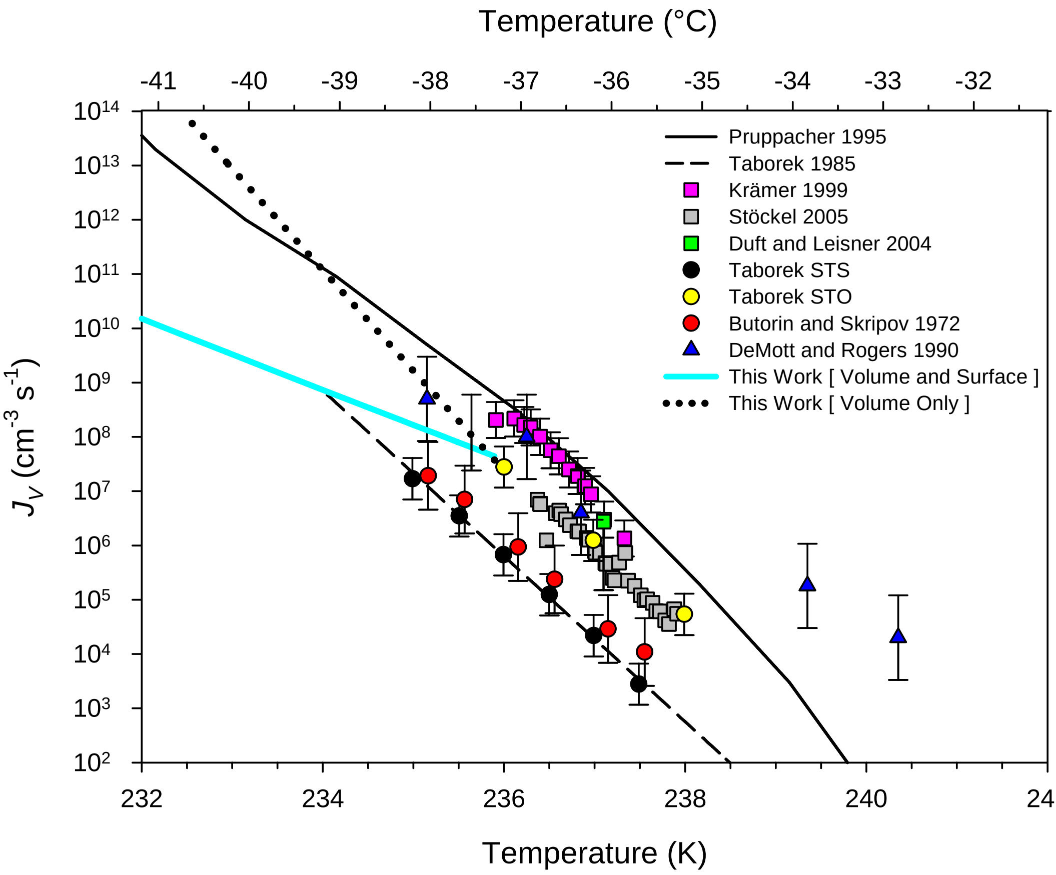

Figure 8.7: Comparison of $J_V(T)$ values from model runs incorporating small flow tube data with literature values. Ambient phase and surfactant designations follow from Figure 7.5.

as postulated in Section 7.3, is likely a result of the microphysics model using an additional degree of freedom to fit experimental data which can be described equally well using only surface nucleation. The $J_V(T)$ values in the combined volume and surface runs should therefore be considered only in relative terms, with no particular significance given to their magnitude or temperature dependence.

The preponderance of surface nucleation for water droplets with radii between 0.63 and 2.7 µm, suspended in air in a laminar aerosol flow tube, is in accordance with the theoretical basis of Djikaev *et al.*[26] and Tabazadeh *et al.*.[34] Since water will only

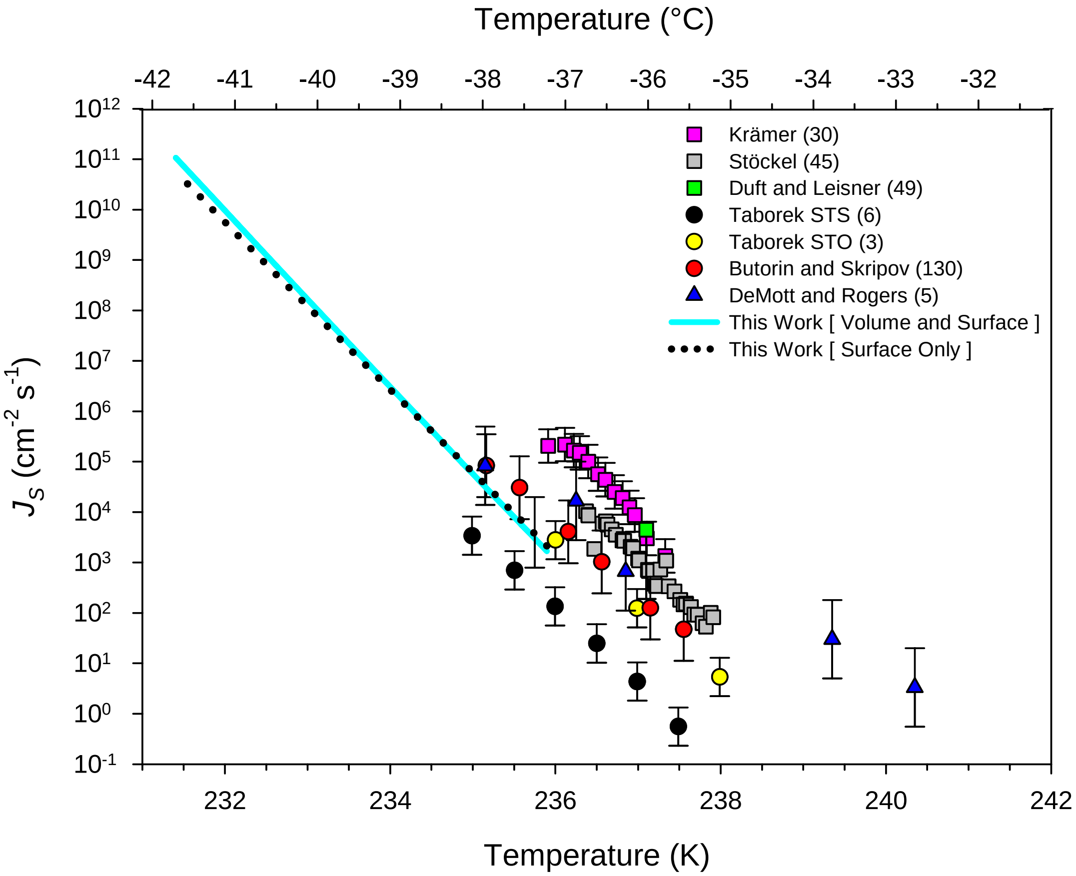

Figure 8.8: Comparison of $J_S(T)$ values from model runs incorporating small flow tube data with literature values. Ambient phase and surfactant designations follow from Figure 7.5.

partially wet ice,[39] the inequality in Equation 2.9 should hold, and hence, nucleation should be primarily surface-based. No previous measurements have been obtained for particles in our size regime suspended in air. The present studies therefore constitute an important addition to the field, and provide a novel and interesting perspective on the current debate regarding surface vs. volume nucleation.

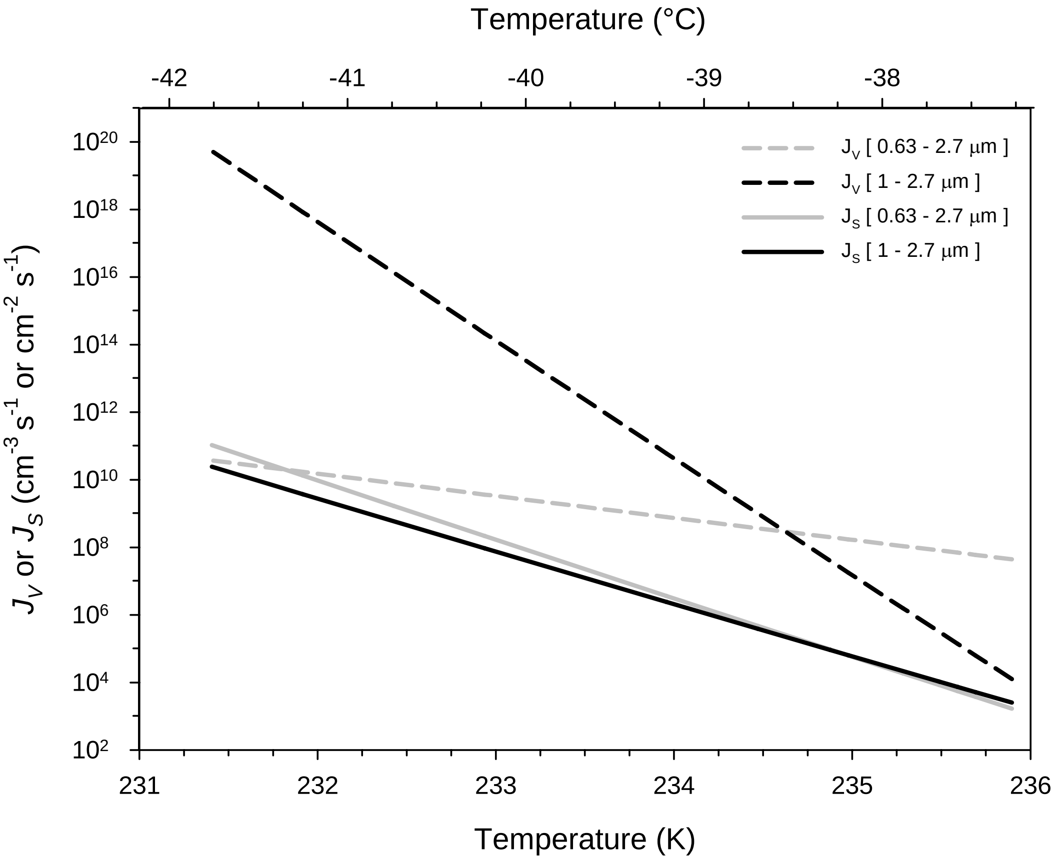

Figure 8.9: Comparison of $J_V(T)$ and $J_S(T)$ values from combined volume and surface model runs employing 44 experimental distributions (radii between 0.63 and 2.7 μm) and 34 experimental distributions (radii between 1 and 2.7 μm).

CHAPTER NINE

ICE CRYSTAL HABIT OBSERVATIONS

9.1. Introduction

The ice particles formed in the freezing experiments detailed in the preceding chapters will have crystal habits defined by the experimental conditions. Given the importance of crystal habit characterization for the parameterization of climate models (Section 2.6), an optical microscopy apparatus has been developed for the direct observation and imaging of ice particles in the cryogenic flow tube. The following chapter details the microscopy setup and approach, and demonstrates the utility of the apparatus for habit observation and classification. Particular interest has been paid to any habits formed from cubic ice-I_c, which is metastable over our range of experimental conditions. The imaging of particles also provides a basis for comparison with the results of the aerosol characterization procedure. In particular, the comparison of particle size distributions retrieved from images and FTIR spectra has been explored as an independent means of validating the output of the aerosol characterization procedure. This aspect of the study has been considered previously elsewhere.[102]

9.2. Experimental

9.2.1. Optical Microscopy Apparatus

The optical microscopy apparatus developed for particle imaging in the cryogenic flow tube is depicted schematically in Figure 9.1. The apparatus comprises a 20X objective (Olympus RMS20X, Thorlabs, Inc.) connected to a CCD (charge-coupled

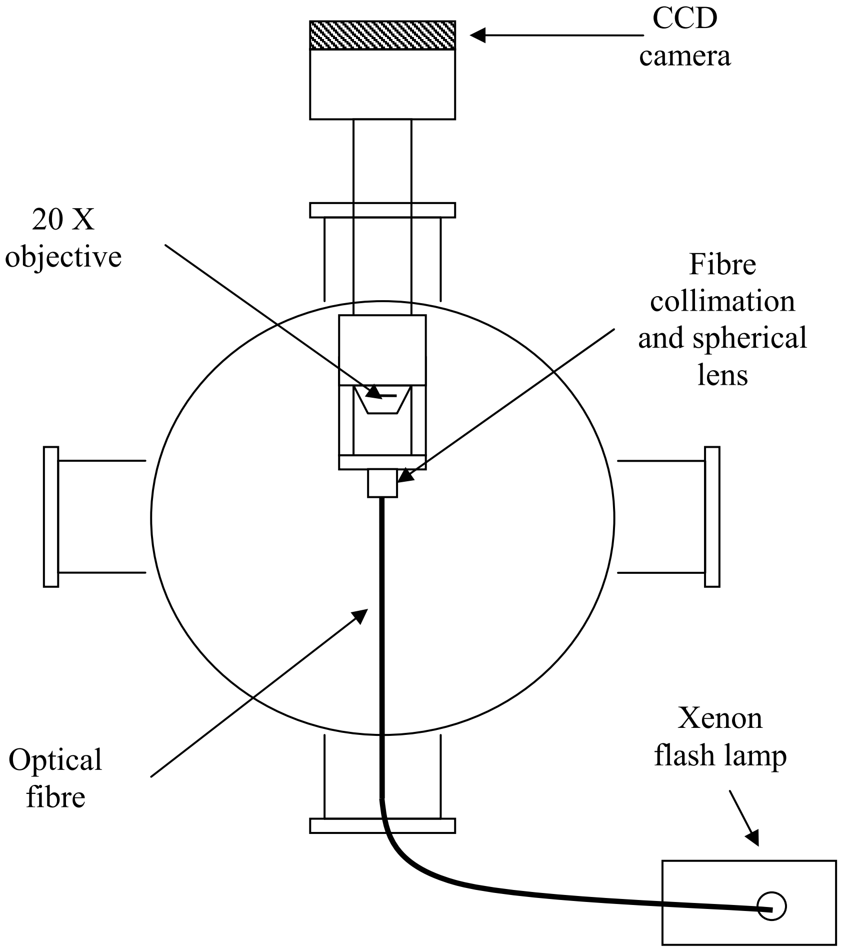

Figure 9.1: Optical microscopy apparatus in bottom section of cryogenic flow tube. Orthogonal ports (left and right) are used for spectroscopic observation.

device) camera (DC111, Thorlabs, Inc.) *via* a 19.0 cm long stainless steel tube (2.54 cm i.d., 3.18 cm o.d.). The objective has a focal length of 9 mm and a working distance of 1.2 mm. The CCD camera has a resolution of 640 x 480 pixels, with a pixel size of 7 µm. The greyscale dynamic range of each pixel ranges from 0 (black) to 255 (white). The maximum sensitivity of the CCD is centered at a wavelength of ~ 0.5 µm, corresponding with the wavelength of maximum intensity produced by a Xenon flashlamp (L4955-11, Hamamatsu Corp.). Illumination is provided by ~ 5 W pulses from the flashlamp, which are triggered by the rising edge of a square wave produced by a waveform generator at ~ 150 Hz. A 600 μm optical fibre (M29L01, Thorlabs, Inc.) carries the pulses to an aluminum attachment on the microscope assembly, which houses the collimating and focussing optics (Thorlabs F230SMA-A fibre collimation package and 1.27 cm diameter plano-convex spherical lens, respectively). The focussed light (focal point) is positioned in the focal plane of the microscope objective by adjusting the height and lateral position of the aluminum attachment. A magnified image is produced on the CCD by the objective and a 2.54 cm diameter lens with a focal length of 180 mm (Thorlabs, Inc.) within the stainless steel tube. With 20X magnification, one pixel in the image corresponds to 0.35 μm, resulting in image dimensions of 224 x 168 μm.

The CCD camera is interfaced to a laboratory PC using FlyCapture software (Point Grey Research, Inc.), which allows real-time image viewing and adjustment of the camera shutter speed and gain. Using FlyCapture source code, a program has been developed in our laboratory to record images from the camera. In typical operation, 100 background images are acquired prior to the introduction of aerosols for a given set of experimental conditions. An aerosol flow is then initiated, and images are acquired, 1000 at a time.

The bottom section of the cryogenic flow tube has been modified to accommodate the microscopy apparatus (Figure 9.1). Additional observation ports were constructed orthogonal to those used in spectroscopic observation, allowing the particles to be imaged at the same axial tube location. The ports are similar in construction to those described in Section 4.2 with respect to the FTIR measurements, but have different end plates. The end plate on one port is equipped with a 3.18 cm i.d. vacuum adaptor, through which the microscope is passed into the flow tube interior, while the end plate on the opposite port is equipped with a 7.6 cm long, 1.27 cm i.d. tube through which the optical fibre is passed. A bored-through rubber stopper holds the fibre in the tube centre, and seals the tube. The apparatus is positioned within the tube interior such that the focal plane of the microscope objective is in the radial centre of one of the quadrants formed by the fins.

The axial location of the microscopy apparatus is advantageous from the standpoint of imaging particles at the same location as the FTIR observations. This location is disadvantageous, however, as the aluminum attachment and fibre obscure the spectroscopic observation path. As a result, particle images and FTIR spectra cannot be obtained simultaneously. When the results of the two methods are to be compared, the images and spectra must be acquired sequentially, under the same experimental conditions.

9.2.2. Image Processing and Analysis

The 100 background images obtained for a given set of experimental conditions are averaged and subtracted from each image obtained once the aerosol flow has been initiated. Background subtraction enhances the contrast between the particle “shadows” and the rest of the image. This contrast serves as the basis for an image processing algorithm developed in our laboratory to extract particle size distributions from collections of images. The algorithm consists of separate pre-processing, particle identification/isolation, and size determination steps.

In the pre-processing step, the algorithm identifies the subset of images containing particles in focus. By focussing the collimated light from the optical fibre onto the focal plane of the microscope objective, maximum intensity is provided to particles in the focal plane, resulting in sharper particle shadows with darker greyscale intensities. Less intensity is provided to particles outside of the focal plane, resulting in diffuse, blurry shadows with brighter greyscale intensities. The algorithm scans through the images, and disregards those which have no pixels with greyscale intensities less than 200. The remaining images are retained for subsequent analysis.

In the identification/isolation step, the algorithm identifies particle edges based on the first derivatives (slopes) of pixel intensity. The threshold slope corresponding with a particle edge is set by the user, and is used to discriminate between particles in- and out-of-focus in the pre-processed images. For particle shadows with slopes exceeding the set threshold, an edge-following algorithm (Papert's turtle[103]) selects the pixels that form a continuous and closed chain along the shadow edge, bounding and isolating the individual particles. When multiple, in-focus particles are present in a given image, each particle is considered separately.

In the size determination step, a polygon is fit to the pixel chain representing each particle edge. The cross-sectional area of each particle shadow is calculated from the fit. The equivalent spherical radius of each particle is then determined from its area, and a size distribution is constructed by counting the number of particles in user-defined size bins. Typically, 0.2 μm bins are used, covering radii between 0 and 12 μm. The determination of equivalent spherical radii allows the direct comparison of size distributions with those obtained from FTIR spectra using the aerosol characterization procedure when Mie theory (assuming spherical particles) is used to compute basis set spectra.

A modified version of this algorithm has been developed to aid in the classification of crystal habits from particle images. The pre-processing and identification/isolation steps are as described above, while the final step is varied to determine rudimentary shape information from the particle shadows. The modified algorithm determines the aspect ratio of the polygon fit to each particle shadow. All particles with aspect ratios of unity are classified as spherical, and are separated from those with non-unity values.

The remaining non-spherical particles are then classified by visual inspection. When pristine geometric habits (*e.g.* hexagons) are observed, a ray-tracing algorithm developed in our laboratory is used to verify the observed habits. The algorithm uses a geometric optics approach, and simulates the particle shadows formed when a bundle of light rays interacts with a given geometric shape. The shape can be rotated with respect to the direction of incident light to best reproduce the particle shadows. Good visual agreement between the observed and simulated shadows is taken as confirmation of the proposed geometric habit.

9.2.3. Imaging Studies

Particle imaging studies have been conducted to observe the crystal habits formed under different experimental conditions. The key objective of these studies was to demonstrate the effectiveness of the microscopy apparatus for observing and classifying crystal habits, and for assessing the frequency of occurrence of different habits for a given set of experimental conditions. The imaging studies employed various temperature profiles in the cryogenic flow tube, with a conditioning temperature of 240 K, and candidate freezing temperatures between 240 and 228 K. The number of conditioning sections was varied between two and zero to vary the residence time at the candidate freezing temperature. The ultrasonic nebulizer was used to generate pure water aerosols, which were introduced to the flow tube at 3 SLPM in all studies. The dry nitrogen carrier flow was varied between 0 to 7 SLPM for each temperature profile, resulting in total flow rates between 3 and 10 SLPM. Reducing the total flow rate extends the residence time of aerosols in the flow tube, providing more time for nucleation and growth by secondary processes. In addition, reducing the total flow rate and, in turn, the flow velocity, increases the value of the buoyancy parameter in Equation 4.1. Buoyancy-induced recirculation is generally undesirable in freezing experiments, as it causes particle residence times and flow pathways to vary from the ideal, laminar case; however, it was believed that such recirculation could produce interesting particle habits. For each temperature profile and flow rate, 10000 sample images were obtained. The shape determination algorithm was used to separate the spherical and non-spherical particles, the latter of which were characterized using both visual inspection and the ray-tracing algorithm.

9.2.4. Validation Studies

Aiming to corroborate the output of the aerosol characterization procedure, validation studies were performed in the cryogenic flow tube with all four sections at room temperature, using pure water droplets produced by the ultrasonic nebulizer. For an aerosol flow of 3 SLPM, and dry nitrogen carrier flow of 7 SLPM, 33000 images were recorded. Several FTIR spectra were obtained under the same conditions. Particle size distributions were then determined from the images and spectra using the image processing algorithm and aerosol characterization procedure (using Mie theory for basis set generation), respectively. At room temperature, all droplets are liquid, and spherical in shape; hence, the assumption of particle sphericity in each method is valid.

9.3. Results and Discussion

9.3.1. Crystal Habit Observation and Classification

Characteristic crystal habits observed in the imaging studies are shown in Figure 9.2. The majority of habits observed are spherical [Figure 9.2(a)], with a propensity for agglomerate formation by contact freezing [Figure 9.2(b)-(c)]. Pristine geometric habits, such as the hexagonal prism in Figure 9.2(d), are also observed. More common, however, are irregular habits formed by mass transfer growth upon an initial frozen droplet [Figure 9.2(e)], and by the combination of mass transfer and contact freezing [Figure 9.2(f)]. Clearly evident in Figure 9.2 is the high level of structural detail imparted by the 0.35 µm pixel resolution.

The assessment of the relative frequencies of occurrence of the different habits, beyond the general trends noted above, requires a large statistical sample of particle images. This assessment is therefore limited by the fact that not all of the 10000 images recorded for each set of experimental conditions contain particles, and of those that do, not all of the particles are in focus. The percentage of images yielding in-focus particle shadows is referred to as the relative particle frequency (*RP*), expressed as follows:

$$RP = \frac{n_p}{n_i} \times 100\% \tag{9.1}$$

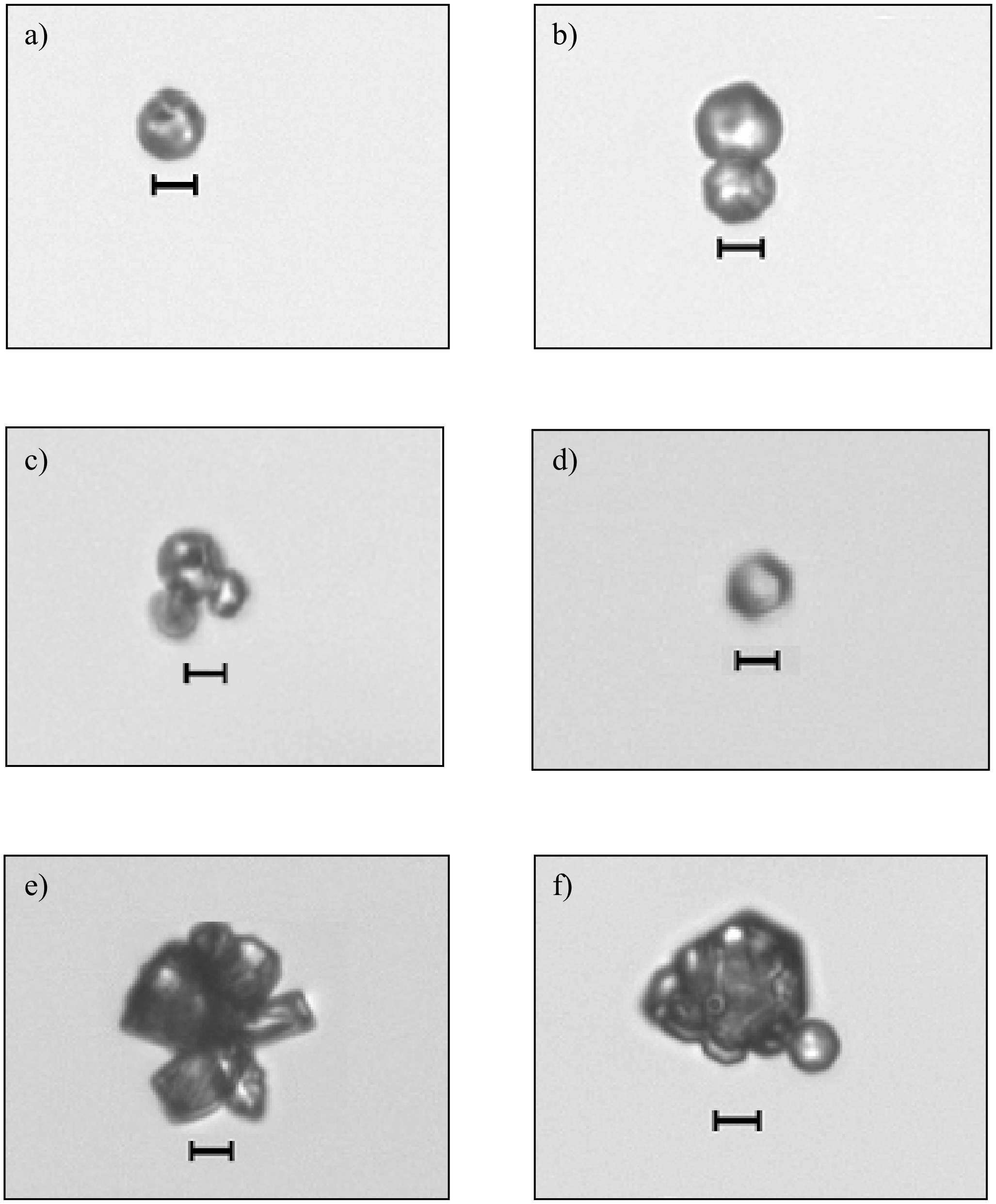

Figure 9.2: Characteristic ice crystal habits observed in imaging studies: (a) spherical frozen droplets; (b) dimers formed by contact freezing; (c) trimers formed by contact freezing; (d) pristine geometric habits (hexagons); (e) irregular habits formed by mass transfer growth from a central frozen particle; and (f) irregular habits formed by mass transfer and contact freezing. The scale marker in each image represents a distance of 7 μm.

where n_p and n_i are the number of in-focus particles and images, respectively. For each set of experimental conditions in the imaging studies, *RP* is typically on the order of 10%. This low value is attributed to two factors: (1) the small dimensions of the area imaged – a 224 x 168 μm plane located 1.2 mm above the objective tip – limits the number of in-focus particles; and (2) the microscope objective and aluminum attachment disturb the flow in the observation region, directing particles around the apparatus, and away from the focal plane.

To obtain larger statistical samples, it is necessary to record correspondingly larger numbers of images. As an illustrative case, 53000 images were recorded for a temperature profile in which all four cryogenic flow tube sections were held at 236 K, with 3 SLPM aerosol flow and 7 SLPM dry nitrogen carrier flow. From these images, 8451 in-focus particles were observed (*RP* ~ 16%). The distribution of these particles amongst the different crystal habits is shown in Figure 9.3. The observed particles are predominantly spherical (84.3%), on account of the rapid cooling and subsequent freezing that occur when spherical droplets produced at room temperature are introduced into an environment maintained at 236 K. Of the remaining non-spherical particles, the majority are classified as irregular (14.1%), with small numbers of agglomerates (1.3%) and pristine geometric habits (0.3%). The above results demonstrate the utility of the microscopy apparatus as a platform for habit observation and classification, fulfilling the main objective of the imaging studies.

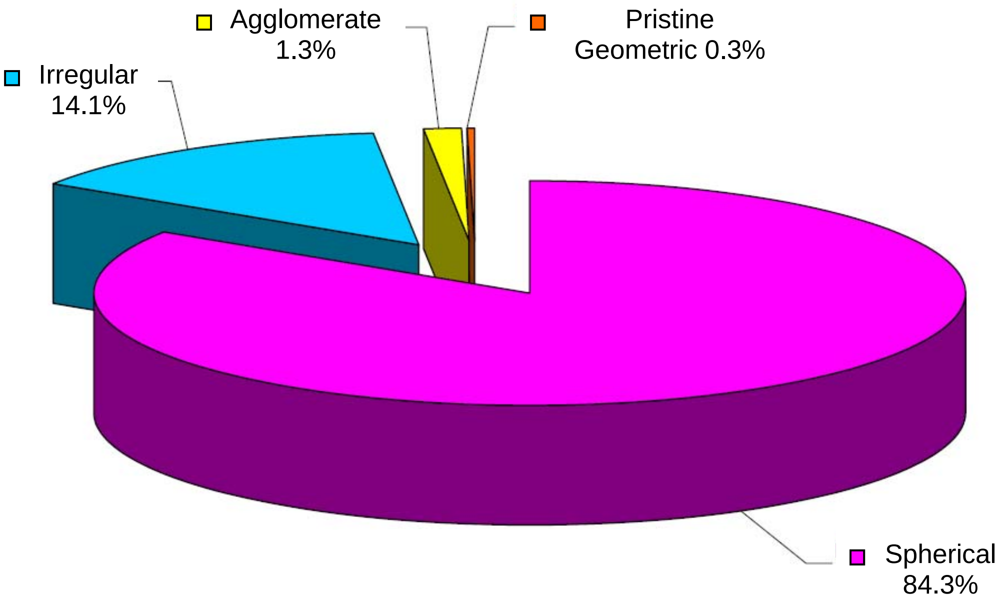

Figure 9.3: Pie chart showing the relative frequencies of occurrence of different particle habits for a single set of experimental conditions (all tube sections at 236 K, 3 SLPM aerosol flow, 7 SLPM dry nitrogen carrier flow).

9.3.2. Pristine Geometric Crystal Habits

Particles were classified as pristine geometric based on the shape of the bright spot in the particle shadow. Shadows with a hexagonal bright spot were considered to be hexagonal columns, with the bright spot arising due to light transmission through the basal facets, as supported by ray-tracing simulations (Figure 9.4). Shadows with a rectangular bright spot were also considered to be hexagonal columns, with the bright spot in these cases arising due to light transmission through the side facets. This was also supported by ray-tracing simulations (Figure 9.5).

Almost all of the pristine geometric particles observed were classified as hexagonal columns based on the above criteria. There was, however, one particle in

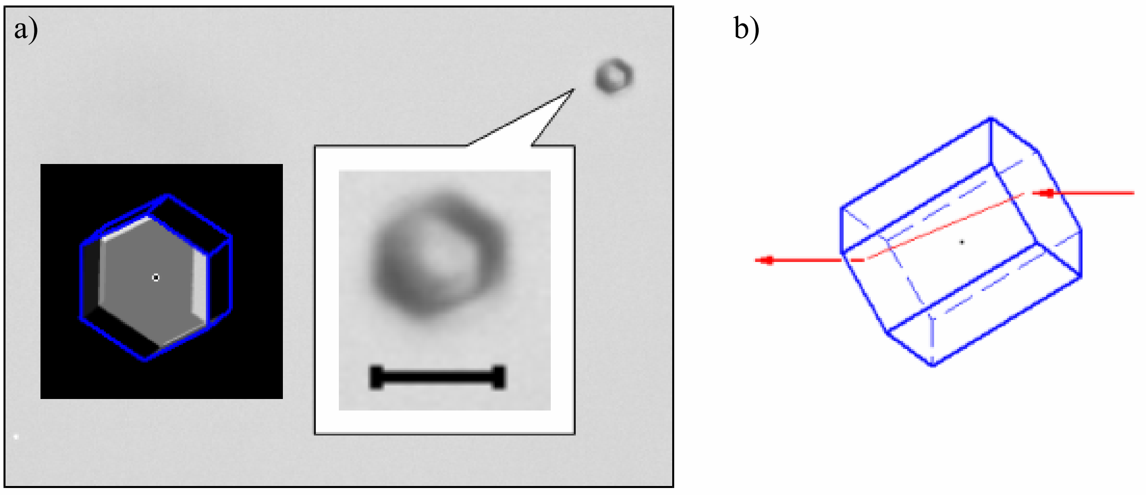

Figure 9.4: (a) Expanded view of particle with hexagonal bright spot and comparison with results of ray-tracing algorithm for (b) a hexagonal column with light transmission through basal facets.[104]

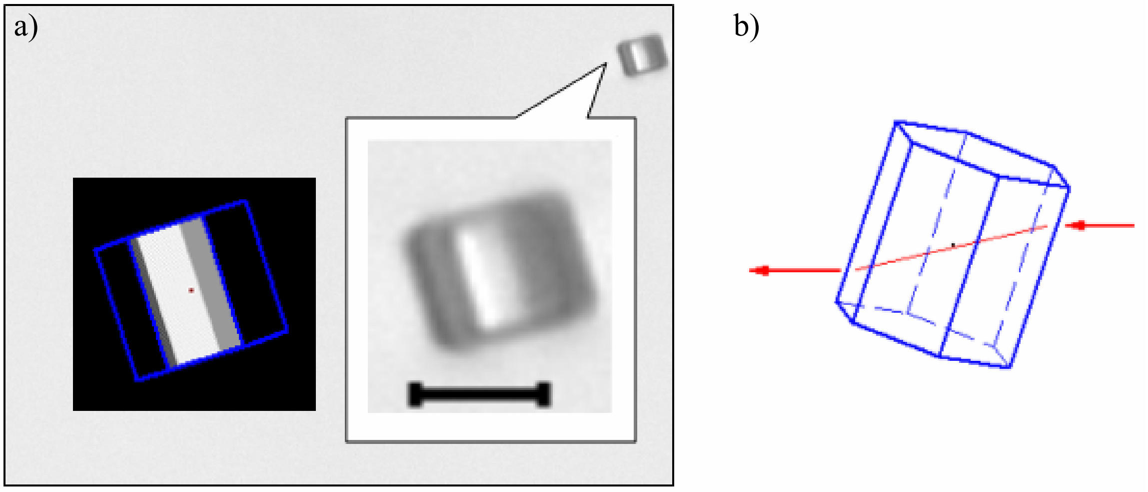

Figure 9.5: (a) Expanded view of particle with rectangular bright spot and comparison with results of ray-tracing algorithm for (b) a hexagonal column with light transmission through side facets.[104]

over 100000 recorded images having a square bright spot. The image containing this particle was recorded with all four flow tube sections at 236 K, with 3 SLPM aerosol flow, and no dry nitrogen carrier flow. The square spot could only be reproduced by the ray-tracing algorithm when decagonal crystal geometry was employed, as shown in Figure 9.6. Recalling the discussion in Section 2.6, decagonal crystal habits are formed from ice-I_c nuclei [Figure 2.7(b)], providing promising, yet far from conclusive, experimental evidence for the formation of this metastable phase under atmospheric temperature conditions. Unfortunately, additional studies performed under the same experimental conditions were unable to reproduce this particle, which can likely be attributed to the rapid conversion of ice-I_c to ice-I_h.

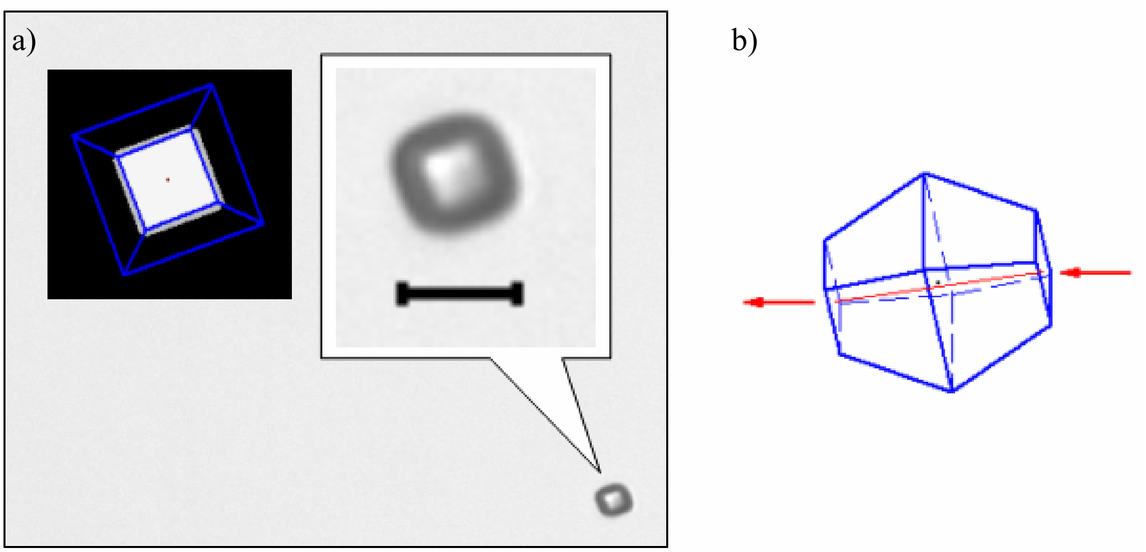

Figure 9.6: (a) Expanded view of particle with square bright spot and comparison with results of ray-tracing algorithm for (b) a decagonal particle with light transmission through basal facets.[104]

9.3.3. Validation of Aerosol Characterization Procedure

From the 33000 particle images recorded at room temperature in the validation studies, only 608 spherical droplets were observed and analyzed by the image processing algorithm. The resulting value of RP was less than 2%. This value was lower than in the particle imaging studies because of the higher partial pressure of water droplets at room temperature. Evaporative losses are more pronounced at room temperature, with smaller droplets evaporating completely due to the Kelvin effect. From the aerosol characterization procedure, the total number density of particles in the FTIR observations was on the order of 10^6 particles cm^{-3}. The size distribution histogram from the images shows excellent correspondence with the number distribution determined from FTIR spectra, as illustrated in Figure 9.7. This correspondence provides independent validation of the aerosol characterization procedure, which is extremely important given the extensive use of the procedure in our studies.

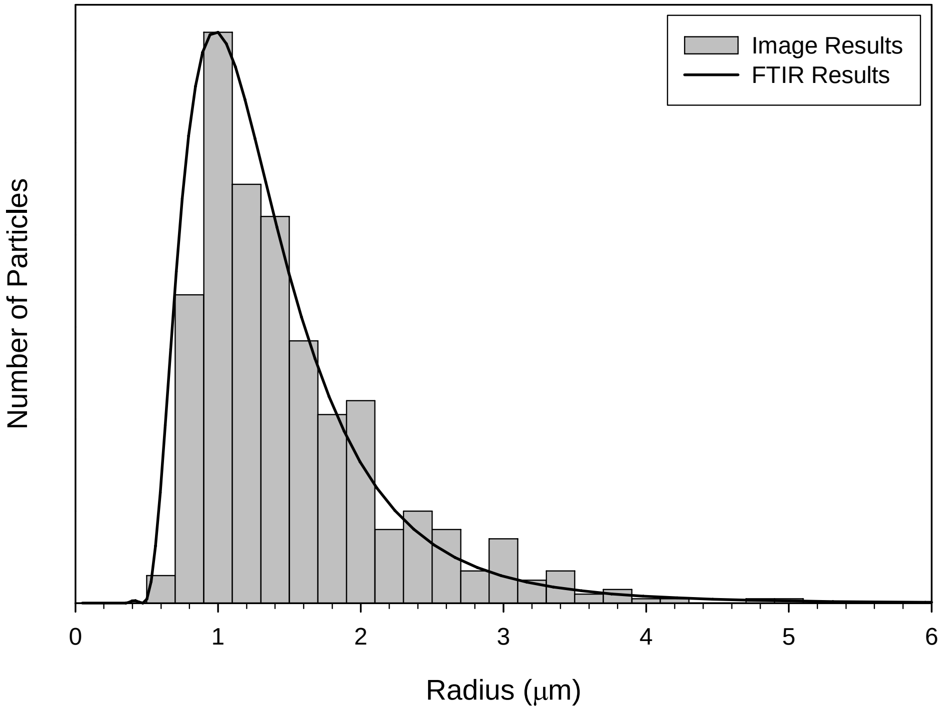

Figure 9.7: Comparison of particle size distribution from image processing algorithm with that obtained from FTIR spectra using the aerosol characterization procedure (all tube sections at room temperature, 3 SLPM aerosol flow, 7 SLPM dry nitrogen carrier flow). The FTIR results are scaled for comparison.

CHAPTER TEN

CONCLUDING REMARKS

10.1. Conclusions

The results presented in this work provide new insight into the fundamental microphysical behaviour of supercooled water aerosols, particularly with respect to homogeneous ice nucleation under the conditions of the upper troposphere and stratosphere. Extinction measurements of supercooled water aerosols with radii of 1 – 2.7 μm were performed in a cryogenic flow tube apparatus. The spectra showed increased "ice-like" character as the temperature was reduced, reflecting the formation of clusters of water molecules. Cluster formation has a profound effect on the complex indices of refraction, causing both the real and imaginary components to more closely resemble the values for ice with decreasing temperature. Our new, temperature-dependent indices of refraction for supercooled water should therefore be employed in retrievals from remote sensing and laboratory studies performed at atmospherically-relevant temperatures, in order to distinguish between the contributions of supercooled water and ice.

These new values were input into our aerosol characterization procedure and used to retrieve volume distributions of supercooled water and ice aerosols from FTIR spectra measured between 240 – 230 K. Freezing curves determined from the above distributions showed a homogeneous nucleation point of 236.2 K for our micrometre-sized water aerosols, in good agreement with the results from the temperature-normalized variance of difference spectra, and with literature values. To address the outstanding question of volume- vs. surface-based nucleation, the volume distributions were input into an aerosol microphysics model from which temperature-dependent homogeneous nucleation rates were determined assuming either, or both, nucleation mechanisms. The model results indicated that surface-based nucleation was the predominant process in our freezing experiments. This finding was supported by additional model studies incorporating volume distributions from freezing experiments on aerosols with radii of 0.63 and 0.75 μm, conducted in a small flow tube apparatus designed and constructed to limit particle growth. These results suggest that the homogeneous nucleation of ice in micrometre- and submicrometre-sized water aerosols should be considered as a surface-based process in climate models.

The various crystal habits formed in our freezing experiments were investigated using an optical microscopy apparatus to image ice particles in the cryogenic flow tube. This apparatus proved to be an effective tool for size and shape analysis when combined with image processing and ray tracing algorithms. A case study conducted at 236 K showed a large tendency for the formation of spherical and irregular habits. Detailed characterization of the crystal habits formed under different sets of atmospheric conditions is highly desirable for the parameterization of climate models, and we have demonstrated the suitability of the microscopy apparatus for measurements conducted in this regard. In addition, particle size determination using an image processing algorithm provided an independent platform for the validation of size distribution retrievals from our aerosol characterization procedure.

Finally, separate studies were performed to determine temperature-dependent complex indices of refraction for crystalline $(NH_4)_2SO_4$ aerosols. The real and imaginary components showed minor variations with temperature down to 223 K, with distinct changes at lower temperatures due to the ferroelectric transition. The differences in the optical constants of paraelectric and ferroelectric $(NH_4)_2SO_4$ are significant enough to distinguish between the phases in laboratory measurements with high signal-to-noise ratios; however, this is not likely to be the case for atmospheric remote sensing studies, where gas-phase interference would obscure the spectral differences.

10.2. Directions for Future Study

The homogeneous nucleation rates determined from the aerosol microphysics model are dependent upon the input volume distributions, flow velocity, temperature profile, and the various microphysical parameters within the model. It is therefore important that each of these factors be carefully determined and/or chosen. In the present study, a value of $\alpha_{ice} = 1$ was chosen for the mass accommodation coefficient of ice, in accordance with previous modelling studies.[17,89,95] Experimental measurements of α_{ice}, however, have shown values as low as 0.001 at temperatures characteristic of the upper troposphere and stratosphere.[105,106] This discrepancy warrants additional minimization runs using lower values of α_{ice}. From Equation 7.14, these lower values will reduce the gas-phase diffusion coefficient, D_v^*, thereby inhibiting diffusion-limited exchange. This could have a profound effect on the homogeneous nucleation rates. While there is currently no consensus as to the "correct" value of α_{ice}, the best value in our studies can be estimated based on the values of χ from our minimization runs.

The present model results from freezing experiments on micrometre- and submicrometre-sized water aerosols indicate a largely surface-based nucleation process. It would be worthwhile to extend this investigation to larger particles, where freezing should be predominantly volume-based. This would be the next step in assessing the relative contributions of volume- and surface-based nucleation as a function of both particle radius and temperature. Such an assessment would be extremely valuable for climate models, providing more accurate determinations of the extent of ice formation given an initial water droplet size distribution and temperature profile.

To provide improved parameterization of crystal habits for climate models, it would be useful to carry out additional imaging studies over a wide range of temperature and humidity conditions, and to determine the relative frequencies of occurrence of different habits for each set of conditions. The image processing algorithm can be used to distinguish between spherical and non-spherical particles, but the further classification of non-spherical particles by visual inspection is time-consuming. A new algorithm, with superior shape recognition, is currently in development in our laboratory, which will streamline the classification process.

A final direction for future study is the determination of temperature-dependent refractive indices of aqueous $(NH_4)_2SO_4$ as a function of solute concentration. These values, combined with those of crystalline $(NH_4)_2SO_4$ and ice determined in the present study (see Appendix A), would permit the determination of composition and size information from freezing experiments on aqueous $(NH_4)_2SO_4$ aerosols when used in our characterization procedure. Modifying the aerosol microphysics model to account for the presence of solute would allow homogeneous ice nucleation rates to be determined from the experimental volume distributions.

APPENDIX A

CRYSTALLINE AMMONIUM SULFATE OPTICAL CONSTANTS

A.1. Introduction

Anthropogenic sulfate aerosols, which include sulfuric acid (H_2SO_4) and ammonium bisulfate and sulfate (NH_4HSO_4 and $(NH_4)_2SO_4$, respectively) are prevalent in the upper troposphere and lower stratosphere, and contribute significantly to the net cooling influence of aerosols.[107-110] In order to improve the accuracy and predictive ability of current atmospheric radiative transfer models, it is essential that the physical and optical properties of these sulfate aerosols be well defined. Complex refractive indices for crystalline $(NH_4)_2SO_4$ have been reported previously by Toon *et al.* at 298 K,[111] but no values have been reported for atmospherically-relevant temperatures. Using the experimental and computational approach applied previously to supercooled water aerosols (Chapter 6), new optical constants were determined for crystalline $(NH_4)_2SO_4$ aerosols at 298, 243, 223, and 213 K. This range of temperatures includes the ferroelectric transition near 223 K, in which the crystal undergoes spontaneous polarization due to changes in the lattice structure. These changes necessarily affect the complex indices of refraction. The details of the temperature-dependent studies have been reported previously in Ref 112.

A.2. Experimental

The experimental apparatus used in these studies is shown in Figure A.1. Aqueous $(NH_4)_2SO_4$ aerosols were generated by atomization of solutions ranging in composition

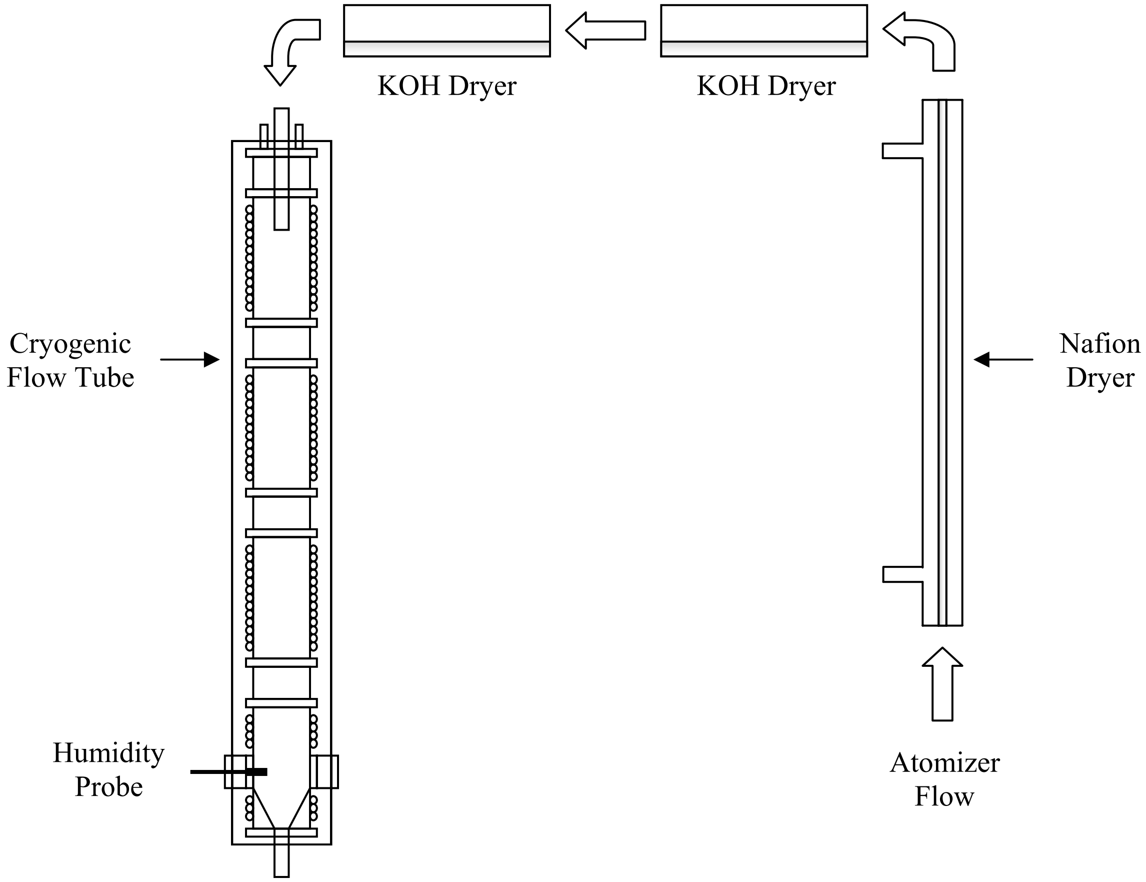

Figure A.1: Schematic diagram of flow tube and drying apparatus used in temperature-dependent studies of $(NH_4)_2SO_4$ optical constants.

from 0.05 to 2 M, prepared from reagent-grade $(NH_4)_2SO_4$ (Sigma-Aldrich Co.) and Millipore®-filtered de-ionized distilled water. The aerosols were dried (effloresced) using the 120 cm long Nafion dryer described in Section 8.2.2 and two beds of hygroscopic KOH pellets. The drying of aqueous solution aerosols of varying concentration was used to generate crystalline $(NH_4)_2SO_4$ aerosols of varying size. The crystalline aerosols were then introduced into the cryogenic flow tube at 3 SLPM, with a dry nitrogen carrier flow of 7 SLPM. All four tube sections were maintained at constant temperature (298, 243, 223, or 213 K). A humidity probe (HM70, Vaisala, Inc.) was placed in the observation section through one of the side ports (orthogonal to FTIR path) used in the optical microscopy setup (Section 9.2.1). The relative humidity in this region was measured to be less than 6%, far below the efflorescence relative humidity of ~ 30%,[15] thus confirming that only crystalline $(NH_4)_2SO_4$ aerosols were present. Extinction spectra were recorded for each solution concentration, and hence, each dry aerosol size, at all experimental temperatures.

The optical constants inversion procedure described in Section 3.9.2 was used to determine the real and imaginary indices of refraction from extinction spectra. T-matrix calculations, employing spheroid aspect ratios between 0.7 and 1.4, were used to generate the basis set spectra. The use of T-matrix theory, rather than Mie theory, for these calculations was based on the fact that crystalline $(NH_4)_2SO_4$ particles are predominantly aspherical, as evidenced by scanning electron microscopy (SEM) observations.[112] Clapp *et al.* have shown previously that Mie calculations for similar small particles (ammonia aerosols) are highly shape-dependent, which can result in the shifting of absorption features in the calculated spectra.[113] Thus, T-matrix calculations are more appropriate for characterizing these aspherical particles.

For experimental extinction spectra recorded at 298, 243, and 223 K, the initial guess values of $k(\tilde{\nu})$ used in the inversion procedure were taken from values obtained in our laboratory at 298 K.[112] For spectra recorded at 213 K – beyond the ferroelectric transition – new initial guess values of $k(\tilde{\nu})$ were determined from a non-scattering spectrum of small particles at 213 K using the approach outlined in Section 3.9.1. The small particles were generated by atomizing and drying a dilute solution of $(NH_4)_2SO_4$ (0.02 M). Irrespective of the initial guess used, an anchor point of $n_\infty = 1.528$ was adopted from the data of Koop in the visible region at 550 nm (~ 18000 cm^{-1}) and room temperature.[114] The resulting optical constants were determined between 590 and 5990 cm^{-1}, with 5 cm^{-1} resolution at 298, 243, and 223 K, and 2 cm^{-1} resolution at 213 K.

A.3. Results and Discussion

The temperature-dependent changes in the crystalline $(NH_4)_2SO_4$ extinction spectra are illustrated in Figure A.2. Gradual changes are observed in the N-H stretching mode, comprising the three overlapping features at 2850, 3062, and 3219 cm^{-1}, and the shoulder at 3300 cm^{-1}. As the temperature is reduced, the peak at 3062 cm^{-1} increases in intensity, while the shoulder at 3300 cm^{-1} becomes sharper and more defined. The ferroelectric transition below 223 K is indicated by changes in the SO_4^{2-} stretching features centred at approximately 1110 cm^{-1} and 975 cm^{-1}, which are shown more clearly in Figure A.3. In the former, two shoulders develop on either side of the central peak, which itself shifts to lower wavenumbers [Figure A.3(a)]. In the latter, a significant increase in intensity is observed, along with a shift to lower wavenumbers [Figure A.3(b)]. The enhancement in the peak at ~ 975 cm^{-1} is believed to arise from distortions of the SO_4^{2-} molecule associated with the ferroelectric transition, as this particular stretching mode is forbidden for perfect tetrahedral geometry.[18,115] These distortions involve changes in the S-O bond lengths and O-S-O bond angles which polarize the SO_4^{2-} molecule; these changes have been previously considered in terms of a transition in the polar structure of SO_4^{2-} from C_S to C_1 symmetry.[116] Overall, the temperature-dependent changes evident in Figures A.2 and A.3 are in accordance with previous literature reports.[17,18]

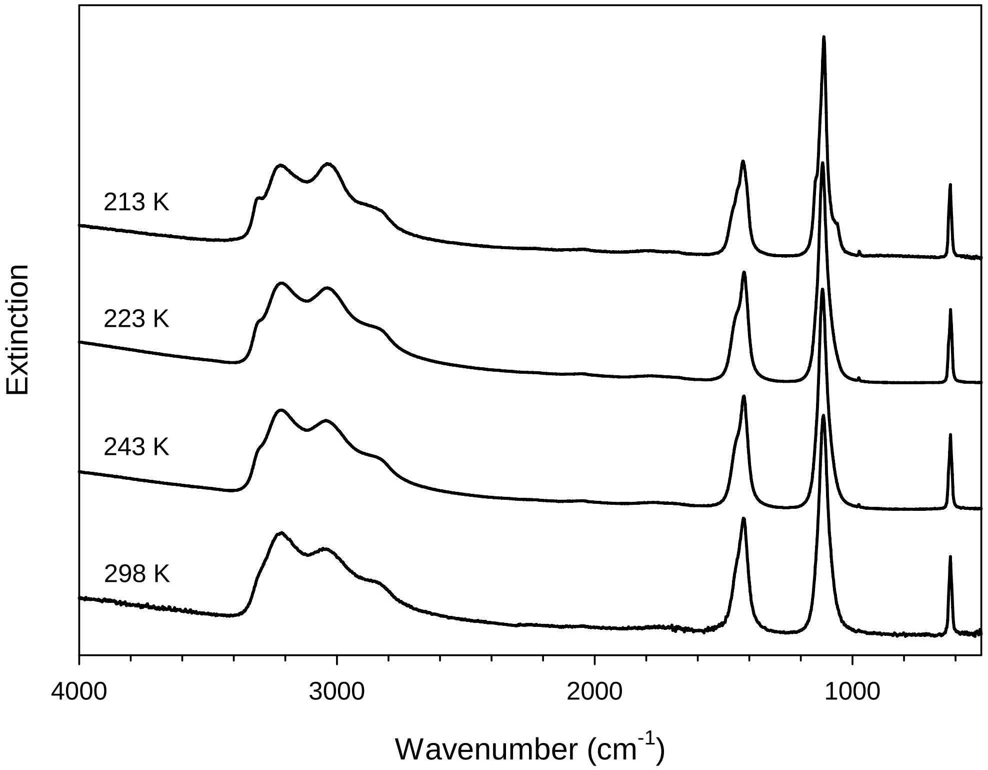

Figure A.2: Changes in extinction spectra of crystalline $(NH_4)_2SO_4$ (from 1 M solution) as a function of temperature. Spectra are scaled and offset for comparison.

The optical constants determined from the inversion procedure for the different dry aerosol sizes were averaged at each experimental temperature. The resulting averaged, temperature-dependent values are plotted in Figure A.4. Only minor changes in both the real and imaginary components are observed as the temperature is reduced to 223 K, with significant changes observed at 213 K due to the ferroelectric transition. Based on these changes, the new values for the ferroelectric phase should be employed in data retrievals from remote sensing and laboratory studies performed below 223 K. Figure A.5 shows calculated fits to an extinction spectrum measured at 213 K using the optical constants obtained at 298 and 213 K. The improved fit obtained using the 213 K

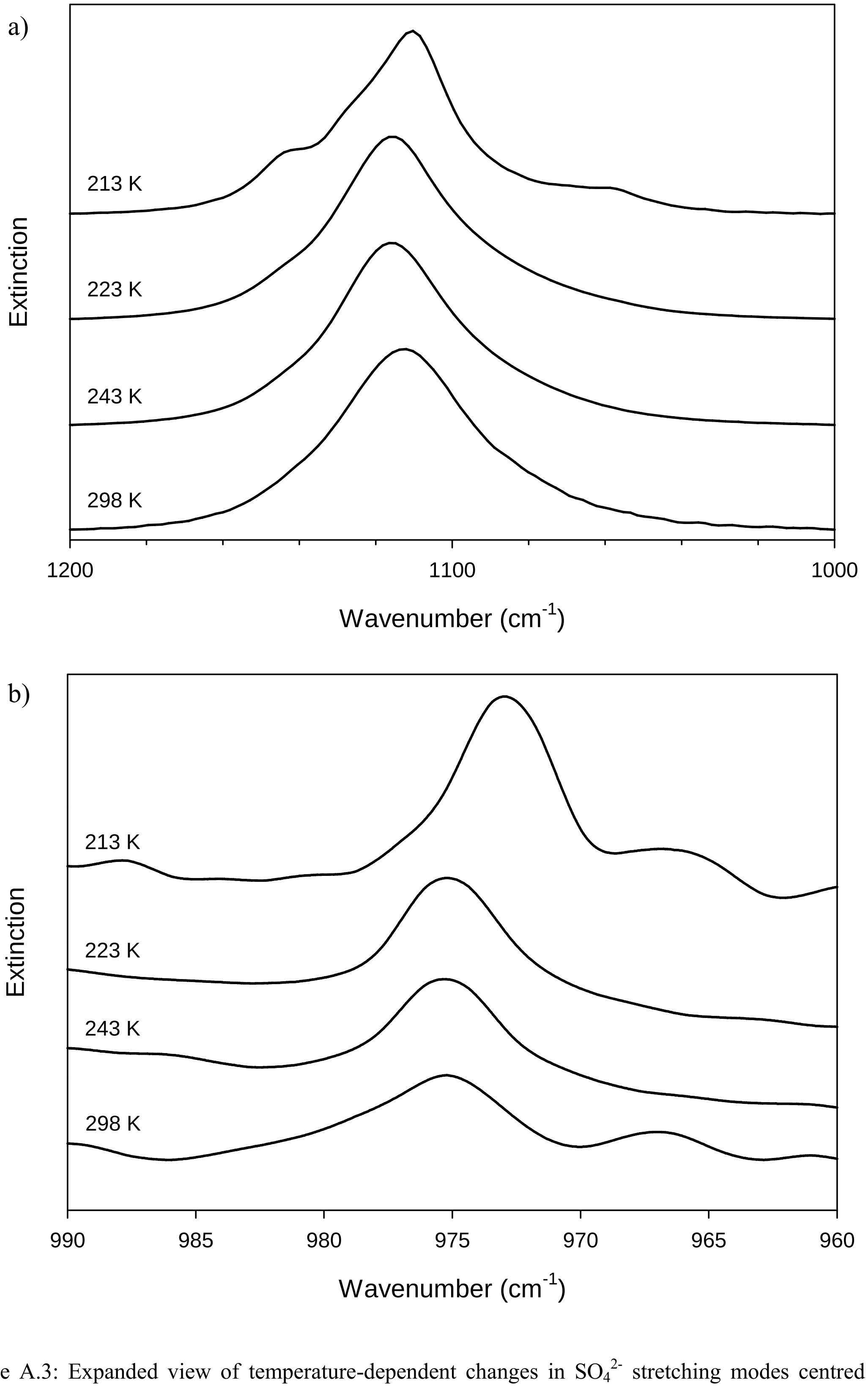

Figure A.3: Expanded view of temperature-dependent changes in SO_4^{2-} stretching modes centred at (a) 1110 cm^{-1} and (b) 975 cm^{-1} from spectra in Figure A.2.

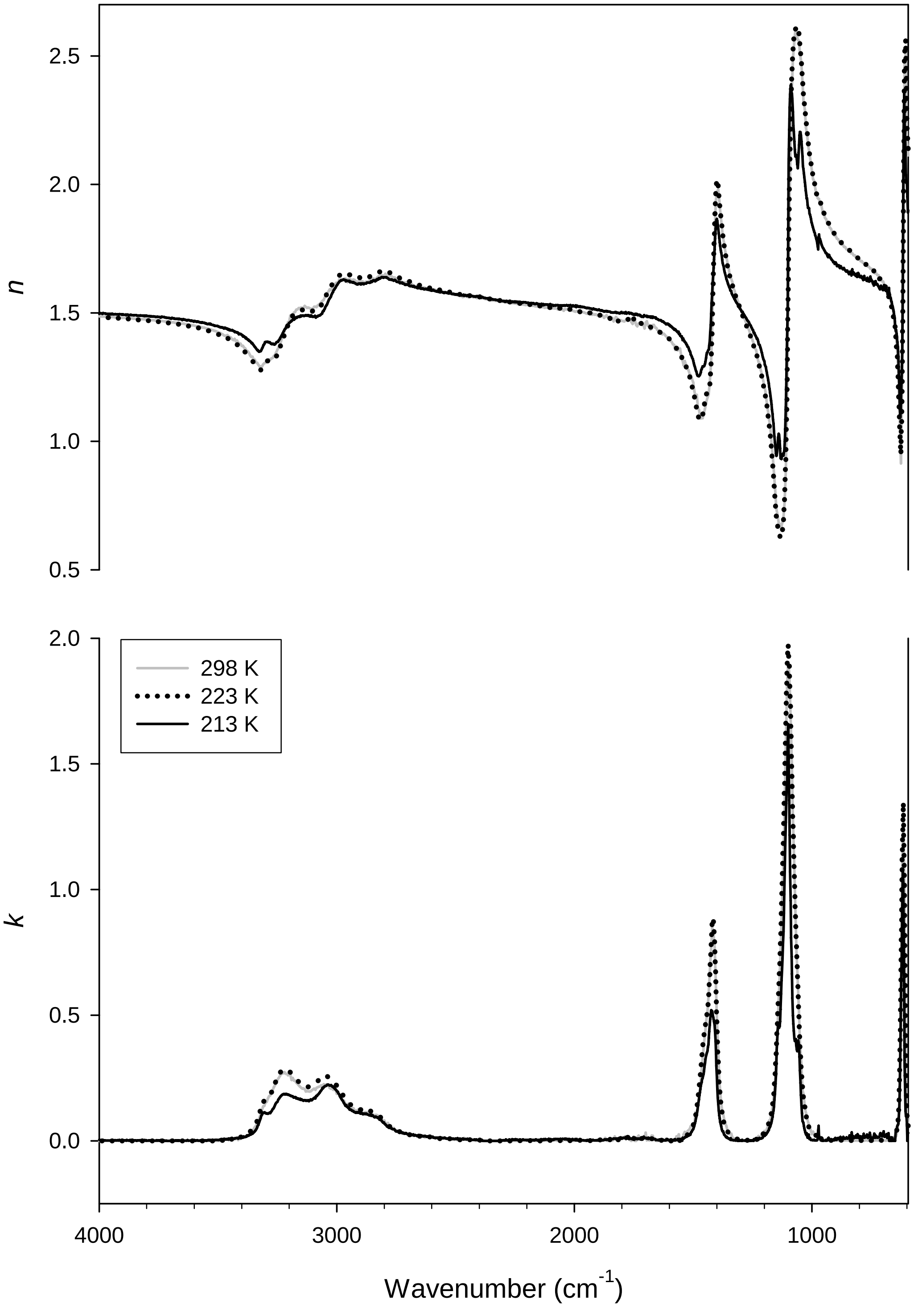

Figure A.4: Averaged temperature-dependent complex indices of refraction of crystalline $(NH_4)_2SO_4$ determined from inversion procedure.

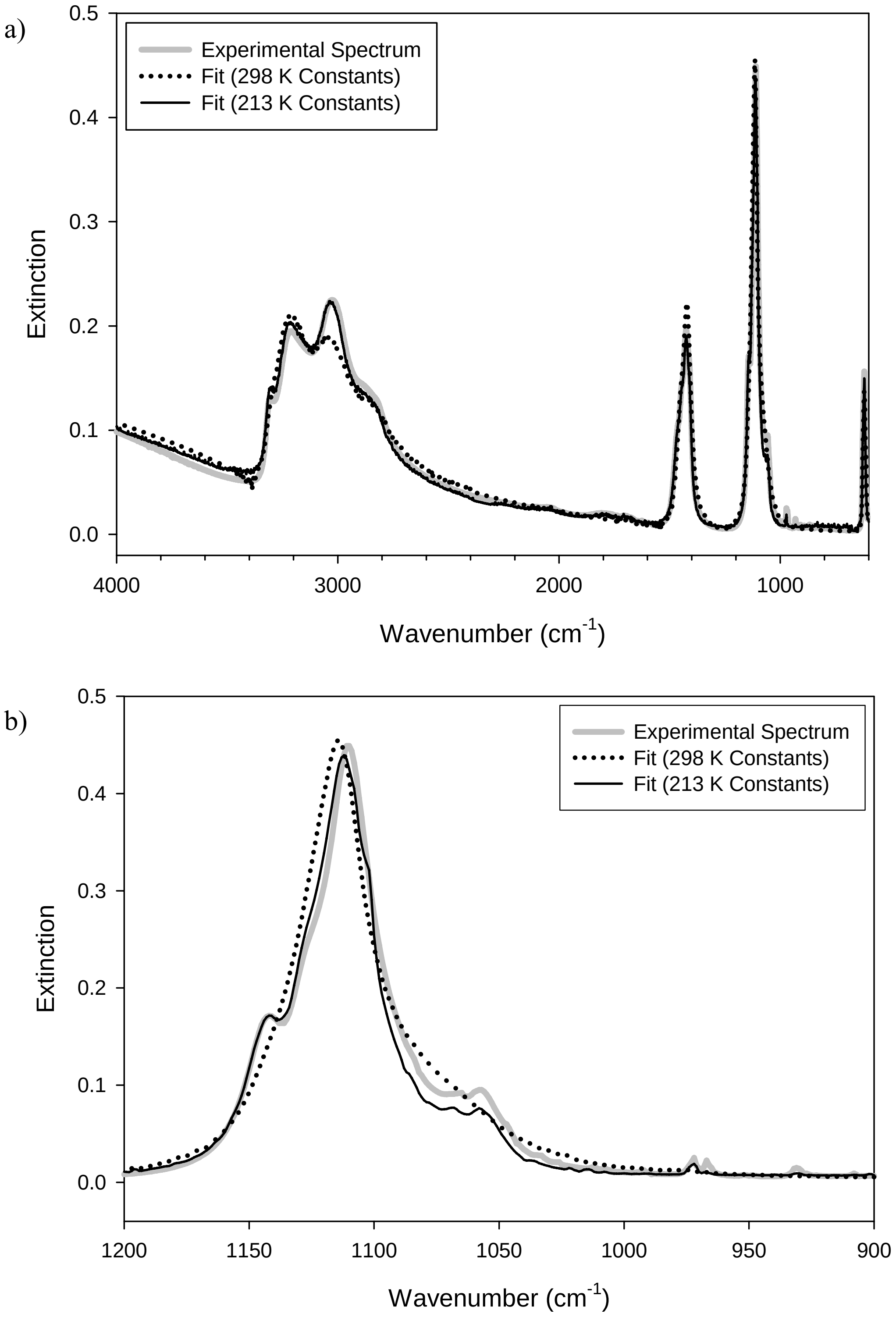

Figure A.5: (a) Calculated fits to an extinction spectrum of crystalline $(NH_4)_2SO_4$ (from 2.1 M solution) at 213 K using optical constants obtained at 298 and 213 K and (b) expanded view of SO_4^{2-} feature subject to greatest change from the ferroelectric transition.

values is clearly evident in the N-H stretching region around 3000 cm^{-1} [Figure A.5(a)], and in the SO_4^{2-} stretching region around 1100 cm^{-1} [Figure A.5(b)], which undergoes the most change following the ferroelectric transition.

The uncertainties in the averaged values of $n(\tilde{\nu})$ and $k(\tilde{\nu})$ were estimated at each temperature using the statistical approach introduced in Section 6.3.1. At room temperature, errors in $n(\tilde{\nu})$ and $k(\tilde{\nu})$ are typically 6% or smaller. As the temperature is reduced to 243 and 223 K, errors in $n(\tilde{\nu})$ are less than 4%, while those in $k(\tilde{\nu})$ are below 5%. This decrease in uncertainty can be attributed to increased extinction intensity in spectra at lower temperatures (minimal evaporative losses), as well as reduced spectral interference from gas-phase absorption (water vapour condensation on aerosols, tube walls, and fins). Contrary to this reasoning, errors in $n(\tilde{\nu})$ and $k(\tilde{\nu})$ at 213 K are typically within 6% and 8%, respectively. We attribute the increased error in this case to the low extinction intensity in the small particle spectrum used to derive the initial guess optical constants at this temperature.

APPENDIX B

AEROSOL MICROPHYSICS MODEL

B.1. Introduction

The aerosol microphysics model has been implemented in Matlab (The Mathworks, Inc.), and consists of separate microphysics and minimization components, as described in Chapter 7. The Matlab code is divided into main routines, which follow the logic flow shown in Figure 7.1, and several subroutines, which calculate the conditions and parameters required by the main routines. This appendix provides each of the constituent routines, along with brief descriptions of their function.

B.2. Main Model Routines

1) master_nP1.m: Initial guess values for the minimization parameters ΔH_{act} and ΔS_{act}, surface and/or volume dependence, and mass accommodation coefficients are set, as are the input files describing the experimental supercooled water and/or ice distributions to be studied. The *fminsearch* minimizer from the Matlab library is called to vary ΔH_{act} and ΔS_{act} in the minimization component.

```
nP = 1;       % number of computer processors

initial_run = false;
global flow;
flow.volume_freezing = true;    % activate volume freezing
flow.surface_freezing = false;  % activate surface freezing
flow.composite_chi = true;      % use both ice and water distributions
%to evaluate Chi
flow.sumAdi = false;            % ice = ice + water
flow.nTprofs = 1;               % number of temperature profiles
save 'flow.mat' flow;

input_files = char(textread('input_files.txt','%s'));
save 'input_files.mat' input_files;
```

```
act_params = [G.dHv G.dSv G.dHs G.dSs];

global massaccom;
massaccom.water = 0.5; % Taken fom the journal of physical chemistry
%Vol 105, Number 47, pg 10627 2001. (Davidovits)
massaccom.ice = 1;

G.dHv = act_params(1);
G.dSv = act_params(2);
G.dHs = act_params(3);
G.dSs = act_params(4);

if flow.surface_freezing & flow.volume_freezing
    params = [G.dHv G.dSv G.dHs G.dSs];
end;

if ~flow.surface_freezing & flow.volume_freezing
    params = [G.dHv G.dSv];
end;

if flow.surface_freezing & ~flow.volume_freezing
    params = [G.dHs G.dSs];
end;

options=optimset('Display','iter');
[xmin,value] = fminsearch('ftm_minimizer_p_nP1',params,options,nP)

%%%%%%%%%%%%%%%%%%%%%%%%%%%%%%%%%%%%%%%%%%%%%%%%%%%%%%%%%%%%%%%%%%

save 'master.mat';
save('runOver.txt')
```

2) ftm_minimizer_nP1.m: Compares total χ values from subsequent runs to determine whether or not a minimum difference between calculated and experimental supercooled water and/or ice distributions has been achieved.

```
function chi = ftm_minimizer_p_nP1(params,nP);

save('params.txt','params','-ascii')

load 'input_files.mat';

n_over = true;
not_over = true;
c = 1;

while n_over

    while not_over
```

```
        for i = 1:nP

            f = dir(horzcat(num2str(i),'.inp'));

            if size(f,1) == 0

                save(horzcat(num2str(i),'.inp'));
                fid = fopen(horzcat(num2str(i),'.inp'),'wt');
                input_file = fprintf(fid,'%s',input_files(c,:));
                fclose(fid);
                model_engine_nP1(1)
                c = c + 1;

                if  c > size(input_files,1)

                    not_over = false;

                    break
                end

            end

        end



    end

    x = dir('Chi2.out');    % new

    if size(x,1) ~= 0   % new

        chi = load('Chi2.out');

        if size(chi,1) == size(input_files,1)
            sprintf('*** Average chi is: %f ***',mean(chi))
%             chi = sum(chi);
            chi = mean(chi);
            n_over = false;
            delete('Chi2.out');
        end
    end % new

end

return
```

3) model_engine_nP1.m: Reads input files and prepares volume distributions of supercooled water and ice, as well as the axial temperature profile in flow tube.

```
function pp = model_engine_nP1(id)

global input_file;
not_over = true;

%while not_over

    endIt = dir('runOver.txt');

    if size(endIt,1) ~= 0

        not_over = false;

    end

    a = dir(horzcat(num2str(id),'.inp'));

if (size(a,1) ~= 0)

        fid = fopen(horzcat(num2str(id),'.inp'));
        input_file = fscanf(fid,'%s');
        fclose(fid);
        delete(horzcat(num2str(id),'.inp'));

%========== Global variables ================================
        global a_D_j;   %   r, N(r), V(r) - experimental data for
%original water aerosol
        global a_D_i;   %   r, N(r), V(r) - experimental data for
%resulting water/ice aerosol
        global a_R;     %   r water & ice (um)
        global a_R_i;
        global a_R_3;
        global a_R_2;
        global v1_j;
        global v1_i;
        global a_N_j;   %   N(r) water
        global a_V_j;   %   V(r) water
        global a_N_i;   %   N(r) ice
        global a_V_i;   %   V(r) ice
        global a_times; %   a_times(time,p(H2O),T, x(ice)) array to
%keep snapshots of few variables in time
        global nm_cond;
        global bin_multiplier;
        global f_handle;
        global t_profile;
        global t_profileC;
        global t_profileA;
        global counter
        global delta_N;
        global run_type;
        global endTime;
        global presentation;
        global r_time;
        global n_sections;
```

```
        % structures used to exchange input/output variables with
%solver function
        global flow;
        global solver;
        global constant;
        global input;
        global output;
        global t_low;
        global t_high;
        global plot_func;

        load 'flow.mat';

        %========== Input files ===================================
        use_inputfile = true;
        bin_multiplier = 1;
        workfolder = 'runs/';
        %%%%%%%%%%%%%%%%%%%%%%%%%%%%%%%%%%%%%%%%%%%%%%%%%
        run_type = 'compare_run';
        flow.transformed_values = true;
        %%%%%%%%%%%%%%%%%%%%%%%%%%%%%%%%%%%%%%%%%%%%%%%%%

        %========Initialize =======================================

        xx = 0;
        g = 20; %cut off first few bins in output calc.

        solver.d_time=0.001;         % time increment for calculation
        solver.ftm_solver_x2 = false;

        flow.mass_transfer = true;      % activate mass transfer
%between drops
        flow.integral_freezing = false; % activate integral formula
%rather than differential equation for freezing
        flow.heat_effects = false;      % activate heat
%release/consumption during condensation/evaporation of drops
        flow.Kelvin_effect = true;      % activate Kelvin effect
        flow.density = true;            % activate density
        semilogx_plot = false;          % use logarithmic scale for
%radii
        r_time_T_corr = true;           % correction of residence time
%due to change of temperature

        solver.n_points = 50;           % number of p_inf etc to store
        solver.min_T_step = 0.05;       % temperature change causing
%recalculation of T dependent functions

        input.n_radii = 96;             % number of r (usually 96, from
%0.05 to 11.89 um)
        input.n_radii_133 = 133;        % number of ice radii (0.05 to
%100 um)

        input.r_ref = 2.0;              % reference radius (um) for
%calculation of J_T_s
        input.Jv_coeff = 1.0;           % coefficient for Jv
```

```
        input.Js_coeff = 1.0;           % coefficient for Js

        %===========Read in input file=================================
        format('long');
        format('compact');


%        if use_inputfile
input_file
[var_type x] = textread(horzcat(workfolder,input_file),'%s%s');

            f_D_j= horzcat(workfolder,cell2mat(x(1)));
            index_j = str2num((cell2mat(x(2))));
            window_j = str2num((cell2mat(x(3))));
            f_D_i= horzcat(workfolder,cell2mat(x(4)));
            index_i = str2num((cell2mat(x(5))));
            window_i = str2num((cell2mat(x(6))));
            r_time = str2double(cell2mat(x(8)));
            n_sections = str2double(cell2mat(x(9)));
            t_low = str2double(cell2mat(x(10)))+xx;
            t_high = str2double(cell2mat(x(11)));
%        end

        clear input_file;

        input.flow_rate = 10.0;    % flow rate, SLPM
        section_tau = 17.73;       % Section residence time
        pTorr = 730.0;             % pressure of experiment, Torr
        input.p = pTorr/760.0*1.01325e5;  % pressure of experiment, Pa

        params =load('params.txt');

        if flow.surface_freezing & flow.volume_freezing
            G.dHv = params(1);
            G.dSv = params(2);
            G.dHs = params(3);
            G.dSs = params(4);
        end;

        if ~flow.surface_freezing & flow.volume_freezing
            G.dHv = params(1);
            G.dSv = params(2);
            G.dHs = 1;
            G.dSs = 1;
        end;

        if flow.surface_freezing & ~flow.volume_freezing
            G.dHv = 1;
            G.dSv = 1;
            G.dHs = params(1);
            G.dSs = params(2);
        end;

        load -mat workspaces/4layermapMedS.mat theta;
        thetas = theta;
```

```
        load -mat workspaces/4layermapMedS.mat intercept;
        intercepts = intercept;
        load -mat workspaces/4layermapMedV.mat theta;
        thetav = theta;
        load -mat workspaces/4layermapMedV.mat intercept;
        interceptv = intercept;

        G =
coordtransform3(G,thetav,thetas,interceptv,intercepts,'decode');

        %========== Constants =========================================
        input.T_low = 273.15 + t_low;  % temperature of experiment, K
        input.T_high = 273.15 + t_high;% temperature of conditioning, K

        if n_sections == .56
            sections = 'abc-d';
        elseif n_sections == 1.56
            sections = 'ab-cd';
        elseif n_sections == 2.56
            sections = 'a-bcd';
        elseif n_sections == 3.56
        sections = 'abcd';
        elseif n_sections == 1.06         % added for small flow tube
            sections = 'a-b';
        else
            sections = '';
        end

        if strcmp(sections,'')
            f_handle = 'temperature1';
        elseif strcmp(sections,'abcd')
            % exponential decay from input.T_high to input.T_low
            f_handle = 'temperature3';
        else
            f_handle = 'temperature2';
            t_profile =
temperatureProfile(sections,input.T_low,solver.d_time*10,1);
        end

        temperature = str2func(f_handle);

        constant.Na = 6.0221e23;
        constant.Mw = 18.0e-3;    % molecular weight of water, kg mol-1
        constant.R = 8.31;       % universal gas constant, J mol-1 K-1
        ro_j = 1.0;            % density of liquid water, g cm-3
        ro_i = 1.0;            % density of water ice, g cm-3

        %========== Read and initialize data ==========================
        if t_high - t_low < 0.5
        end;

        %======Residence time calculation and temperature correction===

        if n_sections == 1.56
            r_time = tCorr(n_sections,section_tau);
```

```
        elseif n_sections == 3.56
            r_time = n_sections*section_tau*298/245; % 63.11s * 298/245
%= 76.77s
        end

        a_D_j = makea_D_j(f_D_j,index_j,window_j);
        a_D_i = makea_D_i(f_D_i,index_i,window_i);
        a_D_j = scale(a_D_i,a_D_j);

%============== Load experimental distributions =======================
        output.T_start = feval(temperature,0,t_profile);
        output.T_end = feval(temperature,r_time,t_profile);
        T = output.T_start;
        output.p_inf_start = p_sat(output.T_start,'water');
        input.t_interval=r_time/solver.n_points;
        a_times=zeros(round(r_time)-1,5);

        v1_j = 1e15*constant.Mw/(ro_j*constant.Na);
        v1_i = 1e15*constant.Mw/(ro_i*constant.Na);

        p_inf = output.p_inf_start;
        N1 = p_inf*constant.Na/(constant.R*T)*1e-6;

        %==== Choose runtype mode=====================================

        mode = 'time';
        %mode = 'fraction';
        if strcmp(mode,'time')
            amount = r_time;
        elseif strcmp(mode,'fraction')
            amount = [r_time .98];
        end

        %==== Run Solver =============================================

        [res,Y] = ftm_solver_ol_nP1(mode,amount,true,G,t_profile);

        %========== Run plotting routines ============================

        save('Chi2.out','res','-append','-ascii')

    end
return
```

4) ftm_solver_ol_nP1.m: Solves differential equations for homogeneous nucleation and diffusion-limited exchange processes using the *ode15s* solver from the Matlab library. Final (calculated) supercooled water and/or ice distributions are output.

```
function [res,Y] =
ftm_solver_ol_nP1(mode,amount,show_timing,G,t_profile);

% Input arguments - mode - either 'time' or 'fraction
%                   amount - designates endtime or fraction of ice
%                            desired
%                   show_timing - toggles timing on and off
%                   G - Structure containing delta H and delta S
%
% Output arguments - res - return either runtime length, or fraction
%                     frozen.

global input_file;  %name of current input file
global a_D_i;       % r, N(r), V(r) - experimental data for ice
%distribution
global a_R;         % r water & ice (um)
global a_R_i;
global a_R_2;       % r^2 water and ice (um^2)
global a_R_i2;       % r^2 water and ice (um^2)
global a_R_3;       % r^3 water and ice (um^3)
global a_R_i3;       % r^3 water and ice (um^3)
global a_N_j;       % N(r) water
global a_V_j;       % V(r) water
global a_N_i;       % N(r) ice
global a_V_i;       % V(r) ice
global a_times;     % a_times(time,p(H2O),T, x(ice)) array to keep
%snapshots of few variables in time
global nm_cond;     % net_mass_condensation
global t_low;       % temperature of experiment, C
global t_high;      % temperature of the previous section
global f_handle;    % name of temperature function to be used
global delta_N      % Change in pressure (in molecules/cm^3)
global run_type;    % designates a direct, compare or inverse run
global counter;     % allows user to keep track of variables of
%interest
global bin_multiplier; % multiplies number of bins original used (96)
%by bin_multiplier
global r_time;
global n_sections;

global flow;
global solver;
global constant;
global input;
global output;
global scaling_values;   % keep track of all scaling factors
global massaccom;        % mass accommodation coefficients

s = resize(50,run_type);
scaling_values(2) = s; % inter- and extrapolation of size distributions
%while extending size range may change total volume: scale back

% Initialize temperature variables

temperature = str2func(f_handle);
T = feval(temperature,0,t_profile);
```

```
% Unbundle constants

p = input.p;
R = constant.R;
Mw = constant.Mw;
Na = constant.Na;

%%%%%%%%%%%%%%%%%%%%%%%%%%%%%%
if flow.density
    ro_j = ro((input.T_high+input.T_low)/2,'water');
    ro_i = ro((input.T_high+input.T_low)/2,'ice');
else
    ro_j = 1;
    ro_i = 1;
end
a_R_i = a_R*(ro_j/ro_i)^(1/3);
rho = [ro_j ro_i];

a_R_i2 = a_R_i.^2; % Calculating a_R^2 and a_R^3 saves processing time
a_R_i3 = a_R_i.^3;

% Calculating vapour pressure using surface fraction

Si=sum(a_R_i2.*a_N_i(:),1);
Sj=sum(a_R_2.*a_N_j(:),1);
output.p_inf_start = Sj/(Si+Sj)*p_sat(T,'water') +
Si/(Si+Sj)*p_sat(T,'ice');
p_inf = output.p_inf_start;
N1 = p_inf*Na/(R*T)*1e-6;


%%%%%%%%%%%%%%%%%%%% Calculation Starts %%%%%%%%%%%%%%%%%%%%%%

if flow.density
    ro_j = ro((input.T_high+input.T_low)/2,'water');
    ro_i = ro((input.T_high+input.T_low)/2,'ice');
else
    ro_j = 1;
    ro_i = 1;
end

rho = [ro_j ro_i]
counter = 1;
steps = 3;
step = amount(1)/steps;

dateStart = sprintf('%s\n%s\n%s\n','- Start ---------------------------
-------------------',...
    datestr(now),...
    '------------------------------------------------------')
sprintf('Now starting ode15s for file: %s',input_file)

 [T, Y] =
ode15s(@deteade_N1lost,[0:step:amount(1)],vertcat(a_N_j,a_N_i,0,0,0,N1)
,[],G,rho,t_profile);  % N1lost added to deteade.m
m = size(Y); % Determine dimension of solution matrix
n = m(2)-4; % N1lost added to deteade.m and Niv and Nis
```

```
o = n/2;

%-----------------------------
logfile = horzcat('log_',input_file);
logfile = regexprep(logfile, '/', '_');
logfile = regexprep(logfile, '\', '_');
logf = fopen(logfile,'wt');        % for printing to logfile

% print information pertinant to run

fprintf(logf,'# Input file:
%s\n#\n######################################################\n',input_
file)

fprintf(logf,'# n_sections = %f,\tr_time = %f\n',n_sections,r_time);
sprintf('n_sections = %f,\tr_time = %f\n',n_sections,r_time)

fprintf(logf,'# At start T = %5.2f K,\tp_inf = %6.3f Pa,\tN1 = %5.3e
cm-3\n',input.T_high,p_inf,N1);
sprintf('At start T = %5.2f K,\tp_inf = %6.3f Pa,\tN1 = %5.3e cm-
3\n',input.T_high,p_inf,N1)

params =load('params.txt'); %MAT
if flow.volume_freezing & ~flow.surface_freezing
    fprintf(logf,'# params (transformed):\t%g
%g\n',params(1),params(2));
    sprintf('params (transformed):\t%g %g',params(1),params(2))
    fprintf(logf,'# T:%5.2f K (t:%5.2f^C; dHv:%13.10f kJ mol-1;
dSv:%13.10f kJ mol-1 K-1; Jv:%5.3e cm-3 s-1\n',...

input.T_low,t_low,G.dHv/1000,G.dSv/1000,Jv_Gibbs(input.T_low,G));
    sprintf('T:%5.2f K (t:%5.2f^C; dHv:%13.10f kJ mol-1; dSv:%13.10f kJ
mol-1 K-1; Jv:%5.3e cm-3 s-1',...

input.T_low,t_low,G.dHv/1000,G.dSv/1000,Jv_Gibbs(input.T_low,G))
elseif flow.surface_freezing & ~flow.volume_freezing
    fprintf(logf,'# params (transformed):\t%g
%g\n',params(1),params(2));
    sprintf('params (transformed):\t%g %g',params(1),params(2))
    fprintf(logf,'# T:%5.2f K (t:%5.2f^C; dHs:%13.10f kJ mol-1;
dSs:%13.10f kJ mol-1 K-1; Js:%5.3e cm-2 s-1\n',...

input.T_low,t_low,G.dHs/1000,G.dSs/1000,Js_Gibbs(input.T_low,G));
    sprintf('T:%5.2f K (t:%5.2f^C); dHs:%13.10f kJ mol-1; dSs:%13.10f
kJ mol-1 K-1; Js:%5.3e cm-2 s-1',...

input.T_low,t_low,G.dHs/1000,G.dSs/1000,Js_Gibbs(input.T_low,G))
elseif flow.volume_freezing & flow.surface_freezing
    fprintf(logf,'# params (transformed):\t%g %g %g
%g\n',params(1),params(2),params(3),params(4));
    sprintf('params (transformed):\t%g %g %g
%g',params(1),params(2),params(3),params(4))
    fprintf(logf,'# T:%5.2f K; dHv:%13.10f kJ mol-1; dSv:%13.10f kJ
mol-1 K-1; Jv:%5.3e cm-3 s-1\n# t:%5.2f^C; dHs:%13.10f kJ mol-1;
dSs:%13.10f kJ mol-1 K-1; Js:%5.3e cm-2 s-1\n',...
        input.T_low,G.dHv/1000,G.dSv/1000,Jv_Gibbs(input.T_low,G),...
        t_low,G.dHs/1000,G.dSs/1000,Js_Gibbs(input.T_low,G));
```

```
    sprintf('T:%5.2f K; dHv:%13.10f kJ mol-1; dSv:%13.10f kJ mol-1 K-1;
Jv:%5.3e cm-3 s-1\nt:%5.2f^C; dHs:%13.10f kJ mol-1; dSs:%13.10f kJ mol-
1 K-1; Js:%5.3e cm-2 s-1',...
        input.T_low,G.dHv/1000,G.dSv/1000,Jv_Gibbs(input.T_low,G),...
        t_low,G.dHs/1000,G.dSs/1000,Js_Gibbs(input.T_low,G))
end % if flow.volume_freezing & ~flow.surface_freezing

% Unbundle solution matrix

a_N_j = Y(m(1),1:o)';
a_N_i = Y(m(1),o+1:n)';
a_N_j_evol = Y(:,1:o)';
a_N_i_evol = Y(:,o+1:n)';

a_V_i(:) = (a_N_i.*(a_R_i.^3*4/3*pi))';
a_V_j(:) = (a_N_j.*(a_R_3*4/3*pi))';

N1f = Y(m(1),m(2));
N1lost = Y(m(1),m(2)-1)  % N1lost added to deteade.m
% and Niv and Nis
Niv =  Y(m(1),m(2)-3);
Nis =  Y(m(1),m(2)-2);
Njtotal = sum(a_N_j_evol(:,1)); % total number concentration of water
%droplets at START
%the above two variables have to be scaled later
N1evol = Y(:,m(2));
%T is time, Tevol is evolution of temperature
for ii = 1:m(1)
Tevol(ii,1) = feval(temperature,T(ii),t_profile);
p_sat_w_evol(ii,1) = p_sat(Tevol(ii,1),'water');
p_sat_i_evol(ii,1) = p_sat(Tevol(ii,1),'ice');
end
p_inf_evol = (N1evol*1e6/Na)*R.*Tevol;

% finally scale calculated resulting water and ice volumes to match
% total of experimental water and ice volume: scale up by about 1.1
% (10%), losses haven't been accounted for when mass balance scaling
% was applied
scaling =
(sum(a_D_i(:,3))*ro_j+sum(a_D_i(:,5))*ro_i)/(sum(a_V_i)*ro_i+sum(a_V_j)
*ro_j)
scaling_values(3) = scaling;
a_V_i = a_V_i.*scaling;
a_V_j = a_V_j.*scaling;
a_N_i(:) = (a_V_i./(a_R_i.^3*4/3*pi))';
a_N_j(:) = (a_V_j./(a_R_3*4/3*pi))';
a_N_j_evol = a_N_j_evol.*scaling;
a_N_i_evol = a_N_i_evol.*scaling;

Njtotal = sum(a_N_j_evol(:,1)); % total number concentration of water
%droplets at START
Niv =  Niv.*scaling;
Nis =  Nis.*scaling;

delta_N = N1 - N1f;

    if flow.density
```

```
        ro_j = ro(output.T_end,'water');
        ro_i = ro(output.T_end,'ice');
    else
        ro_j = 1;
        ro_i = 1;
    end

% Calculate values important for plotting
% mass fraction frozen
ice_fraction =
sum(a_V_i(:))*ro_i/(sum(a_V_j(:))*ro_j+sum(a_V_i(:))*ro_i+1e-10)
% volume fraction frozen
ice_fraction = sum(a_V_i(:))/(sum(a_V_j(:))+sum(a_V_i(:))+1e-10)

temp = feval(temperature,amount(1),t_profile);
output.T_end = temp;
p_inf = N1f/constant.Na*(constant.R*temp)*1e6;
output.p_inf_end = p_inf;

if   strcmp(mode,'time')
    res = ice_fraction;
elseif strcmp(mode,'fraction')
    res = current_time - tau;
end;

%=====Print Results on Prompt====================

chi1 = ((a_D_i(1:input.n_radii,3) -
a_V_j(1:input.n_radii))/(1+sum(a_D_i(1:input.n_radii,3))+sum(a_D_i(1:in
put.n_radii,5)))*input.n_radii).^2; %Final water
chi2 = ((a_D_i(1:input.n_radii,5) -
a_V_i(1:input.n_radii))/(1+sum(a_D_i(1:input.n_radii,3))+sum(a_D_i(1:in
put.n_radii,5)))*input.n_radii).^2; %Final ice

fprintf(logf,'# Mass balance scaling of water Start distribution
(losses not accounted for): %f\n',scaling_values(1));
massaccom
fprintf(logf,'# Mass accomodation coefficients: water = %f\t ice =
%f\n',massaccom.water,massaccom.ice);
fprintf(logf,'# Scale volume of water Start distr. back after distr.
extrap. (should be close to 1): %f\n',scaling_values(2));

dateEnd = fprintf(logf,'%s\n# Results: %s\n%s\n','#---------------------
---------------------------------',...
    datestr(now),...
    '#-----------------------------------------------------');
dateEnd = sprintf('%s\n%s\n%s\n','- End --------------------------------
-----------------',...
    datestr(now),...
    '------------------------------------------------------')

fprintf(logf,'# Scaled calculated distributions to match total
experimental volume of water and ice: %f\n',scaling_values(3));
fprintf(logf,'# Volume fraction frozen of ice: %f\n',ice_fraction);
fprintf(logf,'# N.conc.waterSTART: %8.0f;\t nucleated by V (fraction)
and S: %8.0f (%.3f)\t%8.0f\n',Njtotal,Niv,Niv/(Niv+Nis),Nis);
```

```
%========== Run plotting routines =====================================

        res = sum(chi2);
        fprintf(logf,'# chi2: %f\n',res);
        sprintf('chi2: %f\n',res)
        if flow.composite_chi
            res = res + sum(chi1);
            fprintf(logf,'# chi1+chi2: %f\n',res);
            sprintf('chi1+chi2: %f\n',res)
        end

      fprintf(logf,'# Solution in %i timesteps:\n',steps);
      fprintf(logf,'# Col1:radius(water/ice), Col2:Nwater/ice,exper-
end, Col3-%i:Nwater/ice\n# Water\n',3+steps);
fclose(logf); % close logfile

% experimental size distribution at End, extended size range (with
zeros)
aDi_water = vertcat(a_D_i(:,2), zeros(input.n_radii_133-
input.n_radii,1));
aDi_ice = vertcat(a_D_i(:,4), zeros(input.n_radii_133-
input.n_radii,1));

%save solution for water
Y = [a_R aDi_water a_N_j_evol];
save(logfile,'Y','-append','-ascii')

% blank line
logf = fopen(logfile,'at');        % for printing to logfile
fprintf(logf,'\n# Ice\n');
fclose(logf); % close logfile

%save solution for ice
Y = [a_R_i aDi_ice a_N_i_evol];
save(logfile,'Y','-append','-ascii')

% blank line
logf = fopen(logfile,'at');        % for printing to logfile
%%fprintf(logf,'\n# Evolution of important variables\n# time/s p_inf/Pa
T/degC ice_mass_fract freeze_rate_V/cm-3s-1 freeze_rate_S/cm-3s-1 S_wat
S_ice total_N_j total_N_i total_V_j total_V_i\n');
fprintf(logf,'\n# Evolution of important variables\n# time/s p_inf/Pa
T/degC ice_mass_fract freeze_rate_V/cm-3s-1 freeze_rate_S/cm-3s-1 S_wat
S_ice total_N_j total_N_i total_V_j total_V_i N1lost(wall_losses)
number_fraction_frozen\n'); % N1lost added to deteade.m
fclose(logf); % close logfile

save(logfile,'a_times','-append','-ascii')

% blank line and JV and or JS
logf = fopen(logfile,'at');        % for printing to logfile
fprintf(logf,'\n# Jv and/or Js at T_low and 0.5 K higher:\n#
T[K]\tJv[cm-3s-1]\tJs[cm-2s-1]\n');

if flow.volume_freezing & ~flow.surface_freezing

fprintf(logf,'%5.2f\t%5.3e\t.\n',input.T_low,Jv_Gibbs(input.T_low,G));
```

```
fprintf(logf,'%5.2f\t%5.3e\t.\n',input.T_low+0.5,Jv_Gibbs(input.T_low+0
.5,G));
elseif flow.surface_freezing & ~flow.volume_freezing

fprintf(logf,'%5.2f\t.\t%5.3e\n',input.T_low,Js_Gibbs(input.T_low,G));

fprintf(logf,'%5.2f\t.\t%5.3e\n',input.T_low+0.5,Js_Gibbs(input.T_low+0
.5,G));
elseif flow.volume_freezing & flow.surface_freezing

fprintf(logf,'%5.2f\t%5.3e\t%5.3e\n',input.T_low,Jv_Gibbs(input.T_low,G
),Js_Gibbs(input.T_low,G));

fprintf(logf,'%5.2f\t%5.3e\t%5.3e\n',input.T_low+0.5,Jv_Gibbs(input.T_l
ow+0.5,G),Js_Gibbs(input.T_low+0.5,G));
end
fclose(logf); % close logfile

return;
```

5) deteade_n1lost.m: Calculates and assembles the differential equations for homogeneous nucleation and diffusion-limited exchange processes that are passed to the *ode15s* solver.

```
function deriv = deteade_N1lost(t,a_N_j_a_N_i_N1,G,rho,t_profile)

% Input arguments - t - current time (independent variable)
%                   a_N_j_a_N_i_N1 - the vertically concatenated array
%                     of a_N_j, a_N_i, and N1 (the number of molecules
%                     relating to far field pressure)
%                   G - Structure containing delta H and delta S
%
% Output arguments - deriv - returns the array of derivatives
%                            calculated. A vertically concatenated
%                            array (like the input)of dNjdt,dNidt, and
%                            dN1dt)

global a_R;         % r water & ice (um)
global a_R_i;         % r water & ice (um)
global a_R_2;       % r^2 water and ice (um^2)
global a_R_i2;       % r^2 water and ice (um^2)
global a_R_3;       % r^3 water and ice (um^3)
global a_R_i3;       % r^3 water and ice (um^3)
global a_V_i;       % vol. conc. of ice
global a_V_j;       % vol. conc. of water
global v1_j;        % "volume of a water molecule"
global v1_i;        % "volume of an ice molecule"
global a_times;     % a_times(time,p(H2O),T, x(ice)) array to keep
%snapshots of few variables in time
```

```
global nm_cond;     % net_mass_condesation
global t_low;       % temperature of experiment, C
global t_high;      % teperature of the previous section
global f_handle;    % name of temperature function to be used
global counter;     % allows user to keep track of variables of
%interest
global run_type;    % designates a direct, compare or inverse run
global endTime

global flow;
global solver;
global constant;
global input;
global output;
global n_sections;
global r_time;

m = size(a_N_j_a_N_i_N1,1); % Read dimension of input vector
%n = m-1;
n = m-4; % N1lost added to deteade.m, % and Niv and Nis
o = n/2;

% Unbundle input (for ODE standpoint, this would be yo)

a_N_j = a_N_j_a_N_i_N1(1:o);
a_N_i = a_N_j_a_N_i_N1(o+1:n);
N1 = a_N_j_a_N_i_N1(m);
N1lost = a_N_j_a_N_i_N1(m-1);
a_V_i(:) = (a_N_i.*(a_R_i3*4/3*pi))';
a_V_j(:) = (a_N_j.*(a_R_3*4/3*pi))';

%%%%%%%%%%%%%%%%%%%%%%%%%%%%%%%%%%%%%%%%%%%%%%%%%%%%%%%%%%%%%%%%%%%%%%%
a_Kelvin_j=zeros(input.n_radii_133,1);
a_Kelvin_i=zeros(input.n_radii_133,1);
a_p_sat_w = zeros(input.n_radii_133,1);
a_p_sat_i = zeros(input.n_radii_133,1);
a_dNjdt = zeros(input.n_radii_133,1);
a_dNidt = zeros(input.n_radii_133,1);
%%%%%%%%%%%%%%%%%%%%%%%%%%%%%%%%%%%%%%%%%%%%%%%%%%%%%%%%%%%%%%%%%%%%%%%

% Unbundle constants

p = input.p;
R = constant.R;
Mw = constant.Mw;
Na = constant.Na;

% Initialize temperature variables, calculate pressure

temperature = str2func(f_handle);
T = feval(temperature,t,t_profile);
p_inf = (N1*1e6/Na)*R*T; %P_sat(T,'ice');
ro_j = rho(1);
ro_i = rho(2);

% Wall losses
Dv1 = Dv(p,T);
```

```
if n_sections == 1.06
    % small flow tube with 26 mm diameter, 1.3 cm radius
    k = 3.66*Dv1/((1.3)^2);
else
    % old flow tube
    k = 3.66*Dv1/((1.75/2*2.54)^2);
end
p_sat_i = p_sat(T,'ice');
N_i = p_sat_i*Na/(R*T*1e6);

%%%%%%%%%%%%%%%%%%% Freezing %%%%%%%%%%%%%%%%%%%%5

if flow.volume_freezing
    J_T = Jv_Gibbs(T,G);
    dNjvdt = -a_N_j(:).*(J_T*a_R_3(:)*(4.0/3.0*pi*1e-12));
    dNivdt = -dNjvdt;
else
    dNjvdt = 0;
    dNivdt = 0;
end

if flow.surface_freezing
    J_T_s = Js_Gibbs(T,G);
    dNjsdt = -a_N_j(:).*(J_T_s*a_R_2*(4.0*pi*1e-8));
    dNisdt = -dNjsdt;
else
    dNjsdt = 0;
    dNisdt = 0;
end

dNjdt = dNjvdt+dNjsdt;
dNidt = dNivdt+dNisdt;

%%%%%%%%%%%%%%%% Mass Transfer %%%%%%%%%%%%%%%%%%%

if flow.mass_transfer

    Dv_water = Dv_star(a_R*1e-4,p,T,'water');
    Dv_ice = Dv_star(a_R_i*1e-4,p,T,'ice');
    p_sat_w = p_sat(T,'water');
    p_sat_i = p_sat(T,'ice');
    if flow.Kelvin_effect
        a_Kelvin_j(:) = exp(2*Sigma_w(T)*Mw./(ro_j*1e3*R*T*a_R(:)*1e-
6));
        a_Kelvin_i(:) = ones(input.n_radii_133,1);
    else
        a_Kelvin_j(:) = ones(input.n_radii_133,1);
        a_Kelvin_i(:) = ones(input.n_radii_133,1);
    end;

    a_p_sat_w(:) = p_sat_w * a_Kelvin_j(:);
    a_p_sat_i(:) = p_sat_i* a_Kelvin_i(:);

    dRjdt = 1e5*Dv_water(:)*Mw.*(p_inf/T-
a_p_sat_w(:)./T)/R./(ro_j*a_R);  % um/s
    dRidt = 1e5*Dv_ice(:)*Mw.*(p_inf/T-
a_p_sat_i(:)./T)/R./(ro_i*a_R_i);
```

```
    % 1e8 for cm^2 -> um^2 (Dv_water&ice)
    % 1e12 for cm^3 -> um^3 (ro_j&i)
    % 1e-6 for m-1 -> um-1 (R - Joules term)
    % 1e-12 for m-1(^2) -> um-1(^2) (p_inf & p_satw&i)
    % 1e3 for Kg -> g
    % total = 1e5

    dmjdt = (dRjdt*ro_j).*a_N_j.*(4*pi*a_R_2); % pg/s
    dmidt = (dRidt*ro_i).*a_N_i.*(4*pi*a_R_i2);

    dN1_jdt = -(dmjdt)/(v1_j*ro_j); % # of molecules/s
    dN1_idt = -(dmidt)/(v1_i*ro_i);

    a_V_crit = a_R_3*(4/3*pi); % used in mass transfer sharing
%procedure
    a_V_crit_i = a_R_i3*(4/3*pi); % v1_j&v1_i/(a_V_crit(ii)-
%a_V_crit(ii-1))
     % designates the difference in number of water molecules in bins
%of different sizes

    % This algorithm is based on the one developed by A Prakash, A. P.
    % Bapat and M.R.Zachariah Aerosol Science and Technology,
    % 37:892-898,2003

    %%%%%%% WATER Transfer %%%%%%%%%%%%

    for ii = 2:input.n_radii_133-1

        if p_inf > a_p_sat_w(ii-1)
% if condensation occurs in a bin of smaller size (ii-1)
            addterm1 = -v1_j/(a_V_crit(ii)-a_V_crit(ii-1))*dN1_jdt(ii-
1); % add to reference bin (ii)
        else
            addterm1 = 0;
% otherwise ignore
        end
        if p_inf < a_p_sat_w(ii+1)
% if evaporation occurs in a bin of larger size (ii+1)
            addterm2 =  v1_j/(a_V_crit(ii+1)-
a_V_crit(ii))*dN1_jdt(ii+1); % add to reference bin (ii)
        else
            addterm2 = 0;
% otherwise ignore
        end % if p_inf > a_p_sat_w(ii)
        if p_inf > a_p_sat_w(ii)
% if condensation occurs in reference bin (ii)
            subterm1 =  -v1_j/(a_V_crit(ii+1)-
a_V_crit(ii))*dN1_jdt(ii);  % subtract from reference bin (ii)
        else
            subterm1 = 0;
% otherwise ignore
        end
        if p_inf < a_p_sat_w(ii)
% if evaporation occurs in reference bin (ii)
            subterm2 = v1_j/(a_V_crit(ii)-a_V_crit(ii-1))*dN1_jdt(ii);
% subtract from reference bin (ii)
        else
```

```
            subterm2 = 0;
% otherwise ignore
        end % if p_inf < a_p_sat_w(ii)

        a_dNjdt(ii) = ((addterm1+addterm2) - (subterm1 + subterm2));
% Determin net result from addition and subtraction

    end % for ii = 1:n_radii_133

    %%%%%%%%% ICE Transfer %%%%%%%%% (description of method in water
                               %  applies directly to ice)

    for ii = 2:input.n_radii_133-1

        if p_inf > a_p_sat_i(ii-1)
            addterm1 = -v1_i/(a_V_crit_i(ii)-a_V_crit_i(ii-
1))*dN1_idt(ii-1);
        else
            addterm1 = 0;
        end
        if p_inf < a_p_sat_i(ii+1)
            addterm2 =  v1_i/(a_V_crit_i(ii+1)-
a_V_crit_i(ii))*dN1_idt(ii+1);
        else
            addterm2 = 0;
        end % if p_inf > p_sat_w(ii)
        if p_inf > a_p_sat_i(ii)
            subterm1 =  -v1_i/(a_V_crit_i(ii+1)-
a_V_crit_i(ii))*dN1_idt(ii);
        else
            subterm1 = 0;
        end
        if p_inf < a_p_sat_i(ii)
            subterm2 = v1_i/(a_V_crit_i(ii)-a_V_crit_i(ii-
1))*dN1_idt(ii);
        else
            subterm2 = 0;
        end % if p_inf < p_sat_w(ii)

        a_dNidt(ii) =((addterm1+addterm2) - (subterm1 + subterm2));

    end % for ii = 1:n_radii_133
    dN1dt = sum(dN1_jdt+dN1_idt);   % Net change in far field pressure
%comparing evaporation and condensation
    dN1dt2 = -k*(N1-N_i); % Wall losses
    dN1dt_total  = dN1dt + dN1dt2;

else

    dN1dt_total = 0;

end  % if flow.mass_transfer

% a_times keeps track of important varibles used in the plotting
procedures

if n_sections == 1.06
```

```
    % small flow tube: residence time is about 4 s, need smaller time
steps
    tcounter = t*10+1;
else
    % old flow tube: residence time about 35 s for bottom 2 sections
    tcounter = t+1;
end
if (tcounter > counter | t == r_time)
    if ~strcmp(run_type,'inverse_run')
        % attention this ice fraction is mass fraction
        ice_fraction =
sum(a_N_i(:).*a_R_i3(:))*ro_i/(sum(a_N_j(:).*a_R_3(:))*ro_j+sum(a_N_i(:
).*a_R_i3(:))*ro_i+1e-10);
        if ice_fraction*100 < 99
            endTime = t;
        end

        a_times(counter,1)=t;          % time
        a_times(counter,2)=p_inf;      % pressure
        a_times(counter,3)=T-273.15;   % temperature
        a_times(counter,4)=ice_fraction; %ice fraction
        a_times(counter,5) = sum(dNivdt); %freeze rate due to JV
        a_times(counter,6) = sum(dNisdt); %freeze rate due to JS
        a_times(counter,7) = p_inf/p_sat_w;
        a_times(counter,8) = p_inf/p_sat_i;
        % total number concentration
        a_times(counter,9) = sum(a_N_j);
        a_times(counter,10) = sum(a_N_i);
        % total volume concentration
        a_times(counter,11) = sum(a_N_j(:).*(4/3*pi*a_R_3(:)));
        a_times(counter,12) = sum(a_N_i(:).*(4/3*pi*a_R_i3(:)));
        % cumulative wall losses (expressed as vapour molecule
%concentration
        a_times(counter,13) = N1lost;
        a_times(counter,14) = a_times(counter,10)/a_times(1,9);
% number fraction frozen
    end;
    counter = counter + 1;

end

deriv =
vertcat(dNjdt+a_dNjdt,dNidt+a_dNidt,sum(dNivdt),sum(dNisdt),dN1dt2,dN1d
t_total); % N1lost added to deteade.m, % and Niv and Nis

return
```

B.3. Model Subroutines

1) *coordtransform3.m:* transforms/rescales minimization parameters ΔH_{act} and ΔS_{act} to reduce computation time.

```
function Gprime =
coordtransform3(G,thetav,thetas,interceptv,intercepts,direction)

if strcmp(direction,'code')

    Gprime.dHv = G.dHv*cos(thetav) +  (G.dSv-interceptv)*sin(thetav);
    Gprime.dSv = - G.dHv*sin(thetav) +  (G.dSv-interceptv)*cos(thetav);

    Gprime.dHs = G.dHs*cos(thetas) +  (G.dSs-intercepts)*sin(thetas);
    Gprime.dSs = - G.dHs*sin(thetas) +  (G.dSs-intercepts)*cos(thetas);

    Gprime.dHs = Gprime.dHs/1e6;
    Gprime.dHv = Gprime.dHv/1e6;

elseif strcmp(direction,'decode')

    G.dHv = G.dHv*1e6;
    G.dHs = G.dHs*1e6;

    Gprime.dHv = G.dHv*cos(thetav) -  G.dSv*sin(thetav);
    Gprime.dSv = G.dHv*sin(thetav) +  G.dSv*cos(thetav)+interceptv;

    Gprime.dHs = G.dHs*cos(thetas) -  G.dSs*sin(thetas);
    Gprime.dSs = G.dHs*sin(thetas) +  G.dSs*cos(thetas)+intercepts;

else

    sprintf('error');

end
```

2) Dv.m: Calculates the gas-phase diffusion coefficient of water vapour in air for a given temperature and pressure.

```
function r = Dv(p,T)

%   Returns diffusion constant Dv (cm2 s-1) of water vapour in air
%   at pressure p (Pa) and temperature T (K)

r = 0.211*(T/273.15)^1.94*(1.01325e5/p);
```

3) Dv_star.m: Corrects gas-phase diffusion coefficients for non-continuum effects (Fuchs correction) and droplet curvature (Kelvin effect).

```
function res = Dv_star(r,p,T,component)
```

```
%   Corrected diffusion constant for water vapour in air
%   for droplet of radius r(cm) at pressure p(Pa) and temperature T
%   (K), component is 'water' or 'ice'
%   lambda_ref (cm) is for 283 K and 0.8e5 Pa
global massaccom;
Mw=18.0e-3;     % molecular weight of water, kg mol-1
R = 8.31;       % universal gas constant, J mol-1 K-1

Dv = 0.211*(T/273.15)^1.94*(1.01325e5/p);
lambda_ref = 8e-6;
p_ref = 0.8e5;
T_ref = 283.0;
lambda = lambda_ref*(p_ref/p)*(T/T_ref);
Delta_v = 1.3*lambda; % Pruppacher&Klett
if strcmp(component,'water')
    alpha = massaccom.water;
elseif strcmp(component,'ice')
    alpha = massaccom.ice;
end;
res = Dv./(r./(r+Delta_v) + Dv./(r*alpha)*1e-2*sqrt(2*pi*Mw/(R*T)));
```

4) Jv_Gibbs.m: Calculates volume-based nucleation rate, $J_V(T)$.

```
function J = Jv_Gibbs(T,G)

%   Returns freezing nucleation constant Jv (cm3 s-1) for water
%   calculated at a temperature T (K) using classical expression
%   Jv = N_L(kT/h)exp(-dG/(RT))
%   given in A. Tabazadeh et al., PNAS, 2002, 99(25), 15873.
%   Originally given in Turnbull and Fisher, J.Chem.Phys., 1949, 17, 71
%   Temperature range of validity is about -40 C <= t <= -30 C.

N_L = 3.35e22;
k = 1.381e-23;
h = 6.626e-34;
R = 8.314; %J mol-1 K-1
dG = G.dHv - G.dSv.*T; %J mol-1

J = N_L*(k.*T/h).*exp(-dG/(R.*T));
```

5) Js_Gibbs.m: Calculates surface-based nucleation rate, $J_S(T)$.

```
function r = Js_Gibbs(T,G)

%   Returns freezing nucleation constant Js (cm2 s-1) for water
%   calculated at a temperature T (K) using classical expression
%   Js = N_s(kT/h)exp(-dG/(RT))
%   given in A. Tabazadeh et al., PNAS, 2002, 99(25), 15873.
%   Originally given in Turnbull and Fisher, J.Chem.Phys., 1949, 17, 71
```

```
%   Temperature range of validity is about -40 C <= t <= -30 C.

N_S = 1.0392e+015;
k = 1.381e-23;
h = 6.626e-34;
R = 8.314; %J mol-1 K-1
dG = G.dHs - G.dSs.*T; %J mol-1

r = N_S*(k.*T/h).*exp(-dG/(R.*T));
```

6) makea_D_i.m: Creates arrays for experimental ice distributions from input files.

```
function a_D_i = makea_D_i(f_D_i,index_i,window_i)

global flow

    a_D_i=load(f_D_i,'-ascii');


    if size(index_i,2) == 1        % If index_i references 1 column
        input.n_radii=size(a_D_j,1);
        a_D_i(:,2)=a_D_i(:,(2*(index_i - 1) + 2))-1.0+1e-30; % Read the
%one column
        a_D_i(:,3)=a_D_i(:,2)*4/3*pi.*a_D_j(:,1).^3; % Calculate Volume
%vector
        for n = 1:size(a_D_i,1)
            if window_i(1)>a_D_i(n,1)
                a_D_i(n,2) = 1e-30;
                a_D_i(n,3) = 1e-30;
            end
            if window_i(2)<a_D_i(n,1)
                a_D_i(n,2) = 1e-30;
                a_D_i(n,3) = 1e-30;
            end
        end
    elseif size(index_i,2) == 2       % If index_i referneces 2 columns
        input.n_radii=size(a_D_i,1);
        a_D_i(:,2)=a_D_i(:,(2*(index_i(1) - 1) + 2))-1.0+1e-30; % Read
%the one column
        a_D_i(:,3)=a_D_i(:,2)*4/3*pi.*a_D_i(:,1).^3; % Calculate Volume
%vector
        a_D_i(:,4)=a_D_i(:,(2*(index_i(2) - 1) + 2))-1.0+1e-30; % Read
%the one column
        a_D_i(:,5)=a_D_i(:,4)*4/3*pi.*a_D_i(:,1).^3; % Calculate Volume
%vector
        if flow.sumAdi
            a_D_i(:,5) = a_D_i(:,5)+a_D_i(:,3);
        end
        for n = 1:size(a_D_i,1)
            if window_i(1)>a_D_i(n,1)
                a_D_i(n,2) = 1e-30;
                a_D_i(n,3) = 1e-30;
            end
```

```
            if window_i(2)<a_D_i(n,1)
                a_D_i(n,2) = 1e-30;
                a_D_i(n,3) = 1e-30;
            end
            if window_i(3)>a_D_i(n,1)
                a_D_i(n,4) = 1e-30;
                a_D_i(n,5) = 1e-30;
            end
            if window_i(4)<a_D_i(n,1)
                a_D_i(n,4) = 1e-30;
                a_D_i(n,5) = 1e-30;
            end
        end
    else
        sprintf('error in input');
        return
    end

    return
```

7) makea_D_j.m: Creates arrays for experimental water distributions from input files.

```
function a_D_j = makea_D_j(f_D_j,index_j,window_j)

% Creates array for water distribution from input file

    a_D_j=load(f_D_j);

if size(index_j,2) == 1       % If index_j references 1 column
    input.n_radii=size(a_D_j,1);
    a_D_j(:,2)=a_D_j(:,(2*(index_j - 1) + 2))-1.0+1e-30;  % Read the
%one column
    a_D_j(:,3)=a_D_j(:,2)*4/3*pi.*a_D_j(:,1).^3;  % Calculate volume
%vector
    for n = 1:size(a_D_j,1)
        if window_j(1)>a_D_j(n,1)
            a_D_j(n,3) = 1e-30;
        end
        if window_j(2)<a_D_j(n,1)
            a_D_j(n,3) = 1e-30;
        end
    end
elseif size(index_j,2) == 2    % If index_j references 2 columns
    input.n_radii=size(a_D_j,1);
    a_D_j(:,2)=((a_D_j(:,(2*(index_j(1) - 1) + 2))-1.0) +
(a_D_j(:,(2*(index_j(2) - 1) + 2))-1.0)) + 1e-30;  % Add columns 2 & 4
%together
    a_D_j(:,3)=a_D_j(:,2)*4/3*pi.*a_D_j(:,1).^3;   % Calculate volume
%vector
    for n = 1:size(a_D_j,1)
        if window_j(1)>a_D_j(n,1)
            a_D_j(n,3) = 1e-30;
        end
```

```
        if window_j(2)<a_D_j(n,1)
            a_D_j(n,3) = 1e-30;
        end
    end
else
    sprintf('error in input')
    return
end

return
```

8) p_sat.m: Calculates saturation vapour pressure above water and ice aerosols.

```
function r = P_sat(T,component)

%   Returns equilibrium vapour pressure (Pa)
%   at temperature T (K) above components 'water' and 'ice'

t = T - 273.15;

if strcmp(component,'water')
   r = 6.1121*exp(17.502*t/(240.97+t))*1e2;
end

if strcmp(component,'ice')
   r = 6.1115*exp(22.452*t/(272.55+t))*1e2;
end
```

9) resize.m: Changes the number of size bins or the range of radii in water and ice distributions.

```
function res = resize(big_bin,mode)

global a_D_j;       % r, N(r), V(r) - experimental data for original
%water aerosol
global a_D_i;       % r, N(r), V(r) - experimental data for ice
%distribution
global a_R;         % r water & ice (um)
global a_R_2;       % r^2 water and ice (um^2)
global a_R_3;       % r^3 water and ice (um^3)
global a_N_j;       % N(r) water
global a_V_j;       % V(r) water
global a_N_i;       % N(r) ice
global a_V_i;       % V(r) ice
global bin_multiplier;

global flow;
global solver;
```

```
global constant;
global input;
global output;

a_R = a_D_j(:,1);  % Read a_R vector from file
delta_lgr = (log10(a_R(2)) - log10(a_R(1)))/bin_multiplier; % Determine
%bin spacing (log)

if big_bin ==0
    big_bin = a_D_j(size(a_D_j,1)); % Determine largest particle size
end

int = log10(big_bin) - log10(a_R(1)); % determine difference between
%largest and smallest bin
n_radii_133 = ceil(int/delta_lgr)+1;  % find number of bins necessary
%to cover this interval

for k=2:n_radii_133               % Fill empty matrix elements with
%invented radii
    a_R(k) = 10^(log10(a_R(k-1)) + delta_lgr);
end;

a_R = a_R(:);

%=========== Initialize variables ==
n_radii = input.n_radii;
input.n_radii_133 = n_radii_133;
%====================================
a_N_i=zeros(n_radii_133,1);
a_V_i=zeros(n_radii_133,1);
a_N_j=zeros(n_radii_133,1);
a_V_j=zeros(n_radii_133,1);
%====================================

% Build a_V_j vector by interpolating file with new a_R values (if
% bin_multiplier is used)

a_V_j = interp1(log10(a_D_j(:,1)),a_D_j(:,3),log10(a_R),'spline');

%TK: interp1 extrapolates: results in negative values for volume=> the
scaling later uses these negative values !!!!.
%
a_R_2 = a_R.^2; % Calculating a_R^2 and a_R^3 saves processing time
a_R_3 = a_R.^3;

scale = sum(a_D_j(:,3))/sum(a_V_j)
a_V_j(:) = a_V_j(:).*scale;   % scale total volume back to original
%distribution volume

if (strcmp(mode,'inverse_run') || strcmp(mode,'compare_run'))

    a_D_j(:,3) = a_D_j(:,3).*scale;
    a_D_i(:,3) = a_D_i(:,3).*scale;
    a_D_i(:,5) = a_D_i(:,5).*scale;
end

for n = 1:size(a_V_j,1)
```

```
    if a_V_j(n)<0
        a_V_j(n) = abs(a_V_j(n));   % Make sure a_V_j contains no
%negative numbers from interpolation
    end
end

a_N_j = a_V_j./(4.0*pi/3.0*a_R_3);  % Build a_N_j from a_V_j
a_D_j(:,2) = a_D_j(:,3)./(4.0*pi/3.0*a_R_3(1:size(a_D_j(:,3),1)));
res = scale;

return
```

10) *ro.m:* Computes the density of water and ice at reduced experimental temperatures.

```
function r = ro(T,component)

t = T - 273.15;

if strcmp(component,'water')
    a = [0.99986 6.690e-5 -8.486e-6 1.518e-7 -6.9484e-9 -3.6449e-10 -
7.497e-12];
    r = 0.0;
    for i = 1:7
        r = r + a(i)*t.^(i-1);
    end;
end

if strcmp(component,'ice')
    a = [0.9167 -1.75e-4 -5.0e-7];
    r = 0.0;
    for i = 1:3
        r = r + a(i)*t.^(i-1);
    end;
end

return;
```

10) scale.m: Scales initial and final supercooled water and/or ice distributions such that total water mass is conserved.

```
function a_D_j = scale(a_D_i,a_D_j)

global output
global t_profile
global f_handle
global flow
global constant
global a_R_2
```

```
global a_R_i
global a_R_i_2
global r_time
global scaling_values   % keep track of all scaling factors

temperature = str2func(f_handle);
    output.T_start = feval(temperature,0,t_profile);
    output.T_end = feval(temperature,r_time,t_profile);
    T = output.T_start;

    if flow.density
        ro_j = ro(output.T_start,'water');
        ro_i = ro(output.T_end,'ice');
    end

    output.p_inf_start = p_sat(output.T_start,'water');
    a_R_2 = a_D_i(:,1).^2;
    a_R_i = a_D_i(:,1)*(ro_j/ro_i)^(1/3);
    a_R_i_2 = a_R_i.^2;
    Sj=sum(4*pi*a_R_2.*a_D_i(:,2));
    Si=sum(4*pi*a_R_i_2.*a_D_i(:,4));
    output.p_inf_end = Sj/(Si+Sj)*p_sat(output.T_end,'water') +
Si/(Si+Sj)*p_sat(output.T_end,'ice');

    dm_liq = (output.p_inf_start/output.T_start -
output.p_inf_end/output.T_end)*constant.Mw*1e-6*1e12*1e3/constant.R
    scaling = (sum(a_D_i(:,3))*ro_j+sum(a_D_i(:,5))*ro_i -
dm_liq)./(sum(a_D_j(:,3))*ro_j);
    %additional scaling to account for losses
    sum(a_D_j(:,3))*ro_j
    sum(a_D_i(:,3))*ro_j
    sum(a_D_i(:,5))*ro_i
    a_D_j(:,3) = a_D_j(:,3)*scaling;
    a_D_j(:,2) = a_D_j(:,3)./(4/3*pi*a_D_j(:,1).^3);
    scaling
    scaling_values(1) = scaling; % scale Start water size distribution
acording to mass balance
    return
```

11) tCorr.m: Corrects aerosol residence times to account for changes in temperature.

```
function r_time = tCorr(n_sections,section_tau)

global input
global solver

if n_sections > 1.0e-5
    r_time = n_sections*section_tau;
    r_time = r_time*298.15/((input.T_high + input.T_low)/2);
    if input.early_freezing
        input.delta = ((1.2318-1.181)+(1.3221-
1.2572))/2*100/(47.63/(section_tau*298.15/((input.T_high +
input.T_low)/2)));
```

```
    else
        input.delta = 0;
    end;

else

    r_time = r_time*298.15/((input.T_high + input.T_low)/2);
    if input.early_freezing
        input.delta = ((1.2318-1.181)+(1.3221-
1.2572))/2*100/(47.63/(section_tau*298.15/((input.T_high +
input.T_low)/2)));
    else
        input.delta = 0;
    end;

    sprintf('Residence time (298K): %6.3f',r_time)
end;

if solver.d_time/r_time > 0.001
    solver.d_time = 0.001*r_time;
end;

return
```

12) temperature2.m: Determines temperature at any given residence time in the flow tube.

```
function temp = temperature2(t,t_profile)

% Determines temperature at any given residence time in flow tube

index = fix(t(1)/(t_profile(2,1)-t_profile(1,1)))+1;

dTdt = (t_profile(index+1,2)-t_profile(index,2))/(t_profile(index+1,1)-
t_profile(index,1));
temp = t_profile(index,2) + dTdt*(t(1)-t_profile(index,1));

return
```

13) temperatureProfile.m: Determines axial temperature profile in flow tube based on CFD calculations.

```
function profile =
temperatureProfile(runtype,input,stepsize,T_profile_i)

global flow
```

```
if flow.nTprofs == 1

    if strcmp(runtype,'ab-cd')
        t_p = load('tempab-cd.txt','-ascii');
    elseif strcmp(runtype,'abc-d')
        t_p = load('tempabc-d.txt','-ascii');
    elseif strcmp(runtype,'a-bcd')
        t_p = load('tempa-bcd.txt','-ascii');
    elseif strcmp(runtype,'a-b')
       t_p = load('tempa-b_small.txt','-ascii');

    else
        sprintf('error');
    end

    time = t_p(:,1);
    profile = (time(1):stepsize:time(size(time,1)))';
    slope = t_p(:,2);
    intercept = t_p(:,3);

    new_array = slope*(input-273.15) + intercept;

    profile(:,2) = spline(time,new_array,profile(:,1));

else

    if strcmp(runtype,'ab-cd')
        t_p_time = load(horzcat('temp_ab-cd_time.txt'),'-ascii');
        t_p_tc = load(horzcat('temp_ab-cd_tc.txt'),'-ascii');
        t_p_tk = load(horzcat('temp_ab-
cd(',num2str(T_profile_i),')_tk.txt'),'-ascii');
    elseif strcmp(runtype,'abc-d')
        t_p_time = load(horzcat('temp_abc-d_time.txt'),'-ascii');
        t_p_tc = load(horzcat('temp_abc-d_tc.txt'),'-ascii');
        t_p_tk = load(horzcat('temp_abc-
d(',num2str(T_profile_i),')_tk.txt'),'-ascii');
    elseif strcmp(runtype,'a-bcd')
        t_p_time = load(horzcat('temp_a-bcd_time.txt'),'-ascii');
        t_p_tc = load(horzcat('temp_a-bcd_tc.txt'),'-ascii');
        t_p_tk = load(horzcat('temp_a-
bcd(',num2str(T_profile_i),')_tk.txt'),'-ascii');
    else
        sprintf('error');
    end

    for i = 2:size(t_p_tc,2)
        t_p_time(:,i)=t_p_time(:,1);
    end;

    for i = 2:size(t_p_time,1)
        t_p_tc(i,:)=t_p_tc(1,:);
    end;

    time = t_p_time(:,1);
    profile = (time(1):stepsize:time(size(time,1)))';
    hold on
```

```
    [XI,YI] = meshgrid(time,-stepsize*10+(input-
273.15):stepsize*10:(input-273.15)+stepsize*10);
    ZI = griddata(t_p_time,t_p_tc,t_p_tk,XI,YI,'linear');
    profile(:,2) = interp1(time,ZI(2,:),profile(:,1),'v5cubic');
end;

return
```

REFERENCES

1. Reist, P. C. *Aerosol Science and Technology*, 2nd ed.; McGraw-Hill: New York, 1993.
2. Penner, J. E.; Hegg, D.; Leaitch, R. *Environ. Sci. Technol.* **2001**, *35*, 332A-340A.
3. Finlayson-Pitts, B. J.; Pitts, J. N. *Chemistry of the Upper and Lower Atmosphere*, Academic Press: San Diego, 2000.
4. Poschl, U. *Angew. Chem. , Int. Ed. Engl.* **2005**, *44*, 7520-7540.
5. Hinds, W. C. *Aerosol Technology: Properties, Behavior, and Measurement of Airborne Particles*, 2nd ed.; Wiley-Interscience: Toronto, 1999.
6. Charlson, R. J.; Schwartz, S. E.; Hales, J. M.; Cess, R. D.; Coakley, J. A.; Hansen, J. E.; Hofmann, D. J. *Science* **1992**, *255*, 423-430.
7. Morgan, M. G.; Adams, P. J.; Keith, D. W. *Climatic Change* **2006**, *75*, 195-214.
8. Twomey, S. *J. Atmos. Sci.* **1977**, *34*, 1149-1152.
9. Heymsfield, A. J.; Sabin, R. M. *J. Atmos. Sci.* **1989**, *46*, 2252-2264.
10. Lynch, D. K. *Acta Astronaut.* **1996**, *38*, 859-863.
11. Seinfeld, J. H.; Pandis, S. N. *Atmospheric Chemistry and Physics: From Air Pollution to Climate Change*, John Wiley & Sons, Inc.: New York, 1998.

12. Pruppacher, H. R.; Klett, J. D. *Microphysics of Clouds and Precipitation*, Kluwer Academic Publishers: Boston, 1998.

13. Mace, G. G.; Benson, S.; Kato, S. *J. Geophys. Res. -Atmos.* **2006**, *111*.

14. Martin, S. T. *Chem. Rev.* **2000**, *100*, 3403-3453.

15. Cziczo, D. J.; Abbatt, J. P. D. *J. Geophys. Res.* **1999**, *104*, 13781-13790.

16. Hu, J. H.; Abbatt, J. P. D. *J. Phys. Chem. A* **1997**, *101*, 871-878.

17. Chelf, J. H.; Martin, S. T. *J. Geophys. Res.* **2001**, *106*, 1215-1226.

18. Fortin, T. J.; Shilling, J. E.; Tolbert, M. A. *J. Geophys. Res.* **2002**, *107*.

19. Matthias, B. T.; Remeika, J. P. *Phys. Rev.* **1956**, *103*, 262.

20. Atkins, P. *Physical Chemistry*, 6th ed.; W.H. Freeman and Company: New York, 1998.

21. Sassen, K.; Liou, K. N.; Kinne, S.; Griffin, M. *Science* **1985**, *227*, 411-413.

22. Dickens, D. *M.Sc. Thesis*, University of Waterloo: 2000.

23. Bertram, A. K. *Ph.D. Thesis*, University of Waterloo: 1998.

24. Rawson, H. *Properties and Applications of Glass*, Elsevier Scientific Publishing Company: New York, 1980.

25. Cantrell, W.; Heymsfield, A. *Bull. Amer. Meteorol. Soc.* **2005**, *86*, 795-807.

26. Djikaev, Y. S.; Tabazadeh, A.; Hamill, P.; Reiss, H. *J. Phys. Chem. A* **2002**, *106*, 10247-10253.

27. Demott, P. J.; Rogers, D. C. *J. Atmos. Sci.* **1990**, *47*, 1056-1064.

28. Duft, D.; Leisner, T. *Atmos. Chem. Phys.* **2004**, *4*, 3077-3088.

29. Stockel, P.; Weidinger, I. M.; Baumgartel, H.; Leisner, T. *J. Phys. Chem. A* **2005**, *109*, 2540-2546.

30. Kramer, B.; Hubner, O.; Vortisch, H.; Woste, L.; Leisner, T.; Schwell, M.; Ruhl, E.; Baumgartel, H. *J. Chem. Phys.* **1999**, *111*, 6521-6527.

31. Butorin, G. T.; Skripov, V. P. *Kristallografiya* **1972**, *17*, 379-384.

32. Taborek, P. *Phys. Rev. B* **1985**, *32*, 5902-5906.

33. Pruppacher, H. R. *J. Atmos. Sci.* **1995**, *52*, 1924-1933.

34. Tabazadeh, A.; Djikaev, Y. S.; Reiss, H. *Proc. Natl. Acad. Sci. U. S. A.* **2002**, *99*, 15873-15878.

35. Tabazadeh, A.; Djikaev, Y. S.; Hamill, P.; Reiss, H. *J. Phys. Chem. A* **2002**, *106*, 10238-10246.

36. Chushak, Y.; Bartell, L. S. *J. Phys. Chem. A* **2000**, *104*, 9328-9336.

37. Chushak, Y. G.; Bartell, L. S. *J. Phys. Chem. B* **1999**, *103*, 11196-11204.

38. Huang, J. F.; Bartell, L. S. *J. Phys. Chem. A* **2002**, *106*, 2404-2409.

39. Elbaum, M.; Lipson, S. G.; Dash, J. G. *J. Cryst. Growth* **1993**, *129*, 491-505.

40. Shaw, R. A.; Durant, A. J.; Mi, Y. *J. Phys. Chem. B* **2005**, *109*, 9865-9868.

41. Durant, A. J.; Shaw, R. A. *Geophys. Res. Lett.* **2005**, *32*.

42. Sastry, S. *Nature* **2005**, *438*, 746-747.

43. Hindmarsh, J. P.; Russell, A. B.; Chen, X. D. *J. Phys. Chem. C* **2007**, *111*, 5977-5981.

44. Vrbka, L.; Jungwirth, P. *J. Phys. Chem. B* **2006**, *110*, 18126-18129.

45. Zasetsky, A. Y.; Remorov, R.; Svishchev, I. M. *Chem. Phys. Lett.* **2007**, *435*, 50-53.

46. Mendez-Villuendas, E.; Bowles, R. K. *Phys. Rev. Lett.* **2007**, *98*.

47. Charlson, R. J.; Seinfeld, J. H.; Nenes, A.; Kulmala, M.; Laaksonen, A.; Facchini, M. C. *Science* **2001**, *292*, 2025-2026.

48. Donaldson, D. J.; Anderson, D. *J. Phys. Chem. A* **1999**, *103*, 871-876.

49. Facchini, M. C.; Mircea, M.; Fuzzi, S.; Charlson, R. J. *Nature* **1999**, *401*, 257-259.

50. Castellano, N. E.; Avila, E. E.; Saunders, C. P. R. *Atmos. Environ.* **2004**, *38*, 6751-6761.

51. Schwarzenbock, A.; Mertes, S.; Heintzenberg, J.; Wobrock, W.; Laj, P. *Atmos. Res.* **2001**, *58*, 295-313.

52. Petrucci, R. H.; Harwood, W. S.; Herring, F. G.; Madura, J. D. *General Chemistry: Principles and Modern Applications*, 9th ed.; Pearson Prentice Hall: Upper Saddle River, New Jersey, 2007.

53. Kiefte, H.; Clouter, M. J.; Whalley, E. *J. Chem. Phys.* **1984**, *81*, 1419-1420.

54. Takahashi, T. *J. Cryst. Growth* **1982**, *59*, 441-449.

55. Whalley, E. *Science* **1981**, *211*, 389-390.

56. Riikonen, M.; Sillanpaa, M.; Virta, L.; Sullivan, D.; Moilanen, J.; Luukkonen, I. *Appl. Opt.* **2000**, *39*, 6080-6085.

57. Murray, B. J.; Knopf, D. A.; Bertram, A. K. *Nature* **2005**, *434*, 202-205.

58. Murray, B. J.; Bertram, A. K. *Phys. Chem. Chem. Phys.* **2006**, *8*, 186-192.

59. Murphy, D. M. *Geophys. Res. Lett.* **2003**, *30*.

60. Hallett, J. *J. Opt. Soc. Am. A-Opt. Image Sci.* **1987**, *4*, 581-&.

61. Korolev, A.; Isaac, G. A.; Hallett, J. *Quart. J. Roy. Meteorol. Soc.* **2000**, *126*, 2873-2902.

62. Korolev, A. V.; Isaac, G. A.; Hallett, J. *Geophys. Res. Lett.* **1999**, *26*, 1299-1302.

63. Lawson, R. P.; Heymsfield, A. J.; Aulenbach, S. M.; Jensen, T. L. *Geophys. Res. Lett.* **1998**, *25*, 1331-1334.

64. Mayer, E.; Hallbrucker, A. *Nature* **1987**, *325*, 601-602.

65. Goodman, J.; Toon, O. B.; Pueschel, R. F.; Snetsinger, K. G.; Verma, S. *J. Geophys. Res. -Atmos.* **1989**, *94*, 16449-16457.

66. Liou, K. N.; Takano, Y. *Atmos. Res.* **1994**, *31*, 271-298.

67. Heymsfield, A. J.; Miloshevich, L. M. *J. Atmos. Sci.* **1993**, *50*, 2335-2353.

68. Jensen, E. J.; Toon, O. B.; Tabazadeh, A.; Sachse, G. W.; Anderson, B. E.; Chan, K. R.; Twohy, C. W.; Gandrud, B.; Aulenbach, S. M.; Heymsfield, A.; Hallett, J.; Gary, B. *Geophys. Res. Lett.* **1998**, *25*, 1363-1366.

69. Abbatt, J. P. D.; Benz, S.; Cziczo, D. J.; Kanji, Z.; Lohmann, U.; Mohler, O. *Science* **2006**, *313*, 1770-1773.

70. Callaghan, R.; Lim, I. J.; Murdock, D. E.; Sloan, J. J.; Donaldson, D. J. *Geophys. Res. Lett.* **1994**, *21*, 373-376.

71. McPhail, R. *M.Sc. Thesis*, University of Waterloo: 2005.

72. TSI Instruction Manual *Model 3075/3076 Constant Output Atomizer*, TSI, Inc.: 2003.

73. Bernath, P. B. *Course Notes: Spectroscopy and Remote Sensing in Atmospheric Chemistry*, University of Waterloo: 2003.

74. Bohren, C. F.; Huffman, D. R. *Absorption and Scattering of Light by Small Particles*, John Wiley and Sons, Inc.: New York, 1983.

75. Borrmann, S.; Luo, B. P.; Mishchenko, M. *J. Aerosol Sci.* **2000**, *31*, 789-799.

76. Mishchenko, M. I.; Travis, L. D. *J. Quant. Spectrosc. Radiat. Transfer* **1998**, *60*, 309-324.

77. Zasetsky, A. Y.; Sloan, J. J.; Escribano, R.; Fernandez, D. *Geophys. Res. Lett.* **2002**, *29*.

78. Zasetsky, A. Y.; Khalizov, A. F.; Sloan, J. J. *Appl. Opt.* **2004**, *43*, 5503-5511.

79. Zasetsky, A. Y.; Khalizov, A. F.; Earle, M. E.; Sloan, J. J. *J. Phys. Chem. A* **2005**, *109*, 2760-2764.

80. Clapp, M. L.; Miller, R. E.; Worsnop, D. R. *J. Phys. Chem.* **1995**, *99*, 6317-6326.

81. Dohm, M. T.; Potscavage, A. M.; Niedziela, R. F. *J. Phys. Chem. A* **2004**, *108*, 5365-5376.

82. Norman, M. L.; Qian, J.; Miller, R. E.; Worsnop, D. R. *J. Geophys. Res. -Atmos.* **1999**, *104*, 30571-30584.

83. Bertram, A. K.; Sloan, J. J. *J. Geophys. Res. Atmos.* **1998**, *103*, 3553-3561.

84. Dickens, D. B.; Sloan, J. J. *J. Phys. Chem. A* **2002**, *106*, 10543-10549.

85. Khalizov, A.; Earle, M. E.; Johnson, W. J. W.; Stubley, G. D.; Sloan, J. J. *Rev. Sci. Instrum.* **2006**, *77*.

86. Johnson, W. J. W. *M.Sc. Thesis*, University of Waterloo: 2005.

87. Incropera, F. P.; DeWitt, D. P. *Fundamentals of Heat and Mass Transfer*, 5th ed.; John Wiley and Sons, Inc.: New York, 2002.

88. Anderson, R. J.; Miller, R. C.; Kassner, J. L.; Hagen, D. E. *J. Atmos. Sci.* **1980**, *37*, 2508-2520.

89. Hung, H. M.; Malinowski, A.; Martin, S. T. *J. Phys. Chem. A* **2002**, *106*, 293-306.

90. Bertie, J. E.; Lan, Z. D. *Appl. Spectrosc.* **1996**, *50*, 1047-1057.

91. Warren, S. G. *Appl. Opt.* **1984**, *23*, 1206-1225.

92. Errington, J. R.; Debenedetti, P. G.; Torquato, S. *Phys. Rev. Lett.* **2002**, *89*.

93. Zasetsky, A. Y.; Khalizov, A. F.; Sloan, J. J. *J. Chem. Phys.* **2004**, *121*, 6941-6947.

94. Bellissent-Funel, M. C. *Nuovo Cimento D-Cond. Matt. At.* **1998**, *20*, 2107-2122.

95. Hung, H. M.; Martin, S. T. *J. Geophys. Res. -Atmos.* **2001**, *106*, 20379-20394.

96. Li, Y. Q.; Davidovits, P.; Shi, Q.; Jayne, J. T.; Kolb, C. E.; Worsnop, D. R. *J. Phys. Chem. A* **2001**, *105*, 10627-10634.

97. Houzelot, J. L.; Villermaux, J. *Chem. Eng. Sci.* **1977**, *32*, 1465-1470.

98. Villerma, J. *Int. J. Heat Mass Transfer* **1971**, *14*, 1963-&.

99. Khalizov, A. F.; Earle, M. E.; Johnson, W. J. W.; Stubley, G. D.; Sloan, J. J. *J. Aerosol Sci.* **2006**, *37*, 1174-1187.

100. Prakash, A.; Bapat, A. P.; Zachariah, M. R. *Aerosol Sci. Tech.* **2003**, *37*, 892-898.

101. Khalizov, A. F., Personal Communication.

102. Zasetsky, A. Y.; Earle, M. E.; Cosic, B.; Schiwon, R.; Grishin, I. A.; McPhail, R.; Pancescu, R. G.; Najera, J.; Khalizov, A. F.; Cook, K. B.; Sloan, J. J. *J. Quant. Spectrosc. Radiat. Transfer* **2007**, *107*, 294-305.

103. Duda, R. O.; Hart, P. E. *Pattern Classification and Scene Analysis*, Wiley: New York, 1973.

104. Grishin, I. A., Personal Communication.

105. Choularton, T. W.; Latham, J. *Quart. J. Roy. Meteorol. Soc.* **1977**, *103*, 307-318.

106. Magee, N.; Moyle, A. M.; Lamb, D. *Geophys. Res. Lett.* **2006**, *33*.

107. Martin, S. T.; Hung, H. M.; Park, R. J.; Jacob, D. J.; Spurr, R. J. D.; Chance, K. V.; Chin, M. *Atmos. Chem. Phys.* **2004**, *4*, 183-214.

108. Sheridan, P. J.; Brock, C. A.; Wilson, J. C. *Geophys. Res. Lett.* **1994**, *21*, 2587-2590.

109. Talbot, R. W.; Dibb, J. E.; Loomis, M. B. *Geophys. Res. Lett.* **1998**, *25*, 1367-1370.

110. Warneck P. *Chemistry of the Natural Atmosphere*; Academic Press: San Diego, Ca, 2000; pp. 587-655.

111. Toon, O. B.; Pollack, J. B.; Khare, B. N. *J. Geophys. Res.* **1976**, *81*, 5733-5748.

112. Earle, M. E.; Pancescu, R. G.; Cosic, B.; Zasetsky, A. Y.; Sloan, J. J. *J. Phys. Chem. A* **2006**, *110*, 13022-13028.

113. Clapp, M. L.; Miller, R. E. *Icarus* **1993**, *105*, 529-536.

114. Koop, T., Personal Communication.

115. Jain, Y. S.; Bist, H. D.; Upreti, G. C. *Chem. Phys. Lett.* **1973**, *22*, 572-575.

116. Bajpai, P. K.; Ram, P. N.; Jain, Y. S. *J. Phys. C.* **1987**, *20*, 5577-5584.